Gas Transport Into Vortex Cavities

Nanda, S.

DOI
10.4233/uuid:aec085db-c92e-4842-9ea3-96a7dce93fd7

Publication date
2023

Document Version
Final published version

Citation (APA)
Nanda, S. (2023). *Gas Transport Into Vortex Cavities*. [Dissertation (TU Delft), Delft University of Technology]. https://doi.org/10.4233/uuid:aec085db-c92e-4842-9ea3-96a7dce93fd7

Important note
To cite this publication, please use the final published version (if applicable).
Please check the document version above.

Gas Transport Into Vortex Cavities

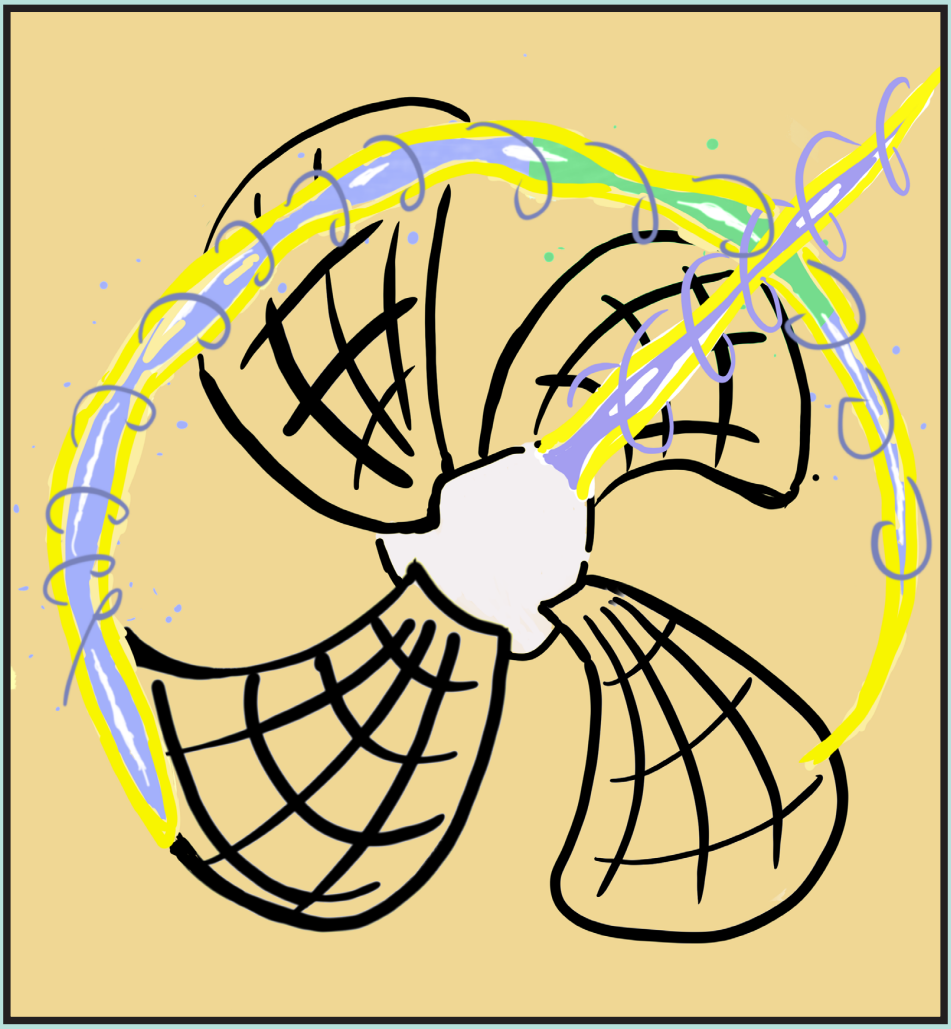

Swaraj Nanda

Gas Transport Into Vortex Cavities

Dissertation

for the purpose of obtaining the degree of doctor
at Delft University of Technology,
by the authority of the Rector Magnificus prof.dr.ir. T.H.J.J. van der Hagen,
Chair of the Board of Doctorates,
to be defended publicly on Monday 11 September 2023 at 15:00 o'clock

by

Swaraj Nanda

Master of Science in Marine Technology,
Delft University of Technology, The Netherlands,
born in Doranda, Ranchi, India.

This dissertation has been approved by the promotors

Composition of the doctoral committee:

Rector Magnificus	chairperson
Prof. dr. ir. J. Westerweel	Delft University of Technology (3mE), NL, promotor
Prof. dr. ir. T. J. C. van Terwisga	MARIN, NL/Delft University of Technology (3mE), NL, promotor
Dr. ir. G. E. Elsinga	Delft University of Technology (3mE), NL, promotor

Composition of the independent committee:

Dr. ir. J. Bosschers	MARIN, NL
Prof. dr. G.D. Weymouth	Delft University of Technology (3mE), NL
Prof. dr. M. Versluis	University of Twente, NL
Prof. dr. M. Atlar	University of Strathclyde, UK

Reserve member: Prof. dr. ir. B. J. Boersma, Delft University of Technology (3mE), NL

This research was funded by the Netherlands Dutch Research Council (NWO) as part of the NOISOURCE project (ALWTW.2016.008).

Keywords: vortex cavitation, water quality, three dimensional flow measurement, neural networks, computer vision

Printed by: Ipskamp Printing

Front & Back: Artist: Swaraj Nanda

Discover, invent, design and make.
[...]
Inveniāre, inventāre, dēsīgnāre et facere.
[...]
उद्भावनम्, आविष्कारः, निर्माणं च करोति।
[...]
Ontdekken, bedenken, ontwerpen en maken.

Contents

List of Figures

Summary

The research presented in this thesis aims at understanding how gases influence the cavitating vortex generated by a wing tip in a stationary flow. Gases in the flow occur as non-condensible microbubbles as well as gases dissolved in the liquid. They are typically abundant in surface flows. For studying how dissolved gases influence a cavitating vortex, a set of diffusion models are developed that predict how gases dissolved in water are transported into a vortex cavity. The predictions of the growth rate of a cavitating vortex using these models is then compared with the growth and development of a cavitating wing-tip vortex generated by a NACA $66_2 - (415)$ foil. The cavitating vortex is measured using single-view shadowgraph imaging in a cavitation tunnel. Some experimental practices on how the flow conditions are prepared prior to a measurement are also investigated, which is instructive in guiding experimental practices that promote repeatability of the results. A good agreement is achieved between the measured growth rate of the cavity, and that predicted by the diffusion models. The results also explain previously observed behavior of the development of a cavitating vortex from literature.

The results from these studies on the growth behavior of the cavitating vortex raise new questions on how the vortex kinematics, with respect to the viscous core size in particular, change during cavity growth, without a change in the flow parameters of the experiment, i.e., the Reynolds number, the cavitation number and the lift coefficient of the foil. In order to answer this question, it is necessary to apply experimental techniques that are capable of reconstructing the flow field around a vortex cavity. The three dimensional particle-tracking approach is found to be the most suitable measurement technique for this flow problem because in a particle tracking measurement, the instantaneous displacement of neutral tracer particles captures flow field information that is both well resolved in time as well as in space, circumventing any spatial averaging that occurs when correlation based approaches are applied to the flow problem. However, the application of particle tracking to the flow problem is not straightforward. This is primarily because tracer particles can hide behind the opacity of the cavity which blocks multiple camera views simultaneously. Furthermore, as the flow field is dominated strongly by axial velocity, a longer time trace over a particle track requires a larger axial length of the measurement volume. Moreover, recording scattered light from tracer particles over a large measurement volume poses a challenge to imaging as the illumination intensity drops drastically with the volume of the imaged region. Lastly, the cavity itself has a wandering motion due to both inherent cavity dynamics and turbulence in the flow field. In order to capture this motion, it is decided to reconstruct the axis of the vortex cavity simultaneously in three dimensions, increasing the challenges present in imaging the flow field around the vortex. Noting the aforementioned challenges, significant efforts are directed towards the development of an experimental setup which places all the cameras in the imaging system in forward scattering mode. A backlighting system is also introduced in the measurement system that visualizes the silhouettes of the cavity in each view, thus allowing a combination of

multi-view shadowgraph imaging and particle tracking in one measurement system. This allows reconstructing the shape of the cavitating vortex, which can further be used to reconstruct the axis of the cavitating vortex in order to correct wandering effects to the reconstructed flow field.

The developed imaging system yields good recordings of the particle images, and clear silhouettes of the vortex cavity are seen in each of the views. However, a particle reconstruction technique that takes into account the varying camera cover of a particle as it travels around the cavity is not readily available. Furthermore, as the images recorded from the measurement system are a combination of shadowgraph imaging and particle imaging, traditional image processing techniques cannot be readily applied to separate the silhouette information from the particle images. Noting these reconstruction challenges, a new particle reconstruction and tracking technique is developed that allows for variation in the camera cover of each particle. An image segmentation approach that utilizes deep learning techniques is applied to separate the silhouettes of the cavity from the recorded particle images with reasonable accuracy. This enables reconstructing the cavity in three dimensions using a voxel carving approach. The axis of the reconstructed cavity further enables the particle tracking approach by utilizing canonical vortex models to predict the next position of a reconstructed particle in the subsequent timestep. Once a data set of particle tracks are reconstructed, the recovered cavity axis also allows for the conditional averaging of particle displacements around the cavity, which corrects for the influence of vortex wandering, thus minimizing smearing effects on the profile of a vortex cavity in the conditionally averaged results.

Once the conditionally averaged velocity profiles of the flow around a cavitating vortex are extracted from the reconstruction data, it is possible to study the influence of the growth and development of the cavitating vortex on the azimuthal component of the vortex velocity profile. In the measurement campaign, two data sets are acquired which have similar inflow Reynolds numbers and cavitation numbers. Before comparing their vortex velocity profiles, a sensitivity study of the azimuthal component of the vortex profile is conducted which targets variations in the conditional averaging procedure due to changes in camera cover as well as physical location of the particles binned to produce the velocity profiles. The findings from this study are used to further guide the conditional averaging procedure that is used to study the kinematics of cavitating wing-tip vortices under influence of their growth and development due to water quality effects.

The vortex profiles reconstructed using the above steps are then compared against vortex models found in literature by fitting these models to the data. By both comparing the vortex model fit coefficients and comparing the vortex profiles at two different stages of growth, it is possible to construct a hypothesis on the influence of water quality effects on the vortex profile of a cavitating vortex, i.e., when it is developing in size alone. Some data contamination is also detected, which is attributed to influence by microbubbles. Overall, the measurements confirm the hypothesis adopted in the diffusion model developed in this study (Chapter 2), that the change in radius of a vortex cavity due to diffusion of dissolved gases alone does not change the kinematics of the vortex cavity.

Samenvatting

Het onderzoek dat in dit proefschrift gepresenteerd wordt, heeft tot doel uit te werken hoe gassen, aanwezig in de stroming als niet-condenseerbare microbellen, evenals gassen opgelost in het vloeibare medium, de caviterende werveling beïnvloeden die wordt gegenereerd door een stationaire vleugeltip. Om te bestuderen hoe opgeloste gassen een caviterende wervel beïnvloeden, is een set diffusiemodellen ontwikkeld die voorspellen hoe in water opgeloste gassen in een wervelholte worden getransporteerd. De voorspellingen van de groeisnelheid van een caviterende vortex met behulp van deze modellen worden vervolgens vergeleken met de groei en ontwikkeling van een caviterende vleugeltip vortex gegenereerd door een NACA $66_2 - (415)$ folie gemeten met behulp van single-view shadowgraph imaging in een cavitatie tunnel. Sommige experimentele praktijken over hoe de stromingsomstandigheden voorafgaand aan een meting worden voorbereid, worden ook onderzocht, wat leerzaam is bij het begeleiden van experimentele praktijken die de herhaalbaarheid van de resultaten bevorderen. Er wordt een goede overeenkomst bereikt tussen de gemeten groeisnelheid van de caviteit en die voorspeld door de diffusiemodellen. De resultaten verklaren ook eerder waargenomen gedrag van de ontwikkeling van een caviterende vortex uit de literatuur.

De resultaten van deze onderzoeken naar het groeigedrag van de caviterende vortex roepen nieuwe vragen op over hoe de vortexkinematica, in het bijzonder met betrekking tot de viskeuze kerngrootte, verandert tijdens de groei van de holte, zonder een verandering in de stromingsparameters van het experiment, d.w.z. het Reynoldsgetal, het cavitatiegetal en de liftcoëfficiënt van de folie. Om deze vraag te beantwoorden is het noodzakelijk om experimentele technieken toe te passen die in staat zijn het stromingsveld rond een wervelholte te reconstrueren. De driedimensionale deeltjesvolgbenadering blijkt de meest geschikte meettechniek te zijn voor dit stromingsprobleem, omdat bij een deeltjesvolgmeting de momentane verplaatsing van neutrale tracerdeeltjes stromingsveldinformatie vastlegt die zowel goed in tijd als in ruimte kan worden opgelost. , waarbij elke ruimtelijke middeling wordt omzeild die optreedt wanneer op correlatie gebaseerde benaderingen worden toegepast op het stromingsprobleem. De toepassing van het volgen van deeltjes op het stromingsprobleem is echter niet eenvoudig. Dit komt vooral omdat tracerdeeltjes zich kunnen verschuilen achter de ondoorzichtigheid van de holte die meerdere camerabeelden tegelijkertijd blokkeert. Bovendien, aangezien het stromingsveld sterk wordt gedomineerd door axiale snelheid, vereist een langere tijdsvolgorde over een deeltjesspoor een grotere axiale lengte van het meetvolume, en het opnemen van verstrooid licht van tracerdeeltjes over een groot meetvolume vormt een uitdaging voor beeldvorming aangezien de verlichtingsintensiteit daalt drastisch met het volume van het afgebeelde gebied. Ten slotte heeft de holte zelf een zwervende beweging als gevolg van zowel inherente holtedynamiek als turbulentie in het stromingsveld. Om deze beweging vast te leggen, is besloten om de as van de vortexholte gelijktijdig in drie dimensies te reconstrueren, waardoor de uitdagingen bij het in beeld brengen van het stromingsveld rond de vortex toenemen. Gezien de bovenge-

noemde uitdagingen, zijn er aanzienlijke inspanningen gericht op de ontwikkeling van een experimentele opstelling die alle camera's in het beeldvormingssysteem in voorwaartse verstrooiingsmodus plaatst. Er wordt ook een achtergrondverlichtingssysteem geïntroduceerd in het meetsysteem dat de silhouetten van de holte in elk beeld visualiseert, waardoor een combinatie van multi-view shadowgraph-beeldvorming en het volgen van deeltjes in één meetsysteem mogelijk wordt. Dit maakt het mogelijk de vorm van de caviterende wervel te reconstrueren, die verder kan worden gebruikt om de as van de caviterende wervel te reconstrueren om zwervende effecten op het gereconstrueerde stromingsveld te corrigeren.

Het ontwikkelde beeldvormingssysteem levert goede opnames van de deeltjesbeelden op en in elk van de weergaven zijn duidelijke silhouetten van de vortexholte te zien. Een techniek voor het reconstrueren van deeltjes die rekening houdt met de variërende cameradekking van een deeltje terwijl het door de holte reist, is echter niet direct beschikbaar. Aangezien de beelden die met het meetsysteem zijn opgenomen een combinatie zijn van schaduwbeeldvorming en deeltjesbeeldvorming, kunnen bovendien traditionele beeldverwerkingstechnieken niet gemakkelijk worden toegepast om de silhouetinformatie van de deeltjesbeelden te scheiden. Gezien deze reconstructie-uitdagingen, wordt een nieuwe deeltjesreconstructie- en volgtechniek ontwikkeld die variatie in de cameradekking van elk deeltje mogelijk maakt. Een beeldsegmentatiebenadering die gebruik maakt van deep learning-technieken wordt toegepast om de silhouetten van de holte met redelijke nauwkeurigheid te scheiden van de opgenomen deeltjesbeelden. Dit maakt het mogelijk om de holte in drie dimensies te reconstrueren met behulp van een voxel-carving-benadering. De as van de gereconstrueerde holte maakt verder de deeltjesvolgbenadering mogelijk door gebruik te maken van canonieke vortexmodellen om de volgende positie van een gereconstrueerd deeltje in de volgende tijdstap te voorspellen. Zodra een dataset van deeltjessporen is gereconstrueerd, maakt de herstelde holte-as ook de voorwaardelijke middeling van deeltjesverplaatsingen rond de holte mogelijk, wat corrigeert voor de invloed van vortexzwerven, waardoor uitsmeereffecten op het profiel van een vortexholte in de conditioneel worden geminimaliseerd. gemiddelde resultaten.

Zodra de conditioneel gemiddelde snelheidsprofielen van de stroming rond een caviterende vortex zijn geëxtraheerd uit de reconstructiegegevens, is het mogelijk om de invloed van de groei en ontwikkeling van de caviterende vortex op de azimutale component van het vortexsnelheidsprofiel te bestuderen. In de meetcampagne worden twee datasets verkregen met vergelijkbare instroom-Reynolds-getallen en cavitatiegetallen. Alvorens hun vortexsnelheidsprofielen te vergelijken, wordt een gevoeligheidsstudie van de azimutale component van het vortexprofiel uitgevoerd, die zich richt op variaties in de voorwaardelijke middelingsprocedure als gevolg van veranderingen in de cameradekking en de fysieke locatie van de deeltjes die zijn opgevangen om de snelheidsprofielen te produceren. De gevolgtrekkingen uit deze studie worden gebruikt om de voorwaardelijke middelingsprocedure verder te begeleiden die wordt gebruikt om de kinematica van caviterende vleugeltipwervelingen te bestuderen onder invloed van hun groei en ontwikkeling als gevolg van effecten op de waterkwaliteit.

De vortexprofielen die met behulp van de bovenstaande stappen zijn gereconstrueerd, worden vervolgens vergeleken met vortexmodellen die in de literatuur worden gevonden door deze modellen op de gegevens aan te passen. Door zowel de aanpassingscoëfficiënten van het vortexmodel te vergelijken als de vortexprofielen in twee verschillende groeistadia

te vergelijken, is het mogelijk een hypothese op te stellen over de invloed van waterkwaliteitseffecten op het vortexprofiel van een caviterende vortex, dat wil zeggen wanneer deze zich ontwikkelt in maat alleen. Er wordt ook enige dataverontreiniging gedetecteerd, die wordt toegeschreven aan beïnvloeding door microbellen. Over het algemeen bevestigen de metingen de hypothese die is aangenomen in de diffusiemodelontwikkelingsstudie die eerder in het werk is gepresenteerd, namelijk dat de verandering in straal van een vortexholte als gevolg van diffusie van opgeloste gassen alleen de kinematica van de vortexholte niet verandert.

1 Introduction

1.1 Background

1.1.1 Cavitation

A pure liquid comprises a collection of molecules that are held together at a certain separation distance by inter-molecular forces derived from an intermolecular potential energy ϕ^*, also called the Lennard-Jones potential [32, 33] (see figure 1.1). When an external tensile stress attempts to pull apart the molecules, the intermolecular force, which is the spatial derivative over this potential ($d\phi^*/dr^*$, r^* being the normalized distance between the molecules), is attractive, reaching a maximum at a certain separation distance denoted by the red line in figure 1.1. Beyond this separation distance, the external force overcomes the intermolecular attraction, causing a change in phase from a liquid to gas. The minimum external tensile stress to achieve this phase change is called the tensile strength of the liquid [14], and when this occurs due to a change in pressure, the process is called cavitation. Theoretically, a pure liquid can encounter cavitation at very high tensile strengths of the order of 10^2 MPa [8, 13, 17]. Practically speaking however, liquids cavitate at smaller tensile strengths. This is because in practical cases, liquids are contaminated by gases that are either dissolved in the liquid medium, or present as free gas bubbles, termed as nuclei, which reduce the tensile strength of the flow and act as local sites where cavitation begins, or incepts.

Naturally occurring liquids are often accompanied by impurities, therefore, cavitation is observed in a myriad of scenarios. A snapping shrimp uses cavitation to its advantage to stun its prey when hunting for food [49]. Cavitation is a known mechanism for traumatic brain injuries [21]. It is used by the medical industry as a means to locally deposit energy for a range of purposes such as for breaking up gall bladder stones (lithotripsy) and in cataract surgeries, among many other applications [15]. Central to these examples is the growth and collapse of spherical bubbles, which is captured in the Rayleigh-Plesset equation [42]. As a cavitation bubble encounters a region of higher pressure, it collapses, and pressures as high as 10^3 MPa can be expected in a liquid [24, 25]. When these high energies are deposited onto material surfaces, heavy damage and erosion to surfaces may be observed. This phenomenon is called cavitation erosion [45, 48]. The devastating consequences of cavitation erosion are often found in the spillways of hydroelectric powerplants [22], and

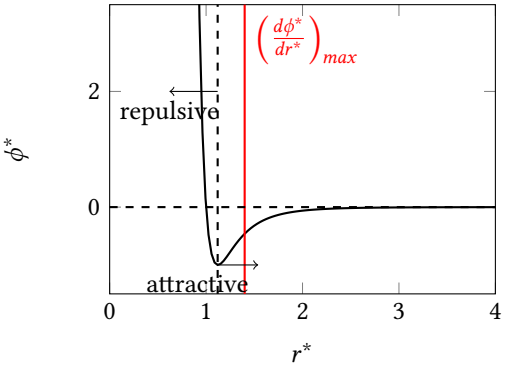

Figure 1.1: Normalized Lennard-Jones potential ϕ^* plotted against normalized intermolecular separation distance r^*, with attractive and repulsive intermolecular force regimes indicated at either sides of the minima of the potential ϕ^*. The red line indicates the r^* where $d\phi^*/dr^*$ is maximum in the attractive region of the potential, corresponding to the maximum attractive force between the molecules.

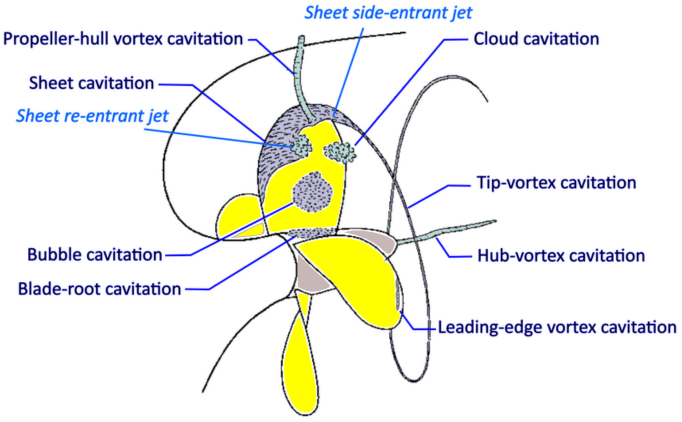

Figure 1.2: Types of cavitation found on a typical marine propeller. Adapted from [11].

in the erosion of marine propellers [11]. In fact, the term cavitation was inspired by its ability to cause thrust breakdown in marine propellers, discovered in the propellers of *SS Turbinia* in the 1890s, and gave rise to the design and construction of the first cavitation tunnel intended to study this phenomenon in greater detail [50]. From then on, propeller cavitation remains an important subject of research for over a century. More recently, there is a lot of attention for the Underwater Radiated Noise (URN) by cavitation as the adverse effects on the marine habitat.

Propeller cavitation is a special case of hydrodynamic cavitation that broadly describes a collection of cavitation phenomena occurring in various locations on a marine propeller as shown in figure 1.2. This is because the propeller is typically embedded in a highly non-uniform inflow behind the hull of a ship, exposing the sections of the rotating propeller blades to a highly unsteady angle of attack. Cavitation therefore occurs in various locations and forms [5]. Besides the previously stated erosive nature of collapsing cavitation bubbles, cavitation on propeller blades acts as a source of fatigue load in the transom region of a ship, forming a source of both broadband and tonal excitations in the frequency spectra of hull pressure fluctuations [9, 11]. Among the various cavitation phenomenon that can be

noted from figure 1.2, two types of propeller cavitation can be singled out that are the most common forms of cavitation and contribute toward underwater radiated noise and hull pressure fluctuations: sheet cavitation that occurs in the leading edge region of propeller blades (better described in [23]), and vortex cavitation that originates from the tip of the propeller blades, and forms a helicoidal structure downstream from the blade tips or the leading edge (see [4] for a review on vortex cavitation). These types of cavitation also cause increased levels of underwater noise radiated into the marine environment, with disruptive effects to marine fauna [34]. Among the two, tip-vortex cavitation can be considered more important, predominantly because it is present in marine propellers whenever the blade is loaded [40], and contributes the most to hull pressure fluctuation and noise [11]. Therefore, this phenomenon was chosen to be studied in this research.

1.1.2 Wing-Tip Vortex Cavitation

A feature of vortex cavitation is that it initiates, or incepts, at the core of the vortex when its pressure drops below the local vapor pressure of water. Tip vortices occur in hydrofoils as a consequence of the circulation generated by the foil and its finite size. Typically, vortex cavitation initiates in the tip region of the hydrofoil [36], and is highly sensitive to the amount of free gas bubbles, the relative velocity between the hydrofoil and the fluid, and the ambient pressure in the liquid.

A unique feature of tip vortex cavitation is the dynamic behavior of its vapor-liquid interface. These interface dynamics can be regarded as a superposition of a number of deformation modes (see [46]). Of these deformation modes, it is the external amplification of the first eigenmode (breathing mode) that gives rise to a peculiar phenomenon in tip-vortex cavitation, so called the *singing vortex* phenomenon [27]. It is thought that these deformations are present in cavitating propellers, where the radiation of noise into the underwater environment is observed, prompting an increase in fundamental research on understanding the source of propeller cavitation noise. Two recent works (experimental work in [40], and theoretical work in [11]) have shed a considerable amount of insight on the way the inherent dynamics of a vapor liquid interface can act as a source of narrow and broadband noise source. Bosschers [11] developed theoretical work on waves that occur on the surface of a vortex cavity, separating its dynamics into a number of deformation modes of the vortex interface, where each of the deformation modes has a wave length and frequency that is governed by the dispersion relation. He combined the fundamental work of Lord Thomson with sound spectra obtained from propellers with tip vortex cavitation, ultimately arriving at a relation between the natural frequency of the first deformation model (breathing mode) of the vortex at zero group speed. The corresponding frequency showed good correspondence to the centre frequency of an otherwise broadband radiated noise spectrum coming from the cavitating propeller. The work by Pennings [40] confirmed the hypothesized relation between the deformation modes and the radiated noise frequencies using both shadowgraph recordings and stereoscopic Particle Image Velocimetry [1].

One important finding from the aforementioned works is that the frequency of noise radiated by the cavitating tip vortex interface is sensitive to the size of the vortex cavity. As this is dependant on the water quality effects [16] where gas is transported into the vortex cavity from its surroundings, water quality plays an important role in determining

vortex cavitation noise as well.

1.1.3 Sensitivity of Wing-Tip Vortex Cavitation to Water Quality

The term water quality broadly describes the amount of gas, both dissolved and as free-gas nuclei, and solid contaminants present in the liquid medium, as well as its chemical composition. Of these, dissolved gas content and free-gas nuclei are two parameters that are most studied. Understanding the influence of water quality is an important research topic in cavitation research which is apparent from a large body of research that has been conducted on inception measurements across various experimental facilities [3, 6, 16, 18, 35]. Over the years, these measurement facilities have departed from conventional variable pressure water tunnels, and have specialized to cater to reducing sensitivities introduced by water quality [12, 37]. Despite the progress, open questions on scaling cavitation with water quality effects remain [7].

Undoubtedly the inception of vortex cavitation is an important field of study because it is the action of free gas bubbles growing and expanding at inception sites near the tip region of propeller blades that give rise to cavitation. The singing vortex phenomenon discussed previously was also shown to be sensitive to influence by water quality [39] in the specialized cavitation flow facility at Wuxi, China. That the influence of water quality on vortex cavitation noise is not well understood is shared by the two works described previously (the works by Bosschers [10] and Pennings [40]), but a greater share of investigations on water quality effects tends to occur on the topic of cavitation inception with recent works being that done on the topic of vortex cavitation inception by Khoo et al. [35, 36] at the Australian Maritime College cavitation tunnel. Consequently, there are questions on the stability of a vortex cavity due to dissolved gases present in its surrounding that has remained unresolved in cavitation literature.

It has been known for some time that when a vortex cavity is exposed to dissolved gases over a period of time, it develops in size due to diffusion of dissolved gases from the liquid medium into the cavity [16], without any change to the flow parameters set in the facility. When a vortex cavity, which is initially vaporous on inception, absorbs dissolved gases from the flow, its core pressure increases and it becomes resistant to shrinkage when inception conditions are removed, allowing the vortex cavity to persist at higher than inception ambient pressures. This phenomenon has been termed cavitation desinence and has been known to present itself in all kinds of cavitation observations studied in flow facilities [2, 29]. Diffusion is an important phenomenon to understand, especially when the population dynamics of free gas bubbles are well controlled in advanced flow facilities because the influence of gas diffusion becomes more pronounced. In fact, a very recent theoretical work utilised diffusion mechanisms to explain how gas pockets locked into crevices in the solid surfaces in a flow facility can give rise to a continuous formation of free-gas bubbles, particularly due to an enhanced rate of diffusion of dissolved gas into the gas pocket when a flow is present across the crevice [26]. These developments are encouraging, and necessitate reciprocation by extending our current understanding of gas diffusion into large scale cavitation, i.e., for vortex cavities. Therefore, the focus of this thesis is to expand the current understanding of gas transport in cavitation phenomenon to vortex cavitation.

1.1.4 Wing-Tip Vortex Kinematics and its Measurement

Because the conditions of cavitation inception lie in the magnitude of low pressure developed in the core of wing-tip vortices, the kinematics of cavitating vortices is an important topic of discussion in cavitation literature [20]. With regards to inception alone, the focus is on estimating the radius of the viscous core [28, 47], with special emphasis on scaling model test results to full scale propellers [30, 31, 44, 51]. The kinematics of a wing-tip vortex is fundamentally related to water quality because it strongly alters the path of microbubbles in the flow, which eventually leads to cavitation inception when nuclei approach an inception site under the right conditions and quantities. Even after the vortex cavitation initiates and develops, its kinematics once again play an important role in the ingestion of microbubbles in the flow, contributing to an increase in air, therefore pressure, inside the cavity, which leads to cavitation hysteresis. Furthermore, the distribution of the pressure field in a developing vortex cavity is also interesting to know because pressure is balanced across the interface during development, which can help construct diffusion models to explain vortex cavity development. The motion of the vortex cavity interface, derived by extrapolation from a vortex model, also appears as a parameter in estimating the motion of the vapor-liquid interface [9], which is needed to estimate the magnitude and frequency of noise radiated into the underwater environment. Therefore, studying the kinematics of a developed vortex cavity is the topic considered in this thesis.

It is remarkable to note here that measurement techniques that can be applied to probe the kinematics of cavitating vortices are generally applicable to single-phase flows and notoriously difficult to adapt to multiphase flows. This is due to a range of issues that occur with imaging particles around a vortex cavity. There is obstruction by vapor-liquid interfaces, specular reflections at the interface to illumination by laser based techniques, and wandering of the cavitating vortex itself that limits applicability of optical measurement techniques to cavitating vortices. This is discouraging because three-dimensional measurements of the flow around a vortex cavity can help reconstruct the fluctuating pressure field around a cavitating vortex, which can be further used to reconstruct noise from a cavitating vortex. By measuring the velocity profile around a vortex cavity when it develops due to gas diffusion, one can also understand how the kinematics of the cavity are affected by its growing size. Among other advantages, they can also help validate vortex models that describe a cavitating vortex. This thesis aims to mitigate these difficulties through further development of the measurement techniques.

1.2 Objectives, Scope and Thesis Structure

The main theme of this work is to investigate gas transport into cavitating wing-tip vortices, thus requiring the development of models and measurement techniques that augment prior knowledge in this field. Because the field of vortex cavitation is vast, we intentionally narrow down the scope of the present investigation to vortex cavities generated by a stationary hydrofoil set at a constant angle of attack. To make results more relatable to prior work, the NACA $66_2 - (415)$ elliptical foil used by Pennings [40] was used. Furthermore, the study presented in this work remains limited to experimental investigations only. Another important consideration is that the measurements conducted in this work were not repeated across other facilities, although this could have been a very useful exercise.

With this in mind, the objectives of this work are enumerated in the following. For

convenience, the scope of the related work is provided alongside the topic, and the objectives are listed in the order of appearance of the related work in this thesis:

1. (Chapter 2) *Develop a model for the transport of dissolved gases from the liquid medium into a cavitating vortex in order to explain the behavior of vortex cavitation growth as described, for example, by Briançon & Merle* [16].

   Scope: In this work, the influence of nuclei content was ignored in the development of the gas diffusion model. This means that the liquid contains quantities of microbubbles that are low enough for their contribution to the growth rate of the cavity (due to microbubble ingestion) to be observably negligible. The gas diffusion model was compared against experimental measurements performed using shadowgraph imaging at a low image acquisition frequency ($\mathcal{O}(1)$ Hz). The experimental setup is very similar to the work by Pennings [41], however, the shadowgraph imaging was performed using only one camera. This was deemed sufficient to survey the radius of the vortex cavity as it grew due to exposure to dissolved gases in the liquid medium.

2. (Chapter 3) *Develop a simultaneous three-dimensional cavity and velocity field reconstruction technique based on particle imaging and particle tracking that circumvents: (1) Opacity introduced by the cavity; (2) Specular reflections occurring at the vapor liquid interface; and (3) Wandering of the vortex.*

   Scope: The scope of application of this work is limited to cavitating vortices from stationary wing-tips primarily because a helicoidal propeller tip-vortex cavity dramatically increases reconstruction difficulty during the development stage. The measurement technique is limited to the simultaneous reconstruction of the velocity field around a vortex cavity and the visual hull of the vortex cavity, and no attempt is considered towards extending the developed technique to incorporate microbubble sizing. While the developed technique is readily extended to inception studies, the scope of the measurements are limited to answering questions on the influence of a growing vortex cavity on the kinematics of a vortex cavity. This means that the flow field parameters will be kept, as best as possible, at similar values, while the radius of the vortex cavity is allowed to expand to three different sizes, keeping the measurement matrix compact[1].

3. *(Chapter 4) From the datasets generated in chapter 3, investigate the influence of the changing size of a vortex cavity on the conditionally averaged velocity profile of a vortex cavity. This is because keeping the velocity profile of the vortex unchanged during the growth of the cavity's radius was a hypothesis used in the development of the diffusion model in chapter 3, which therefore needed to be supported with experimental evidence.*

   Scope: In this study, a collection of vortex models are assessed. Among these are the analytical and semi-empirical vortex models by Bosschers [11], the vortex model by Choi and Ceccio [19], and the vortex model by Proctor [43]. The development of cavitating-vortex models is not conducted in this work. Due to a small dataset size, the conclusions from this work address only some sensitivities in the reconstruction

[1] This was because the developed reconstruction technique was not optimised for speed, and one dataset containing 0.2 physical seconds of flow data took 3 months to reconstruct.

of the conditionally averaged velocity profiles, and support towards the assumptions made in chapter 2 on the behavior of the vortex profile during diffusion driven growth.

Each individual chapter contains a detailed review of literature on related works. The work in chapter 2 has been adapted to a journal paper which was recently published in the International Journal of Multiphase Flows [38], while the measurement technique developed in chapter 3 has been internally considered for a journal publication in combination with the insights in chapter 4. The conclusions from each chapter have been gathered and summarised in chapter 5. Additional conclusions on experimental practices that have been gathered from the experiences from this work have also been summarised. The thesis finally ends with a set of recommendations towards cavitation research community for subsequent investigations, advancements in measurement techniques, standardization of experimental practices and measurement facilities.

Bibliography

[1] Adrian, R. J. and Westerweel, J. (2011). *Particle image velocimetry*. Number 30. Cambridge university press, Cambridge, UK.

[2] Amini, A., Reclari, M., Sano, T., Iino, M., Dreyer, M., and Farhat, M. (2019). On the physical mechanism of tip vortex cavitation hysteresis. *Exp. Fluids*, 60(7):118.

[3] Arndt, R. and Keller, A. P. (1992). Water quality effects on cavitation inception in a trailing vortex. *J. Fluids Eng.*, 114(3):430–438.

[4] Arndt, R., Pennings, P., Bosschers, J., and Van Terwisga, T. (2015). The singing vortex. *Interface focus*, 5(5):20150025.

[5] Arndt, R. E. (2002). Cavitation in vortical flows. *Ann. Rev. Fluid Mech.*, 34(1):143–175.

[6] Arndt, R. E. and Maines, B. (1994). Vortex cavitation: A progress report. Technical report, American Society of Mechanical Engineers, New York, NY (United States).

[7] Atlar, M. (2002). The specialist committee on water quality and cavitation–final report. volume 2, Venice, Italy.

[8] Berthelot, M. (1850). *Sur quelques phénomènes de dilatation forcée des liquides*. impr. Bachelier.

[9] Bosschers, J. (2009). Investigation of hull pressure fluctuations generated by cavitating vortices. In *Proc. First Symp. Marine Propulsors*, Trondhiem, Norway.

[10] Bosschers, J. (2018a). An analytical and semi-empirical model for the viscous flow around a vortex cavity. *Intl. J. Multiphase Flow*, 105:122–133.

[11] Bosschers, J. (2018b). *Propeller tip-vortex cavitation and its broadband noise*. PhD thesis, University of Twente.

[12] Brandner, P., Lecoffre, Y., and Walker, G. (2007). Design considerations in the development of a modern cavitation tunnel. In *16th Australasian Fluid Mechanics Conference*, Gold Coast, Australia.

[13] Brennen, C. (1969). The dynamic balances of dissolved air and heat in natural cavity flows. *J. Fluid Mech.*, 37(1):115–127.

[14] Brennen, C. (2014). *Cavitation and bubble dynamics*. Cambridge University Press, Cambridge, UK.

[15] Brennen, C. (2015). Cavitation in medicine. *Interface focus*, 5(5):20150022.

[16] Briançon-Marjollet, L. and Merle, L. (1996). Inception, development and noise of a tip vortex cavitation. In *21st Symp. on Naval Hydrodynamics, Trondheim, Norway*.

[17] Caupin, F., Arvengas, A., Davitt, K., Azouzi, M. E. M., Shmulovich, K. I., Ramboz, C., Sessoms, D. A., and Stroock, A. D. (2012). Exploring water and other liquids at negative pressure. *J. Physics: Condensed Matter*, 24(28):284110.

[18] Chen, L., Zhang, L., Peng, X., and Shao, X. (2019). Influence of water quality on the tip vortex cavitation inception. *Phys. Fluids*, 31(2):023303.

[19] Choi, J. and Ceccio, S. (2007). Dynamics and noise emission of vortex cavitation bubbles. *J. Fluid Mech.*, 575:1–26.

[20] Dreyer, M., Decaix, J., Münch-Alligné, C., and Farhat, M. (2014). Mind the gap: a new insight into the tip leakage vortex using stereo-piv. *Exp. Fluids*, 55(11):1–13.

[21] Estrada, J. B., Scimone, M. T., Cramer, H. C., Mancia, L., Johnsen, E., and Franck, C. (2017). Microcavitation as a neuronal damage mechanism in an in vitro model of blast traumatic brain injury. *Biophysical journal*, 112(3):159a.

[22] Falvey, H. T. (1990). *Cavitation in chutes and spillways*. US Department of the Interior, Bureau of Reclamation Denver, CO, USA.

[23] Foeth, E. J. (2008). *The structure of three-dimensional sheet cavitation*. PhD thesis, Delft University of Technology.

[24] Franc, J.-P. (2007). The rayleigh-plesset equation: a simple and powerful tool to understand various aspects of cavitation. In *Fluid dynamics of cavitation and cavitating turbopumps*, pages 1–41. Springer.

[25] Franc, J.-P. and Michel, J.-M. (2006). *Fundamentals of cavitation*, volume 76. Springer science & Business media.

[26] Groß, T. and Pelz, P. (2017). Diffusion-driven nucleation from surface nuclei in hydrodynamic cavitation. *J. Fluid Mech.*, 830:138–164.

[27] Higuchi, H., Arndt, R., and Rogers, M. (1989). Characteristics of tip vortex cavitation noise. *J. Fluids Eng.*, 111(4):495–501.

[28] Holl, J., Arndt, R., and Billet, M. (1972). Limited cavitation and the related scale effects problem. In *Second Symp. Intl. Jap. Soc. Mech. Eng.*

[29] Holl, J. and Treaster, A. (1966). Cavitation hysteresis. *J. Basic Eng.*, 88(1):199–211.

[30] Hsiao, C.-T. and Chahine, G. L. (2005). Scaling of tip vortex cavitation inception noise with a bubble dynamics model accounting for nuclei size distribution. *J. Fluids Eng.*, 127(1):55–65.

[31] Hsiao, C.-T., Chahine, G. L., and Liu, H.-L. (2003). Scaling effect on prediction of cavitation inception in a line vortex flow. *J. Fluids Eng.*, 125(1):53–60.

[32] Jones, J. E. (1924a). On the determination of molecular fields.—i. from the variation of the viscosity of a gas with temperature. *Proc. Royal Society of London. Series A, Containing Papers of a Mathematical and Physical Character*, 106(738):441–462.

[33] Jones, J. E. (1924b). On the determination of molecular fields.—ii. from the equation of state of a gas. *Proc. Royal Society of London. Series A, Containing Papers of a Mathematical and Physical Character*, 106(738):463–477.

[34] Jones, N. (2019). Ocean uproar: saving marine life from a barrage of noise. *Nature*, 568:158–161.

[35] Khoo, M., Venning, J., Pearce, B., and Brandner, P. (2020). Statistical aspects of tip vortex cavitation inception and desinence in a nuclei deplete flow. *Exp. Fluids*, 61:1–13.

[36] Khoo, M., Venning, J., Pearce, B., and Brandner, P. (2021). Nucleation and cavitation number effects on tip vortex cavitation dynamics and noise. *Exp. Fluids*, 62(10):1–19.

[37] Lecoffre, Y., Chantrel, P., and Teiller, J. (1988). Le grand tunnel hydrodynamique (gth). *La Houille Blanche*, 74(7-8):585–592.

[38] Nanda, S., Westerweel, J., van Terwisga, T., and Elsinga, G. (2022). Mechanisms for diffusion-driven growth of cavitating wing-tip vortices. *Intl. J. Multiphase Flow*, 156:104146.

[39] Peng, X., Xu, L., Song, M., and Cao, Y. (2015). Vortex singing in tip vortex cavitation under the effect of water quality. In *J. Physics: Conference Series*, volume 656, page 012185. IOP Publishing.

[40] Pennings, P. (2016). *Dynamics of vortex cavitation.* PhD thesis, Delft University of Technology.

[41] Pennings, P., Westerweel, J., and van Terwisga, T. (2016). Cavitation tunnel analysis of radiated sound from the resonance of a propeller tip vortex cavity. *Intl. J. Multiphase Flow*, 83:1–11.

[42] Plesset, M. S. (1949). The dynamics of cavitation bubbles. *J. Appl. Mech.*, 16(3):277–282.

[43] Proctor, F. (1998). The nasa-langley wake vortex modelling effort in support of an operational aircraft spacing system. In *36th AIAA Aerospace Sciences Meeting and Exhibit*, page 589.

[44] Shen, Y. T., Gowing, S., and Jessup, S. (2009). Tip vortex cavitation inception scaling for high reynolds number applications. *J. Fluids Eng.*, 131(7):071301.

[45] Sreedhar, B., Albert, S., , and Pandit, A. (2017). Cavitation damage: Theory and measurements–a review. *Wear*, 372:177–196.

[46] Thomson, W. (1880). 3. vibrations of a columnar vortex. *Proc. Royal Society of Edinburgh*, 10:443–456.

[47] van Rijsbergen, M. and Kuiper, G. (1997). Modeling a cavitating vortex. In *Proc. ASME Fluids Eng. Division Summer Meeting, Vancouver, British Columbia, Canada.*

[48] van Terwisga, T., Li, Z.-r., Fitzsimmons, P., and Foeth, E. J. (2009). Cavitation erosion-a review of physical mechanisms and erosion risk models. In *Proc. Intl. Cavitation Conf.*, pages 1–13, Ann Arbor, Michigan, USA. University of Michigan.

[49] Versluis, M., Schmitz, B., Von der Heydt, A., and Lohse, D. (2000). How snapping shrimp snap: through cavitating bubbles. *Science*, 289(5487):2114–2117.

[50] Young, F. R. (1999). *Cavitation.* World Scientific.

[51] Zhang, L. X., Zhang, N., Peng, X. X., Wang, B. L., and Shao, X. M. (2015). A review of studies of mechanism and prediction of tip vortex cavitation inception. *J. Hydrodynamics*, 27(4):488–495.

2

Mechanisms for Diffusion Driven Growth of Cavitating Wing-Tip Vortices[1]

Following their inception, vortex cavities emanating from stationary wing tips in cavitation tunnels are often observed to grow. These effects are usually attributed to the free and dissolved non-condensable gases in the liquid. However, a detailed mechanism for the cavity's growth is not known. Consequently, the repeatability of vortex cavitation in different flow facilities is generally poor. The main aim of our work is to highlight the contribution of dissolved gases to the cavity's growth, hence addressing water-quality influence in nuclei-depleted conditions. A model is provided for a steady-state diffusion-driven mechanism that transports dissolved gases from the surrounding liquid into the vortex cavitation through a diffusion layer located outside its interface. The model results show that the cavity grows uncontrollably when the dissolved gas concentration in the liquid is saturated or oversaturated relative to its saturation level at ambient pressure conditions ($c_\infty/c_{sat} \geq 1$). In addition, it is shown that stable cavity sizes can be achieved when the $c_\infty/c_{sat} < 1$. The predictions in the range $1.04 \leq c_\infty/c_{sat} \leq 1.33$ are compared with experimental data and infer either of the two geometries for the diffusion layer: (i) a 5 μm thin film approximated by a hollow cylinder around the cavity, or (ii) one that evolves like a boundary layer along the axis of the cavity. For the latter modeling approach, the observed length of the cavity was much larger than that required to match with the experimental data, skewing a preference to the thin-film assumption. In the undersaturated regime ($c_\infty/c_{sat} = 0.14$ & 0.39), the proposed model has a qualitative agreement with the data of [13].

[1]This chapter has been published in Nanda, S., Westerweel, J., van Terwisga, T., & Elsinga, G. (2022). Mechanisms for diffusion-driven growth of cavitating wing-tip vortices. International Journal of Multiphase Flow, 156, 104146. doi: https://doi.org/10.1016/j.ijmultiphaseflow.2022.104146

2.1 Introduction

Tip Vortex-cavitation is a form of hydrodynamic cavitation that initiates when the low-pressure core of the vortex shed by a lifting-body approaches the local vapor pressure of water [5, 12, 17], resulting in the formation of dynamic vapor-liquid structures. An important feature of vortex-cavitation stems from the dynamics of its interface [44] that causes a fluctuating pressure field in its surrounding, acting as a source of fatigue load to the hull structure, as well as a source of sub-kilohertz, tonal, radiated noise into the underwater environment [9]. The resulting disruption to the global marine habitat has been reported by various studies [22, 34], and, this phenomenon has been studied extensively by conducting observations in cavitation tunnels [2, 30, 32, 47]. One point of contention is that cavitation facilities vary one from another, sometimes in the volumetric water capacity of the tunnel, or the achievable Reynolds and cavitation number of the flow. More importantly, cavitation tunnels vary in their ability to control the water quality content, here identified by the amount of free gas bubbles, or nuclei, and gases dissolved within the fluid. As a result, repeatability of cavitation observations across facilities is often poor [6].

In the case of vortex cavitation inception, water-quality effects are largely dominated by the distribution of nuclei bubbles in the flow [3, 4, 36, 39]. However, immediately following inception when the cavity is saturated with water vapor at its vapor pressure, a higher concentration of dissolved-air in the liquid adjacent to its boundary will initiate a mass-transfer process across the boundary, causing the pressure inside the vortex cavity to increase. The resulting vaporous cavitation will transition to gaseous cavitation, and due to continued mass transfer of gases into the cavity, the cavity radius will increase over time. In order to terminate this growth process, the concentration difference across the vapor-liquid boundary should be bridged. But how long is this development period? What is the rate at which this development occurs and what are the physical quantities most important to this phenomenon? Under what conditions does a vortex cavity achieve a stable size? Answers to these questions are unclear. Clearly, a phenomenological picture of the stability of a vortex cavity size following inception, as influenced by water quality effects, is necessary. In the present work, we separate the influence of the nuclei content in the flow by considering only those cases where the nuclei population in the flow is low enough to be inconsequential to our observations.

2.1.1 Related Works on Dissolved Gas Diffusion Modeling

One of the first theoretical models on the mass transfer of dissolved gases into bubbles was developed by [25]. They studied the growth and dissolution of microbubbles theoretically by assuming that the gas concentration in the bubble and on its surface are saturated relative to its internal pressure. The mass-transfer mechanism is approximated as an unsteady diffusion process analogous to heat conduction in spheres. This is used to estimate a radial concentration profile which ultimately equalizes with the ambient dissolved gas concentration far away from the bubble interface. They also considered the influence of surface tension by incorporating the pressure balance at the interface, and their predictions are in good agreement with dissolution times observed for microbubble radii less than 15 μm and a surface tension range of 25 to 72 mN/m [23].

In contrast to gas diffusion in stationary bubbles, hydrodynamic cavitation often occurs in the vicinity of high flow velocities, where convective components cannot be readily

ignored and Peclet numbers are high. In this regard, a convective diffusion mechanism was proposed by [48] for microbubble growth rates observed in the wakes of flow-facing objects by [35]. The convective diffusion modeling approach has also been useful in describing the growth and shedding of microbubble nuclei from gas pockets attached to surface crevices [29]. In this case and the prior case, where the microbubble is embedded in a turbulent flow, the relative motion of the surrounding flow to the interface indeed merits the inclusion of a convective component in the growth mechanism. Yet another bubble growth mechanism is rectified diffusion [24, 26] which accounts for the non-linear mass transfer of air across a bubble interface induced by an oscillating boundary. This modeling approach may be relevant to the vortex cavity whose interface dynamics could act as a non-linear mass transfer component. While this is a consideration, the diffusion layer morphology for this flow problem is yet to be established and will be elaborated in §2.1.2.

Gas diffusion is also known to affect cavitation phenomenon in larger scales as well. [33] connected the presence of dissolved gases to cavitation hysteresis observed in large developed cavities generated behind flow facing objects [27, 31] and [11] proposed the first mass transfer model for the diffusion of dissolved gases into large axisymmetric cavities. In this model, the mass transfer mechanism was approximated as a two-dimensional, steady state, convective diffusion mechanism occurring over a potential flow background. However, an extension of this solution to three-dimensional cavities by wrapping the two-dimensional model around the cavity, as done by [7], over-predicted the observed growth rate by one order of magnitude. [41] tried to resolve the discrepancy by adopting a turbulent diffusivity obtained from a mixing-length model and showed that the mass-transfer region that contributes to the most mass-flux resides near the frontal region of the cavity, where the concentration gradient at the surface has the highest magnitude. They also showed that a wrap-around solution closely approaches an axisymmetric solution with acceptable loss of accuracy.

More recently, [49] and [38] applied the available convective-diffusion models to limited partial cavities [32], observed using x-ray measurements. They found the proposed models [7, 11, 41] to be ineffective in predicting the bubbles sizes left in its wake. Surprisingly, they were able to scale the order-of-magnitude of growth rates observed by assuming a cumulative molecular diffusion (following [25]) into an assumed monodisperse population of the average microbubble size within the partial cavity. To us, the result reaffirms the role of molecular diffusion in the mass transfer of dissolved gases into bubbles. In the following discussion, we try to motivate the role of molecular diffusion for vortex cavities as well.

2.1.2 Related Works For Vortex Cavitation Flows

In contrast to the experimental and theoretical works present for nucleation and partial cavitation, literature on vortex cavitation growth and development due to dissolved gases in its surrounding is not extensive. Some reasons for this could be the following: (1) Cavitation tunnels water quality management is non-standardized across facilities; (2) Vortex cavitation sound has a greater emphasis than water quality sensitivity, whose high frequency dynamics lead to a small observation duration, typically of $\mathcal{O}(1)$ seconds; and, (3) Experimentation practices for generating the vortex cavity are not adequately described. In order to allow the cavity to develop, or grow, to a *quasi-stable* size, it is common to have an arbitrary buffer time between inception and observation [1, 21, 43]. In the absence

	σ [-]	U_∞ [m/s]	p_∞ [$\times 10^5$ Pa]	Dissolved-air [% a.s. re 1 atm]	c_∞/c_{sat} [-]	Nuclei-Seeding [-]	Δt [sec]	Δr_c [mm]	F_m [-]
1	4.1	10	2.07	30	0.14	Large nuclei	1,548	10.30	0.03
2	4.1	10	2.07	80	0.39	No seeding	332	3.39	0.26
3	2.9	6	0.54	30	0.56	No seeding	590	1.73	0.40
4	2.9	6	0.54	30	0.56	Small nuclei	1,374	3.98	0.17

Table 2.1: Estimates of F_m from data found in [13]. σ is the reported cavitation number, U_∞ is the reported inflow velocity and p_∞ is the ambient pressure estimated using a vapor pressure of 2 kPa and water density of 1 g/cm^3. The relative saturation level (c_∞/c_{sat}) is reported relative to saturation conditions c_{sat} at the estimated test section pressure p_∞. c_{sat} is calculated from the estimated ambient pressure and using Henry's law with Henry's constant for air being 0.223×10^{-6} kg/m^3Pa. The binary diffusion constant is taken to be 2×10^{-9} m^2/s.

of a standardized measurement practice, where the exposure time of the vortex cavity to its surroundings is categorized and its influence is understood, the observer is likely to perceive a slowly developing cavity to be stable. This introduces observer specific biases into the measurements.

To the best of our knowledge, long-time observations of the size of vortex-cavities have only been reported by [13] for their measurements at the GTH facility [37], indeed showing a growing vortex cavity radius following its inception. In some of these measurements, the water-tunnel was operated in nuclei-depleted conditions, still showing an appreciable growth rate of the vortex cavity size. Table 2.1 reproduces some of their measurements by calculating the change in cavity radius (Δr) over its growth duration (Δt), characterized using the non-dimensional mass-transfer Fourier number F_m. Here $F_m = \Delta t D/(\Delta r_c)^2$, where D is binary diffusion coefficient for the solute-solvent configuration, here air-water. The mass Fourier number as defined here compares the magnitude of the growth rate of the cavity in a given period with the molecular diffusion for that gas-liquid configuration, with a value approaching $\mathcal{O}(1)$ identified as a strongly diffusion dominated phenomenon.

For some cases in table 2.1, it is observed that a flow where the nuclei population is moderate to none results in a F_m value only one order of magnitude below $\mathcal{O}(1)$ indicating that the growth mechanism could be diffusion driven. At the same time, one also observes that an increased presence of nuclei-content increases the growth rate, leading to smaller F_m values. This suggests that the growth rate of a cavitating vortex may be sensitive to large nuclei population density in the water-tunnel. However, besides establishing an order-of-magnitude wise connection to molecular diffusion, conclusions made on the effect of the ambient relative air-saturation level (c_∞/c_{sat}) to the growth rate are limited. Here, c_∞ is the ambient air-concentration with units of density, while c_{sat} is the air-concentration of the fully saturation solution at the tunnel's ambient pressure conditions.

Numerical simulations of vortex-cavitation typically do not consider the influence of dissolved gases for the slow growth rates attributed to them. Instead, Euler-Lagrangian models of nuclei entrainment as a mechanism for the growth of vortex-cavities has been considered in a recent numerical work by [16]. The modeling involves a modification of the Schnerr-Sauer cavitation model [45], assuming the presence of non-condensable gas as a monodisperse spherical bubble population, disregarding the influence of dissolved air entirely. Theoretical work on the entrainment of nuclei into vortices has been considered by, for example, [40, 50], and more recently by [15]). When the number of free gas bubbles is strongly reduced, one can consider that the mass flow rate of gas into the cavity by

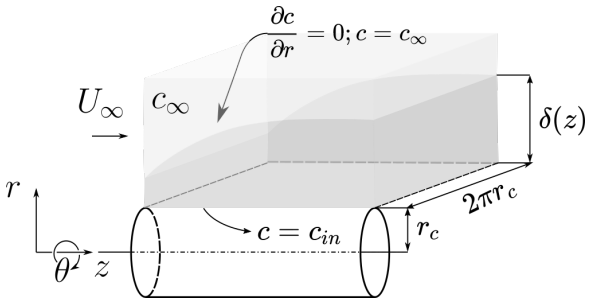

Figure 2.1: A schematic description of the convective-diffusion model found in [1]. c_{in} is the concentration of air at the cavity interface on the vapor-side and c_∞ is the dissolved air content in the ambient liquid. The region where the concentration gradient develops is marked as dark gray, where $\delta(z)$ refers to the concentration boundary layer thickness along the axial direction, and $\delta(z) \ll r_c$. The unwrapped tangential coordinate is depicted as a planar three-dimensional extrusion over a length $2\pi r_c$.

nuclei entrainment is negligible compared to that by diffusion. From our discussion of the results of [13], it is clear that gas-diffusion is important to vortex-cavitation phenomenon, particularly in nuclei depleted conditions. While the influence of dissolved gases on the growth rate and stability of the cavity size remains unknown to this present date, there has been an attempt to model the growth rate of a tip-vortex cavity using the convective-diffusion approach.

Recently, [1] have proposed a convective-diffusion mechanism (see fig. 2.1) using the two-dimensional potential-flow diffusion model discussed by [11]. In this approach, the governing transport equation for the single species dissolved gas-concentration, c (with units of density), given by:

$$\left[\frac{\partial c}{\partial t}\right]_I + \left[u \cdot (\nabla c)\right]_{II} = \left[D\nabla^2 c\right]_{III} \tag{2.1}$$

can be simplified considering (i) two-dimensionality in a cartesian frame, (ii) no accumulation of mass in the diffusion layer (negligible term I of eq. (2.1)), (iii) negligible radial velocity of the cavity, (iv) axisymmetry, and, (v) no axial diffusion component given that the Peclet number is large. $Pe = U_\infty l_c/D$, where U_∞ is the axial flow speed, and l_c the length of a section of the vortex cavity. This gives:

$$U_\infty \frac{\partial c}{\partial z} \approx D\frac{\partial^2 c}{\partial r^2}. \tag{2.2}$$

Over the length of the cavity, the radial concentration profile of dissolved gas is assumed to evolve in a self-similar manner. The two-dimensional solution is wrapped around a cylindrical geometry with negligible loss of accuracy compared to a fully axisymmetric model as shown by [41]. The resulting total mass-transfer rate of gas into a longitudinal segment of the cavity, $\dot{m}$, is then derived by [1] as:

$$\dot{m}_{CD} \approx 4r_c(c_\infty - c_{in})\sqrt{\pi U_\infty D l_c}. \tag{2.3}$$

One missing aspect of eq. (2.3) is its connection to the increasing total pressure inside the cavity. This is because, if a *quasi-steady* growth-behavior as motivated by the observations of [13] and those reported here (see §2.3) is assumed, an interfacial pressure balance of the following form must be obeyed during the growth stage:

$$\left[p_{in}^G(t) + p_{vap}\right]_c = \left[\{p_\infty + p_c(r_c)\} + p_\mathcal{T}(r_c)\right]_l \tag{2.4}$$

where p_{in}^{G} is the time-dependant pressure of air inside the cavity, p_{vap} the vapor pressure of water, p_∞ the ambient pressure, p_c the radial pressure distribution of the vortex relative to p_∞, and $p_\mathcal{T}$ the contribution of surface tension due to curvature in circumferential direction. One uncertainty with combining the mass-transfer rate of eq. (2.3) with the pressure balance across the interface eq. (2.4) is that the concentration profile inside the cavity is unknown and must be assumed. Secondly, within an analytical or semi-empirical framework, the radial-pressure at the interface, $p_c(r_c)$, requires a vortex-model that is suited to cavitating flows. Therefore, one is not sure if the potential flow convective-diffusion approach yielding eq. (2.3) is the only mechanism that describes diffusion driven growth of the vortex cavity.

To tackle the challenge of scaling the size of a vortex cavity using the dissolved gas content, the flow Reynolds number and cavitation number, it is first important to understand how gas is transported into the cavity from dissolved gas present in its surrounding. In this work, we propose that in the absence of nuclei this mechanism is strongly diffusion driven. We approximate the wing-tip vortex cavity as a line vortex and apply different modeling assumptions to arrive at an estimate of the cavity growth rate, which we compare with experiments. We generate the cavitating tip-vortex using a NACA 66_2-415 elliptical foil, similar to [42] and conduct long-time observations (> 5 minutes) of the development phase of a vortex cavity.

2.1.3 Outline

This chapter is structured as follows: In §2.2 we examine the potential-flow convective-diffusion mass transfer approach to vortex cavity growth rates, and, propose additional mass-transfer mechanisms for the same. We also connect these mass-transfer rates to the growth rate of the cavity by incorporating the *quasi-steady* pressure-balance at the cavity's interface (eq. (2.4)). In §2.3 our experimental investigation is detailed where a special emphasis is placed on the measurement procedure to obtain repeatable results in a low-volume cavitation tunnel. Our experimental results, compared with the different growth rate models, are highlighted and discussed in §2.4. The chapter then closes with the conclusion in §2.5.

2.2 Modeling

In all our modeling attempts, we assume that the mass-transfer rate estimated at the liquid side of the interface results in a uniform growth in the cavity-radius along its length. The assumption of uniform cavity growth is motivated primarily by our own experimental observations, discussed later in §2.3.1 and in figure 2.4. In §2.2.1, we use this assumption in the estimation of the growth-rate of the cavity radius, which is equated to three different mass-transfer models that we describe in §2.2.2, with one of the models being the convective-diffusion model used by [1]. Some distinguishing features of the mass-transfer models are described in §2.2.2.4, and finally some comments on the choice of different vortex-models in the growth-rate expressions are given in §2.2.2.5.

The modeling has been performed for conditions following inception of the vortex cavity, and before the eventual unstable state observed in each cavitation measurement in oversaturated conditions, later described in figure 2.4 and its accompanying discussion. In

this growth period, the primary assumption made is that the radial velocity of the cavity interface is negligible relative to the expected azimuthal velocity of the fluid in its vicinity. Therefore, we consider the growth behavior to be quasi-steady.

2.2.1 Cavity Growth Rate Expression for Purely Radial Growth in Size

Consider the vortex cavity as a cylinder of constant length l_c, ignoring the endcaps and with radius $r_c(t)$. As the circulation is proportional to the lift generated by the wing, which does not change during the measurements, the ambient circulation strength of the vortex, Γ_∞, is taken constant. Assuming that the transported gas is ideal and in isothermal conditions, then, for any temperature T, where M_G is the molecular mass and R the ideal gas constant, the density $\rho^G_{in}(t)$ equals $p^G_{in}(t)M_G/RT$. This can be substituted into the pressure balance expression of eq. (2.4) as follows:

$$\rho^G_{in}(t) = \tau\{p_\infty + p_c(r_c) + p_\mathcal{T}(r_c) - p_{vap}\} \tag{2.5}$$

where $\tau = M_G/RT$. Furthermore, the mass of the gas contained inside a cavity of length l_c is given by:

$$m^G_{in}(t) = (\pi r_c^2)\rho^G_{in}(t)l_c \tag{2.6}$$

Taking the time derivative of eq. (2.6), the mass-transfer rate per unit length of the cavity is given by the following expression:

$$\begin{aligned}\frac{1}{l_c}\frac{dm^G_{in}}{dt} &= \frac{d}{dt}[(\pi r_c^2)\rho^G_{in}(t)] \\ &= 2\pi r_c \rho^G_{in}(t)\frac{dr_c}{dt} + \pi r_c^2 \frac{d\rho^G_{in}(t)}{dt}\end{aligned} \tag{2.7}$$

The term $d\rho^G_{in}(t)/dt$ contains $p_c(r_c)$ and $p_T(r_c)$ which is expanded using the chain rule and substituted into eq. (2.7), yielding:

$$\frac{1}{l_c}\frac{dm^G_{in}}{dt} = 2\pi r_c \frac{dr_c}{dt}\left[\rho^G_{in}(t) + \frac{\tau r_c}{2}\left(\frac{dp_\mathcal{T}}{dr_c} + \frac{dp_c}{dr_c}\right)\right] \tag{2.8}$$

Eq. (2.8) gives the rate of change in mass of gas inside the cavity which can then be equated to a mass-transfer model. For a purely radial diffusion, the mass introduced into the cavity per unit length and per unit time is given by the expression:

$$\frac{1}{l_c}\frac{dm^G_{in}}{dt} = 2\pi r_c D\left(\frac{\partial c}{\partial r}\right)_{r_c}. \tag{2.9}$$

Here, D is the binary diffusion coefficient between liquid and gas while $(\partial c/\partial r)_{r_c}$ is the concentration gradient at the cavity interface. From eq. (2.8) and eq. (2.9), we have:

$$2\pi r_c D\left(\frac{\partial c}{\partial r}\right)_{r_c} = 2\pi r_c \frac{dr_c}{dt}\left[\rho^G_{in}(t) + \frac{\tau r_c}{2}\left(\frac{dp_\mathcal{T}}{dr_c} + \frac{dp_c}{dr_c}\right)\right].$$

Finally, the above is rearranged to yield the expression for cavity growth rate due to diffusion of ambient dissolved gases into the cavity:

$$\frac{dr_c}{dt} = \frac{D\left(\frac{\partial c}{\partial r}\right)_{r_c}}{\left[\rho_{in}^{G}(t) + \frac{\tau r_c}{2}\left(\frac{dp_\tau}{dr_c} + \frac{dp_c}{dr_c}\right)\right]}. \tag{2.10}$$

Eq. (2.10) is a first-order differential equation describing the cavity growth rate, requiring the modeling of mass-transfer through the $(\partial c/\partial r)_{r_c}$ term and a vortex-model for the pressure gradient term $(\partial p_c/\partial r_c)$.

2.2.2 Mass-transfer Modeling

Mass-transfer Considering a Convective-Diffusion Process

As described by [1], the convective-diffusion model takes a two-dimensional, cartesian representation of eq. (2.1) in the axial and radial direction, assumes a steady-state diffusion process, negligible radial velocity, axial velocity equal to freestream, a large Peclet number, and a self similarly evolving concentration profile in the diffusion layer that scales with $\sqrt{Dz/U_\infty}$ as shown in figure 2.1. These approximations reduce the concentration transport equation to eq. (2.2). The expression for the mass-transfer rate of dissolved-gas into the cavity, neglecting the end-caps of the cylinder, is obtained by integrating the local mass-transfer rate per unit area over its length, l_c, yielding a mass-transfer rate given by eq. (2.3). In order to derive a growth rate expression for a developing cavity using the convective-diffusion approach, the mass-transfer rate in eq. (2.3) can be substituted to eq. (2.8) to yield the following approximate first-order ordinary differential equation:

$$\frac{dr_c}{dt} = \frac{\left(c_\infty - c_{in}\right)}{\left[\rho_{in}^{G}(t) + \frac{\tau r_c}{2}\left(\frac{dp_\tau}{dr_c} + \frac{dp_c}{dr_c}\right)\right]}\left[\sqrt{\frac{4DU_\infty}{\pi l_c}}\right]_{U_D^{cd}} \tag{2.11}$$

The component of eq. (2.11) highlighted by subscript U_D^{cd} (where the superscript *cd* denotes convective-diffusion) has the units of velocity and scales with the diffusion velocity of dissolved gas across the interface. We make this distinction for the explicit purpose of comparing the behavior of the diffusion model discussed here, in §2.2.2.3 and in §2.2.2.2. We revisit this diffusion velocity term in §2.2.2.4 and in the results section, §2.4. Likewise, the denominator of eq. (2.11) excluding U_D^{cd} has units of density and can be thought to scale with the density of the gas molecules at the interface location. This is governed by the balance between partial gas-pressure inside the cavity, the dynamic pressure at the interface described by a vortex-model and a surface-tension component due to curvature in the azimuthal direction alone.

Mass-Transfer Through a Thin Diffusion-Layer Approximated as a Hollow Cylinder

If the diffusion layer has no relative motion with respect to the surrounding flow, the radial velocity is negligible, the transport is steady and axisymmetric and the diffusion layer has

a constant thickness δ_f along its length, with the condition that $r_c \gg \delta_f$ (see fig. 2.2), then eq. (2.1) is reduced to:

$$\frac{D}{r}\frac{\partial}{\partial r}\left(r\frac{\partial c}{\partial r}\right) \approx 0. \tag{2.12}$$

In this case, the diffusion coefficient would be that of air in water. In order to obtain solutions to the above equation, the concentration field on either side of the diffusion film is assumed to be uniform along both the axial and radial direction. If the measured concentration of dissolved gas (G) in the liquid outside the diffusion layer is given by c_∞, and, the concentration on the inner wall of the layer is given by c_{in} which increases with time, the solution to eq. (2.12) is analogous to that of heat flux through hollow infinite cylinders. Then, the concentration profile inside the cavity interface ($c(r)$) is given by the steady-state analytical solution (see [19]):

$$c(r) = \left(ln\left(1+\frac{\delta_f}{r_c}\right)\right)^{-1}\left[c_\infty ln\left(\frac{r}{r_c}\right) + c_{in} ln\left(\frac{r_c+\delta_f}{r}\right)\right]; r \in [r_c, r_c+\delta_f] \tag{2.13}$$

which gives us the concentration-gradient at the inner wall of the diffusion film:

$$\left(\frac{\partial c}{\partial r}\right)_{r_c} = \frac{1}{r_c}(c_\infty - c_{in})\left(ln\left(1+\frac{\delta_f}{r_c}\right)\right)^{-1}. \tag{2.14}$$

Finally, substitution of eq. (2.14) into eq. (2.10) results in:

$$\frac{dr_c}{dt} = \frac{c_\infty - c_{in}}{\left[\rho^G_{in}(t) + \frac{\tau r_c}{2}\left(\frac{dp_\tau}{dr_c} + \frac{dp_c}{dr_c}\right)\right]}\left[\frac{D}{r_c}\left(ln\left(1+\frac{\delta_f}{r_c}\right)\right)^{-1}\right]_{U_D^{tf}}, \tag{2.15}$$

where, U_D^{tf} (superscript tf denoting thin-film) scales with the diffusion velocity of the dissolved gas at the cavity surface. While this appears to be a function of the cavity radius, the above expression can be simplified by considering a Taylor expansion of the term $ln\left(1+\delta_f/r_c\right)$, to the first order, considering $\delta_f/r_c \ll 1$. This gives the following approximation to U_D^{tf}:

$$U_D^{tf} \approx D/\delta_f \tag{2.16}$$

Heat-Conduction Analogue

In similar fashion as [25], one may assume the diffusion mechanism to be transient. The concentration profile outside the cavity radius is assumed to be uniform, and the radial distance from the cavity axis to the interface is the region that contains the concentration gradient. Therefore, the concentration gradient at the interface decides the mass-transfer rate. In contrast to the models introduced previously, the location of the diffusion region is inside the cavity, which necessitates an unsteady state mass-transfer process because mass accumulation within the cavity must be considered. If the internal concentration profile is assumed to be axisymmetric, axially invariant, and, convection is ignored in a manner similar to 2.2.2.2, eq. (2.1) simplifies to:

$$\frac{\partial c}{\partial t} \approx \tilde{D}\frac{\partial^2 c}{\partial r^2} \tag{2.17}$$

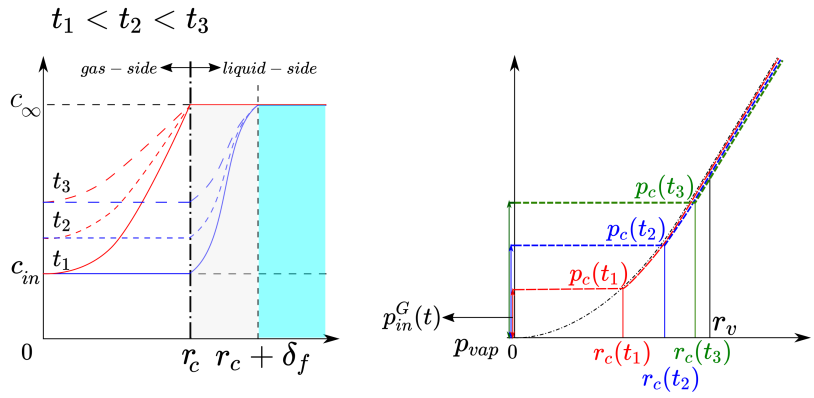

Figure 2.2: Left: A schematic description of the diffusion models described in §2.2.2.3 (red) and §2.2.2.2 (blue), c_∞ is the dissolved air content in the ambient liquid and c_{in} refers to the internal concentration profile in the gas-side. The figure also describes the evolving concentration profile within the diffusion layer of each model, highlighting their differences. Right: A schematic describing the radial pressure distribution from the cavity centre onward, during its growth, ignoring the interfacial pressure jump due to surface tension. The flat-line profile of the pressure distribution inside the cavity represents homogeneity of gas content inside.

If r^+ represents the normalized internal radial position (r/r_c), c^+ $(1-c(r)/c_\infty)$ represents the normalized internal radial concentration deficit relative to interface conditions, and, t^+ representing the normalized-time step as a Fourier number $(t\tilde{D}/r_c(t)^2)$, we require an initial and boundary condition to derive an analytical estimate of c^+. $\tilde{D}$ represents the diffusion coefficient of air in water-vapor, instead of air in water, as was the case in §2.2.2.1 and §2.2.2.2. This distinction is a consequence of the diffusion layer being inside the vortex cavity.

If at the interface $(r^+ = 1)$, the concentration remains constant and equal to c_∞, i.e., $c^+ = 0$ at $r^+ = 1 \; \forall \; t^+$, $\partial c^+/\partial r^+(r^+ = 0) = 0$ due to the axisymmetry assumption, and finally, if no gas is present inside the cavity on inception, i.e., $c^+ = 1 \; \forall \; r^+ \in [0,1)$ at $t^+ = 0$, the normalized form of the equation is similar to transient, axisymmetric, heat conduction into solid cylinders. This allows borrowing the analytical solution of c^+ [20]:

$$c^+(t^+, r^+) = \sum_{n=1}^{\infty} \left[\frac{2}{\alpha_n \mathcal{J}_1(\alpha_n)} \right] \mathcal{J}_0(\alpha_n r^+) e^{-\alpha_n^2 t^+}, \tag{2.18}$$

where, $\mathcal{J}_0$ and $\mathcal{J}_1$ are the zeroth and first order Bessel function of the first kind. α_n represents an infinite set of positively valued numbers for which $\mathcal{J}_0(\alpha_n) = 0$, or, the zero crossings of the zeroth order of $\mathcal{J}$[2]. We note here that the analytical solution is for constant cavity radius, therefore, the model described in this section is an approximation.

[2]In practice, a finite sequence of zero-crossings, α_n, suffices for calculating the concentration profiles. In this work, the first 50 zero-crossings of $\mathcal{J}_0$ were considered, which corresponds to approximately 2% error relative to the converged value of the summation term.

In order to obtain the interfacial concentration gradient, the derivative of eq. (2.18) w.r.t. r^+ can be expanded using chain-rule which finally yields the concentration gradient at the interface in non-normalized form:

$$\left(\frac{\partial c}{\partial r}\right)_{r_c} = \frac{2c_\infty}{r_c}\sum_{i=1}^{\infty} exp\left(\frac{-\alpha_n^2 t\tilde{D}}{r_c^2}\right). \tag{2.19}$$

Eq. (2.19) can be substituted into eq. (2.10) to give a growth rate formulation for the cavity size:

$$\frac{dr_c}{dt} = \frac{c_\infty}{\left[\rho_{in}^G(t) + \frac{\tau r_c}{2}\left(\frac{dp_\tau}{dr_c} + \frac{dp_c}{dr_c}\right)\right]}\left[\frac{2\tilde{D}\sum_{i=1}^{\infty} exp\left(\frac{-\alpha_n^2 t\tilde{D}}{r_c^2}\right)}{r_c}\right]_{U_D^{ma}}, \tag{2.20}$$

where, U_D^{ma} (superscript *ma* denoting mass-accumulation) scales with the diffusion velocity of the dissolved gas at the interface. One issue that arises from the model is that, as incipient cavities are much thinner than a developed cavity, the model might predict a rapid vanishing concentration gradient at the interface following inception.

Comparison Between Mass-transfer Approaches

There are two main type of differences that can be used to distinguish the aforementioned models. The first is the location and morphology of diffusion region. In terms of location, the convective-diffusion (§2.2.2.1) and thin-film diffusion model (§2.2.2.2) have their diffusion layer outside the cavity. In contrast, the diffusion layer in the transient mass-transfer model (§2.2.2.3) exists inside the cavity. In general, the diffusion coefficient of a gas in water vapor is orders of magnitudes higher than in water, therefore, a more rapid equalization of the gas concentration inside the cavity is expected. In terms of morphology, the diffusion layer of the thin film model is a thin hollow-cylinder, that of the transient mass-transfer model is a cylindrical rod, and that of the convective-diffusion model is a self-similarly evolving gas-concentration profile. Clearly, the location motivates the assumption of accumulation in the diffusion layer, while the morphology of the diffusion layer motivates the concentration gradient of dissolved gases at the cavity's interface.

The second distinguishing feature is the dependency of the diffusion-velocity, U_D, to the cavity radius, r_c. In the case of the transient mass-transfer model of §2.2.2.3, the diffusion velocity (see eq. (2.20)) is inversely a function of the square of the cavity radius, and, also rapidly shrinks with increasing time. However, in both the thin-film model and the convective-diffusion model, the diffusion velocity is approximately constant, therefore independent of the cavity radius. Noting this similarity, it is instructive to understand the conditions at which both models would provide an equivalent prediction. We do this by equating the diffusion velocities of both models, therefore term U_D^{cd} of eq. (2.11), and, the first-order approximation to U_D^{tf} from eq. (2.16). We isolate an expression for the equivalent cavity length, $\tilde{l_c}$:

$$\tilde{l_c} \approx \frac{4U_\infty \delta_f^2}{\pi D} \tag{2.21}$$

The above expression can be further simplified by inserting a Reynolds number based on the cavity length, $\tilde{l_c}$ instead of the film-thickness, δ_f, given by Re_{l_c}. In this case, we arrive at the expression:

$$\left(\frac{\tilde{l_c}}{\delta_f}\right)^2 \approx \frac{4}{\pi} Re_{l_c} Sc \tag{2.22}$$

Due to an assumption in the convective-diffusion approximation, that the Péclet number, $U_\infty \tilde{l_c}/D$, is always high, $\tilde{l_c}$ it is at least much greater than the film-thickness, δ_f, needed to match the growth rate predictions with our observations.

Vortex-Model Choices

Besides the necessity of the vortex model to estimate the pressure-gradient at the cavity interface as indicated in §2.2.1, another purpose served by the vortex model is in the estimation internal concentration of air, c_{in}, as found in the cavity growth rate expressions eq. (2.11) and eq. (2.15). (An internal concentration value is not needed for the mass-accumulator approach, eq. (2.20), because the gas-concentration profile inside the cavity is estimated by the model.) Therefore, the most simplistic assumption for c_{in} in the external diffusion layer models is that of homogeneity, with the gas-concentration derived from its partial pressure through Henry's law. The partial gas-pressure can be estimated from the pressure balance (eq. 2.4) if the ambient pressure, vapor pressure, and a vortex-model accounting for the radial pressure gradient of the cavitating flow are available.

In this work, the analytical form of the cavitating Lamb-Oseen vortex model, as derived by [8], was considered. He obtained jump-relations at the cavity interface for mass and momentum conservation equations [10] and obtained a vortex velocity profile given by eq. (2.23). In this model, the radial distribution of the circumferential velocity (u_θ) of a infinite, cavitating vortex is given as:

$$u_\theta = \frac{\Gamma_\infty}{2\pi r}\left[1 - \beta e^{\left(-\zeta \frac{r^2}{r_v^2}\right)}\right]; r \in [0, \infty] \tag{2.23}$$

Here, r_v is the viscous core radius, Γ_∞ is the circulation strength and ζ is a constant equal to 1.2526. β accounts for the zero-shear stress boundary condition at the cavity interface. Eq. (2.23) the steady Lamb-Oseen vortex model when β equals 1. An expression for β is obtained by substituting eq. (2.23) into the simplified momentum balance across the interface. This is given as:

$$\beta = \frac{r_v^2}{\zeta r_c^2 + r_v^2} e^{\zeta r_c^2 / r_v^2}. \tag{2.24}$$

For the assessment of our diffusion models against experimental data, we chose to use the vortex model of [10]. One concern in using this model is that the role of β as the cavity is developing is unknown. β typically has a small influence when $r_c/r_v \ll 1$ where its magnitude is close to 1. If β is left unbounded, it quickly grows in magnitude when the $r_c > r_v$. To circumvent this, we assume that the viscous core will increase only to constrain the cavity size. If this is satisfied, the cavity interface will always be approximately at zero-shear stress condition during the growth-stage. This can be set into the vortex model

as an *ad-hoc* correction where the β-parameter is set to a constant when $r_c = r_v$ during growth (see [9]), thus, has a maximum value of 1.55. The implication of this assumption is that when the cavity size equals the viscous core size, further mass-transfer also expands the viscous core radius size equally.

It is also reasonable to assume that without a change in both the cavitation and Reynolds number, Γ_∞ is a constant. For comparison, we also consider the condition that $\beta = 1$ which reduces eq. 2.23 to the steady Lamb-Oseen formulation. In this case, zero-shear stress across the boundary is disregarded and the cavity is assumed to be embedded within a static vortex. Finally, the pressure field around the cavity can be recovered by the simplified radial momentum balance:

$$\frac{\partial p}{\partial r} \approx \frac{\rho u_\theta^2}{r}, \tag{2.25}$$

which yields the following expression for the radial pressure distribution, as found in [9], which we state here for convenience:

$$\begin{aligned} p_c(r_c) = p(r) - p_\infty = -\frac{\rho\Gamma_\infty^2}{(2\pi r)^2}\Big\{ \frac{1}{2} - \beta exp(-\zeta r^2/r_v^2) + \\ \frac{\beta^2}{2} exp(-2\zeta r^2/r_v^2) + \frac{\beta\zeta r^2}{r_v^2}\mathcal{E}_1\Big(\frac{\zeta r^2}{r_v^2}\Big) - \frac{\beta^2\zeta r^2}{r_v^2}\mathcal{E}_1\Big(\frac{2\zeta r^2}{r_v^2}\Big)\Big\}, \end{aligned} \tag{2.26}$$

where $\mathcal{E}_1$ is the exponential integral function. In the following section, the experimental approach to measure the growth-rate of the cavity is described.

2.3 Experiments

In order to estimate the growth rate of the vortex cavity after inception and during its development, long-time shadowgraph measurements were performed at the cavitation flow loop at the Delft University of Technology. The experimental setup is described in §2.3.1, while, §2.3.2 describes the image processing and data reduction of the shadowgraph recordings for estimating the cavity size during its growth. As this water tunnel has a total water volume of only 6 cubic meters, the length of the flow loop is insufficient for dissolving all microbubbles in a single passage of the water in the flow loop. Its water quality can only be modulated by controlling the dissolved-gas content within the liquid. Therefore, two experimental procedures were used to judge the effect of the unaccounted nuclei content in the flow. This, along with our measurement approach for dissolved air concentration, is described in §2.3.3. Finally, §2.3.4 describes our measurement matrix and provides estimates of the uncertainties in the described results.

2.3.1 Measurement Setup

A schematic of the measurement setup is provided in fig. 2.3. The vortex cavity was generated by a stationary NACA 66(2)-415 elliptical half-wing with a root chord, $\mathcal{C}$, of 12.56 cm which was set at an angle of attack of 9^o to the flow with the suction side facing downwards. The freestream velocity, U_∞, was stabilized by controlling the rpm of the pump, in order to maintain a steady pressure drop across the contraction-section (as described in [42]). The ambient pressure was measured, both at the contraction inlet and exit, using a

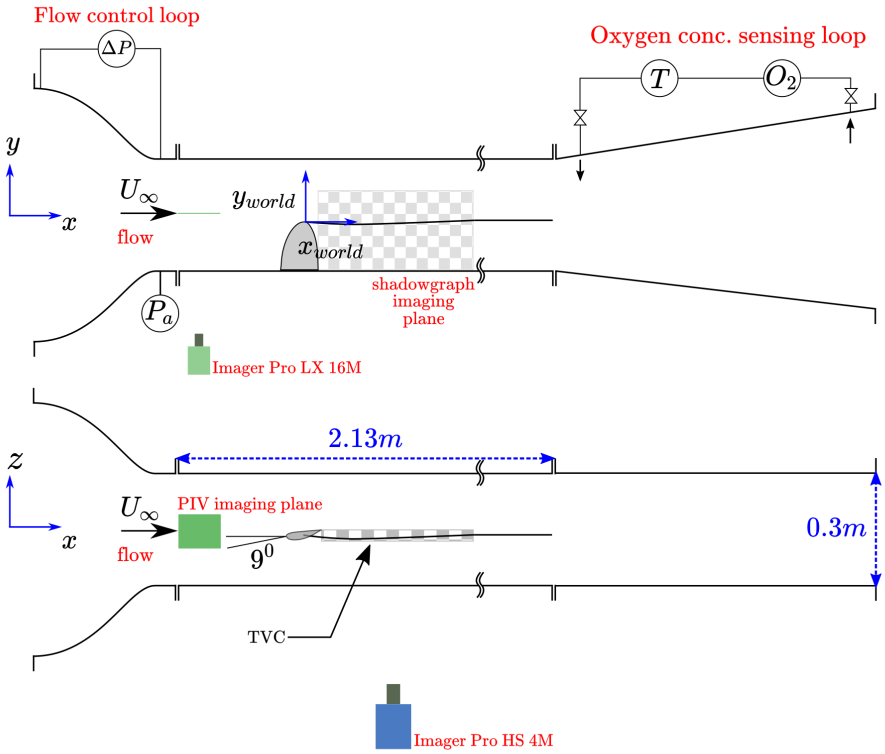

Figure 2.3: A schematic description (not to scale) of the imaging and sensor setup in the cavitation tunnel [42]. Dimension lines are marked by dashed blue lines, while flow directions are black arrows. Top: Top-view of the setup showing the absolute and differential pressure sensors, respectively P_a and ΔP, attached to the contraction. The oxygen sensor and temperature sensor, respectively O_2 and T, are shown attached to the main diffuser on the right. Bottom: The side view of the same setup, showing the position of the camera and the inclination of the elliptical foil, suction side down. In both views, the calibration plane is shown using a schematic dot-pattern with the origin and orientation of the world-coordinate system indicated. The freestream velocity calibration plane is indicated in green.

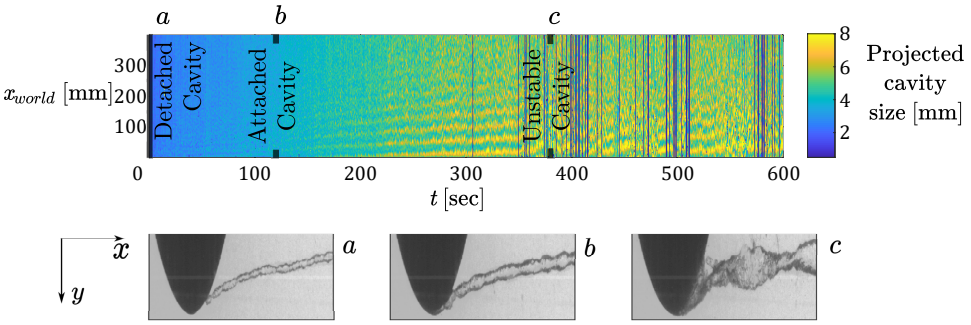

Figure 2.4: Typical space-time curve of a wing-tip vortex cavity during its growth stage (in world-coordinate system). Measurement conditions are at $c_\infty/c_{sat} = 1$. The appearance of the cavity near the wingtip during its growth from detached, to attached, to finally at unstable conditions are marked in the space-time plot and shown below. The edge detection code in these circumstances fails and can be seen in the vertical bands of discontinuity in the space-time plot above.

piezo-electric absolute pressure sensor (Keller PAA 33X) calibrated against a liquid column. This was set up as a redundant measurement to the differential pressure-sensor (Validyne DP 15) in order to validate its calibration. The linear regime of the flow-control system was ascertained using alternative planar Particle Image Velocimetry measurements of the flow entering the test section. Turbulence properties of the inflow were also inferred from the velocimetry recordings. The overall turbulence intensity was found to be below 1% of the mean velocity of 5.77 m/s.

In a typical measurement run, under-pressure conditions were first introduced to the tunnel at standstill conditions, following which, the flowrate was increased in stepwise manner until the intended cavitation number was reached, after which, the velocity was maintained. During the ramp-up of the flowrate, the cavitation initiates, and on completion of the ramp-up, the shadowgraph recordings are initiated. The shadowgraph recordings were continued while the cavity grows in size and is terminated when the cavity starts to cyclically collapse, rebound, and grow again. A typical space-time plot of the cavity size is shown in fig. 2.4, which shows that the cavity is initially featureless, i.e., the cavity size is uniform along its axis, and visibly detached from the tip. During growth, the cavity develops stationary waves on the surface, and after some development, attaches to the tip of the foil. Subsequently, the amplitude of the stationary wave increases, and the cavity becomes unstable, collapses and rebounds cyclically. This signals the termination of the cavity growth stage.

One important consequence of this experimental procedure is that the inception occurs during the ramp-up process, and that the vortex cavity has already slightly developed when the ramp-up is complete and the shadowgraph recordings commence. Therefore, the air concentration inside the cavity is expected to be non-zero from the start of the shadowgraph recordings. For this reason, we have chosen to compare our experimental data to predictions using a standardized Fourier number, which we discuss in §2.3.3. Our standardized Fourier number comparison is provided in §2.4.3.

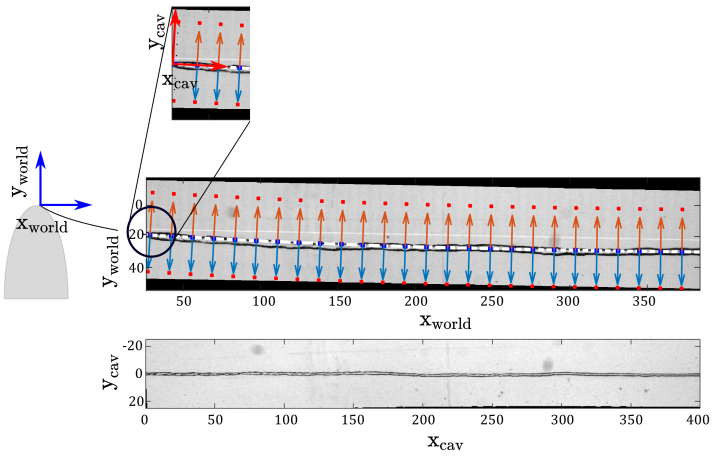

Figure 2.5: Image transformation of the shadowgraph recordings. In this figure the flow is from left to right. Top: Cavity images in world-coordinate system. Cavity axis is given by dotted white lines, arrows indicate the cavity normal direction and red squares indicate the extents of the domain used for subsequent warping step. Bottom: Cavity shadowgraph presented in straightened format in averaged cavity-centreline coordinate system. All dimensions are provided in millimeters.

2.3.2 Imaging and Image Processing

The field of view was adjusted to cover the region from the wingtip and up to a maximum distance of 4.3 root-chord lengths downstream. The camera was calibrated using a laser-engraved 2D dot-target pattern of 1 cm dot-pitch placed at the vertical mid-plane of the test section, as shown in fig. 2.3. A two-dimensional, third order polynomial mapping function similar to [46] was used for pixel-to-world coordinate transformation. This mapping function corrects for refraction through the thick acrylic wall of the test section and fits to the centroids of the imaged dots to within 0.1 pixels.

The cavity was imaged using an ImagerPro HS 4M high-speed camera mounted with a 35mm Nikon objective. The image resolution was set to 2130×300 pixels, and the frame-rate of the high-speed camera was adjusted to provide a maximum of 30 minutes of observation time. Backlighting of the cavity was provided by a LED light-panel set to pulse with the camera shutter and with a pulse-width between $50 - 80\mu s$. As the LED duty cycle is well below reported typical time-scales of cavity oscillations [2, 43] and motion blur on the cavity interface is avoided. The edges of the cavity are easier to extract using a scheme based on the gradient of the images. In this study, the Canny edge detector [14] was found to be suitable for extracting the cavity edges.

Once the cavity edges were detected, the projected centreline of the cavity was calculated from the midpoint between the upper and lower edges of the cavity. An ensemble averaged cavity centreline was then estimated from an ensemble of our recordings, which is shown in fig. 2.5 in the world coordinate system. In order to dewarp the image so that the mean cavity centreline is the abscissa of the new coordinate system, its arc-length parametrization was first calculated using the following integral approach:

$$l_{cav} = \int_p^q \sqrt{1 + \left(\frac{dy}{dx}\right)^2}\, dx, \tag{2.27}$$

where, l_{cav} is the length of the cavity in the cavity centreline coordinate system between any 2 points p and q on x_{world}, and, y is position of the mean cavity centreline as a function of x_{world}.

To simplify this operation, the estimated position of the mean cavity centreline in y_{world} was replaced by a one-dimensional, second-order polynomial as a function of x_{world} with the resulting R^2 of the polynomial fit being 0.99. The polynomial was then reparametrized by its arc-length using eq. (2.27). The resulting new coordinate system has the abscissa as the arc-length parametrized form of the mean-cavity axis (x_{cav}) and the ordinate as the direction normal to the tangent of the mean cavity axis in world coordinate system (y_{cav}). This finally helps generate a cartesian grid in the new coordinate system, which appears warped in the world coordinate system, as indicated in fig. 2.5. Finally, a two-dimensional, homogeneous polynomial is used to warp the image from world-coordinate system to the cavity axis system (see fig. 2.5). Here, the fitting error, defined as the euclidean distance between the axis system of the unstraightened cavity images and the new grid in the cavity axis centered coordinate system (as described in figure 2.5), was found to be less than 10^{-3} mm and therefore not considered in the error analysis. The final resolution of the image in cavity-axis system is 0.18 mm in cavity-axis direction and 0.125 mm in cavity-transverse direction.

In the last step of the image processing, the cavity's projected diameter was estimated from the dewarped cavity edges in the new coordinate system. The resulting cavity growth curves were averaged along the axis-direction for each time-step, following which, a running time-average filter over 500 timesteps was applied to the cavity size time-history.

2.3.3 Dissolved Gas Monitoring

In the present experiments, the ambient dissolved gas level was varied between 28% to 41% air-saturation relative to atmospheric conditions. Under the assumption that the partial fraction of gases in air remains unchanged in underpressure conditions, the dissolved oxygen content was measured as a proxy to the air content. This was monitored by an on-line, optical, dissolved oxygen probe of the flow-through type (PreSens FTM type) whose working principle is based on the fluorescence-quenching mechanism of oxygen molecules. The sensor was housed in a parallel pipe-branching connected to the points near the inlet and exit of the main-diffuser as shown in fig. 2.3. In such a configuration, the natural pressure-drop of the diffuser drives a flow inside the branching which refreshes the sampled tunnel water dynamically, giving reliable results during running conditions. The tunnel has a relatively low water volume of about 6 cubic meters, therefore, at the measurement conditions, the typical flow through time between the hydrofoil and the measurement probe is of $\mathcal{O}(1)$ seconds. In standstill conditions, the ambient pressure on the foil region is also similar to the probe location. Therefore, the sampled water can be thought to be a reliable proxy to the measured dissolved gas in the test section. A PT100 type temperature sensor, compatible with the oxygen sensor's data acquisition system, was also installed to account for temperature changes to the measured oxygen content level. In this work, the oxygen concentration is quoted as % air saturation relative to atmospheric

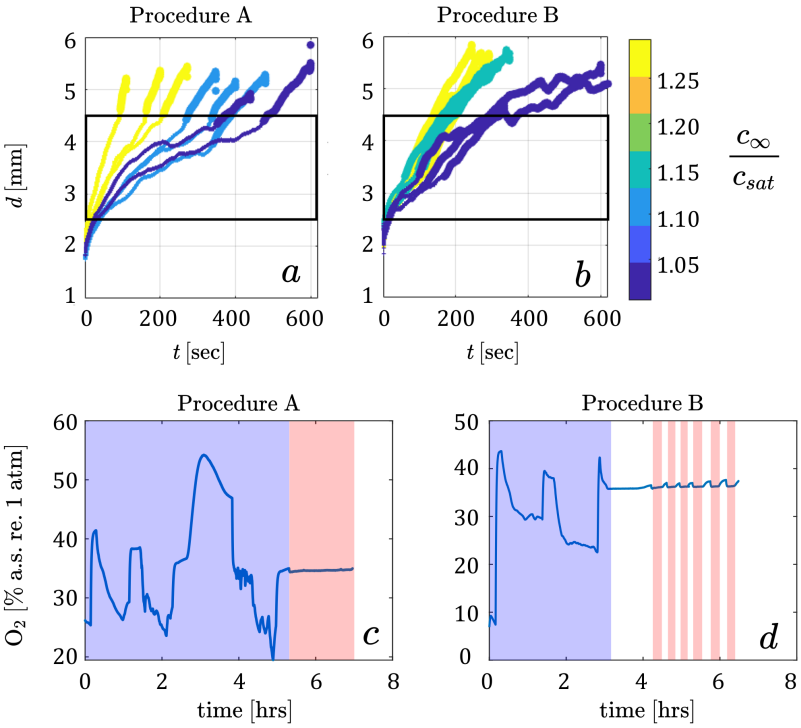

Figure 2.6: a and b: Time-history of the filtered and axially averaged cavity diameter $d := 2r_c$, over the observation period, t, for both measurement procedures described in §2.3.3 and tabulated in table 2.2. The time-histories are colored with respect to the relative saturation level, c_∞/c_{sat}, and the marker thickness is increased when the cavity appears to attach to the wing-tip. The growth period between growth ranges of 2.5 *mm* and 4.5 *mm* is highlighted by the boundaries of the black boxes superimposed on the text. c and d: Oxygen-content measured by the dissolved-oxygen probe represented as a percentage air-saturation relative to 1 atm and operating temperatures. The degassing phase is highlighted in blue whereas red highlights the time-history when the measurement run commenced, and the tunnel is running either at idling (3 *m/s*) or testing conditions. In the figure on the right, shark-fin like deviations is seen in between the measurement runs when the tunnel is stopped and vacuum is removed. In the blank regions, the tunnel is in a shut down state without underpressure or a flow.

pressure and measured temperature. Repeat observations were performed on the same day, and, three dissolved-gas levels were chosen, with each gas-level set on a different day. The dissolved-gas content was reduced every subsequent measurement day and repeat measurements were performed on the same day. The measurement procedure was also varied, in the first procedure (procedure A), the facility is not shut down between the repeat runs, while in the second procedure (procedure B), the facility is shut down between the repeat runs in order to remove microbubbles from the flow.

Because of the flow-through nature of the sensor, the dissolved air-content measurement is sensitive to the presence of a flow in the accompanying diffuser. On stopping the flow, the oxygen sensor reported increasing gas-content due to microbubbles dissolving locally near the probe, thus, de-correlating the sample population present in the sensor branch from the parent population. This is characterised by the shark-fin like deviations on the oxygen sensor recording and is shown in the right panel of fig. 2.6 (procedure B), which are not found when a flow in the tunnel is always present (left panel of fig. 2.6, procedure A). Noting that both procedures significantly differ in terms of how much nuclei content is available in the tunnel prior to a measurement, it is important to distinguish between both measurement procedures as shown in fig. 2.6 into one where tunnel's free-gas content is unaltered (procedure A) during the course of the day while the second procedure is where the tunnel's free-gas content is reset by reintroducing atmosphere and stopping the flow between runs (procedure B). The top panels of figure 2.6 also show the time-history of the measured cavity-radius.

A few observations from figure 2.6 are clear. Firstly, in both measurement procedures, an increase in the relative saturation content of air in ambient flow-conditions increases the growth rate of the cavitation. Secondly, measurement repeatability is severely affected by the increasing nuclei-number-density of bubbles when using measurement procedure A. Finally, the most puzzling aspect is that the attachment of cavity during its growth is delayed in measurements using procedure A. The cause for this observation is unclear and has not been pursued in this work. From these observations, the measurements using procedure B were chosen for further analysis. As the effect of unaccounted free-gas bubbles are presumably lesser. More importantly, the repeatability of the experiment is enhanced. Therefore, the measurements can be said to be in nuclei depleted conditions.

2.3.4 Measurement Matrix and Measurement Spread

In the present work, the chord Reynolds number (Re_C) and cavitation number (σ) are defined as:

$$Re_C = \frac{U_\infty C}{\nu} \tag{2.28}$$

$$\sigma = \frac{p_\infty - p_{vap}}{0.5\rho_l U_\infty^2} \tag{2.29}$$

The measurement matrix of the observations found in this work is provided in table 2.2. In this tabulation, we also provide the F_m estimated over a fixed growth range of the cavity diameter, i.e., from 2.5 mm to 4.5 mm. The time elapsed between these two bounds is also provided in the table. The relative saturation of air in water, c_∞/c_{sat}, is provided with c_{sat} determined at the working ambient pressure, p_∞, using Henry's law. We refer to

	Procedure [-]	p_∞ [$mbar$]	T [^oC]	Re_C [$\times 10^5$]	σ [-]	O_2 [$\%re.1atm$]	c_∞/c_{sat} [-]	Δt [sec]	$\tilde{F_m}$ [-]
				7.35				145.55	0.29
1	A	250	20.7	7.35	1.3	41.00	1.51	189.93	0.37
				7.30				83.56	0.16
				7.35				309.32	0.61
2	A	300	21.0	7.40	1.4	37.00	1.36	354.12	0.70
				7.40				233.80	0.46
3	A	300	21.3	7.45	1.4	34.50	1.27	349.10	0.69
				7.45				455.04	0.91
				7.50				183.32	0.36
4	B	275	21.6	7.50	1.2	36.30	1.33	136.62	0.27
				7.50				126.90	0.25
				7.50				182.49	0.36
5	B	275	21.5	7.50	1.2	32.40	1.19	190.40	0.38
				7.50				162.77	0.32
				7.60				275.07	0.55
6	B	275	22.0	7.60	1.2	28.15	1.04	280.05*	0.56
				7.60				358.79	0.71

Table 2.2: Measurement data for both measurement procedures including the inflow cavitation number, σ, the dissolved gas content expressed relative to saturation conditions at the set test section pressure, c_∞/c_{sat}, and estimates of $\tilde{F_m}$ numbers from experimental measurements for the time duration (Δt), extrapolated from data, for a change in cavity projected diameter from 2.5 mm to 4.5 mm, as highlighted by gray in fig. 2.6. One measurement in set 6 was terminated prematurely but has been included in the table and highlighted with an asterisk. In all the calculations the freestream velocity is taken as 5.77 m/s.

this form of standardization of F_m as $\tilde{F_m}$. It will be clear in §2.4.3 that this standardization helps enable the comparison of our experimental data with our predictions.

The estimation of the spread in the reported experimental parameters was performed using the Monte-Carlo error propagation procedure described by [18], with the input quantities assumed to be normally distributed. The error propagation begins with the voltage output of the pressure sensor, whose typical standard deviation of about 2% of the mean measured voltage, while the temperature sensor has a typical standard deviation of about 1% of the mean measured.The standard deviation of the voltage of the temperature and pressure sensor were used to estimate the histogram of the measured temperature, pressure, and freestream velocities from their respective calibration functions. The obtained distributions were then used to estimate the same for the density, dynamic viscosity and vapor pressure of water using standard temperature correlations. Finally, the probability distributions of density, dynamic viscosity and vapor pressure were used to estimate the same for the chord Reynolds number of the flow, and the cavitation number of the measurement. For the relative air-saturation concentration, the spread of the dissolved oxygen sensor was ignored as its magnitude is very small. Therefore, the spread in this quantity is largely due to that present in the ambient pressure measurement. The edge detection performed for the images is deterministic, hence, the spread in the measured cavity size is of the order of the pixel resolution in cavity centreline coordinate system, y_{cav}, therefore 0.125 mm. The spread of the smoothed cavity size time-history is based on the standard deviation of the running average performed over 500 timesteps and presented as shaded uncertainty envelopes in the figures following this section. In the following discussion, we report the measurement spread as the 95% confidence bound of the estimated probability distributions of the quantities reported.

From the Monte-Carlo error propagation approach, the estimated chord Reynolds

number, Re_C, varied between 7.3×10^5 and 7.5×10^5 with an spread of 1.25%, 4.08% spread in the cavitation number, which was achieved with an input measured inflow velocity distribution of 5.77 m/s with 1.05% uncertainty. The spread of the measured ambient pressure, therefore, that of the relative saturation level at ambient pressure conditions of the measurement, was 3.18%.

2.4 Results and Discussions

In §2.4.1 and §2.4.2, we first present and discuss the cavity radius predictions of eq. (2.11), (2.15) and (2.20) for typical experimental values of the vortex viscous core, the incipient cavity radius and the relative saturation of the ambient dissolved gas content. For convenience, we divide this discussion into two parts: In §2.4.1 we discuss the predicted growth behavior for relatively saturated and oversaturated dissolved gas conditions; and, in §2.4.2, we show the same for undersaturated conditions, where stable cavity sizes can be sought. Then, in §2.4.3 we compare the predictions of the diffusion models with experimental data using a Monte-Carlo approach.

Solving the equations of the cavity growth rate (§2.2) requires a careful consideration of the parametric entries. The parametric entries are divided into three parts. The first set concerns known thermodynamic and kinematic properties of water and the gases dissolved in it (table 2.3), which we take to be air. This contains the molecular weight of air (M_g), density of air and water (ρ_g and ρ_l, respectively), Henry's constant for air dissolved in water (K_H), the water temperature (T), the binary diffusion coefficient for air in water (D), and the surface tension coefficient of pure-water ($\mathcal{T}$). With regards to the binary diffusion coefficient, we assume a magnitude of $2\times10^{-9}\ m^2/s$ for the external diffusion models described in §2.2.2.1 and §2.2.2.2. For the internal diffusion model, we assume the diffusion coefficient, $\tilde{D}$, to be that of air in water-vapor. We assume this to be a magnitude 10^3 times higher than D, which is approximately the diffusion coefficient of oxygen in water-vapor ($2.4\times10^{-5}\ m^2/s$ at 20^oC). We also include the tunnel ambient pressure, p_∞, and the ambient dissolved gas concentration, c_∞, in this categorization.

The second set of parameters (table 2.4) are the flow dependent properties of the vortex cavitation. They consist of the incipient vortex cavity size, r_c^i, the size of the vortex viscous-core, r_v, the β parameter which varies the vortex model between the steady Lamb-Oseen vortex model ($\beta=1$), or, the *ad-hoc* correction described in §2.2.2.5. The ambient circulation strength (Γ_∞), is back-calculated from the vortex model using the assumed viscous-core size, the expression for the pressure distribution of the vortex (eq. 2.26), and, the pressure balance of eq. (2.4) at inception conditions, i.e., when p_{in}^g is zero.

The third set of parameters (table 2.5) relate to the diffusion velocities of the individual diffusion models. They are the cavity length for the convective-diffusion model, either l_c, or, $\tilde{l_c}$, and, the film-thickness, δ_f, for the thin-film diffusion model. Both these quantities are treated as tuning parameters to match the predictions with our experimental data. We note here that the diffusion velocity of the transient mass transfer model of §2.2.2.3 is dependent on the diffusion coefficient and the cavity radius alone. We also include in the table the equivalent cavity length parameter (eq. 2.21) for the convective-diffusion model (§2.2.2.1).

The growth rate equations are solved using a first-order time-stepping approach. The simulations are set to begin at inception conditions, and, in these conditions, the internal air-concentration in the cavity is assumed to be zero. Therefore, the growth of the cavity

	Symbol	Units	§2.4.1, §2.4.2	§2.4.3.1	§2.4.3.2
Molecular weight of air	M_g	kg/mol	28.96×10^{-3}		
Water temperature	T	K	295	table 2.2	295
Universal gas constant	R	$J/mol\cdot K$	8.314		
Air and water density	ρ^g, ρ_l	kg/m^3	M_g/RT, 10^3		
Henry's constant	K_H	$kg/m^3\cdot Pa$	0.223×10^{-6}		
Diffusion coefficient (air-water)	D	m^2/s	2×10^{-9}		
Diffusion coefficient (air-water vapor)	$\tilde{D}$	m^2/s	2×10^{-5}		
Ambient pressure	p_∞	Pa	30000	table 2.2	table 2.1
Ambient dissolved gas concentration	c_∞	kg/m^3	(0.1 to 2)$K_H p^*_\infty$	table 2.2	table 2.1
Vapor pressure of water	p_{vap}	Pa	Clausius-Clapeyron		
Surface tension	$\mathcal{T}$	N/m	0.071		

Table 2.3: A tabulation of the material properties used for the analyses in §2.4.1 and §2.4.3. Asterisk superscript indicates range of values.

	Symbol	Units	§2.4.1, §2.4.2	§2.4.3.1	§2.4.3.2
Incipient cavity radius	r_c^i	mm	0.5	$0.125 \le r_c^i \le 0.2$	1, 1.5
Viscous-core radius	r_v	mm	2.5	eq. (2.31)	2, 4.5**
Ambient circulation strength	Γ_∞	m^2/s	0.09*	0.04*	0.2, 0.45**

Table 2.4: A tabulation of the flow related properties used for the analyses in §2.4.1 and §2.4.3. The expression for vortex-viscous core size is based on a Winkelman-vortex model [28] fit to the stereoscopic PIV measurements found in [42]. The root-chord length of the foils considered in the analyses (C) are 12.56 cm in §2.4.3.1 and 47.5 cm in §2.4.3.2. Quantities with asterisk superscript are estimated at the first timestep. Γ_∞ for §2.4.3 is given as the average of the set of predictions. A double asterix indicates that the magnitude is corrected to match experimental data.

always begins with the cavity being saturated with water vapor at its vapor pressure, p_{vap}. After each incremental timestep in which a new cavity radius is estimated, the pressure of air and its concentration inside the cavity ($p^g_{in}(t)$ and c_{in}, respectively) are evaluated from the pressure balance of eq. (2.4) and Henry's law, respectively. In order to do so, the pressure at the cavity's interface, $p_c(r_c)$, is estimated from the vortex-model, equation (2.26). The effect of surface tension is captured in $p_{\mathcal{T}}(r_c)$, and is given by the expression $\mathcal{T}/r_c$.

2.4.1 Behavior of the Diffusion Models in Saturated and Over-saturated Dissolved Gas Conditions

Figure 2.7 describes the magnitude of the cavity diameter predicted by the diffusion models of §2.2 using the input values described in tables 2.3, 2.4 and 2.5. The first discussion concerns the condition when c_∞/c_{sat} is 1.35, where the growth of the cavity radius over time, and the increasing pressure of air inside the cavity during its growth, are plotted for all three diffusion models in the top two figures. Firstly, the transient mass-transfer model (§2.2.2.3) predicts a rapid stabilization of the cavity radius to about 650 μm from its incipient cavity radius of 500 μm in a time-duration of 0.2 seconds, which gives a Fourier number ($F_m = \Delta t\tilde{D}/\Delta r_c^2$) of 17.7 highlighting that the diffusion has sufficiently advanced in only 0.2

	Symbol	Units	§2.4.1, §2.4.2	§2.4.3.1, §2.4.3.2
Cavity length for U_D^{cd}	l_c	m	1.7	-
Equivalent cavity length for U_D^{cd}	$\tilde{l}_c$	m	0.36	0.18
Film thickness for U_D^{tf}	δ_f	μm	10	5

Table 2.5: A tabulation of the diffusion model parameters used for tuning in §2.4.1 and §2.4.3.

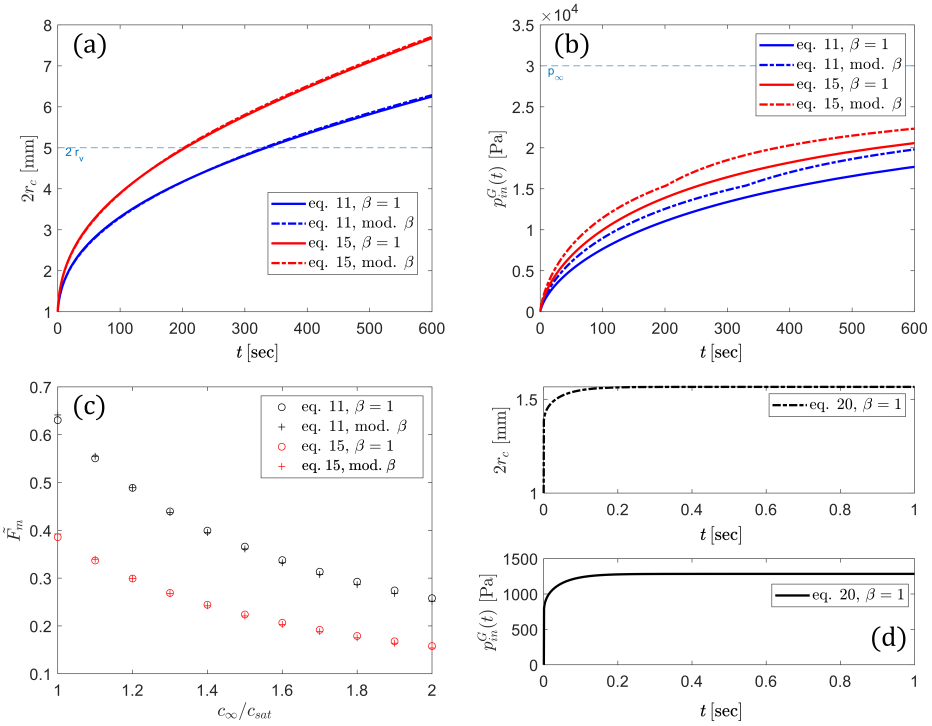

Figure 2.7: Behavior of the diffusion models (§2.2) for the parameters described in tables 2.3, 2.4 and 2.5. The vortex model chosen for the simulations are given by their respective β-parameter behavior in the legend, as described in §2.2.2.5. For figures a & b, the relative saturation level at p_∞ (c_∞/c_{sat}) is 1.35 (or 40% air-saturation re. 1 atm), while, for figure c, this is varied from 1 (saturated) to 2 (oversaturated). a: Evolution of cavity diameter over time. The transient mass-transfer model (eq. (2.20)) is indicated in a sub-figure. For convenience, $2r_v$, is indicated where the modification to the Lamb-Oseen model is activated when $\beta \neq 1$.b: The evolving pressure of gas (air) inside the cavity for the simulations of sub-figure a. c: The estimation of $\tilde{F}_m$ (defined in table 2.2) for c_∞/c_{sat} varied between 1 and 2. d: The cavity diameter evolution for the transient mass-transfer model. Top figure of d corresponds to the radius evolution over time, while the bottom figure of d corresponds to the gas pressure inside the cavity over time.

seconds. This behavior indicates that the concentration is quickly equalized when the cavity size is small and agrees with our heat-conduction analogy indicated in §2.2.2.3, where the temperature in a thin wire suddenly exposed to heat equalizes much faster than that in thicker rods. This predicted behavior is clearly not what is observed in experiments (see fig. 2.6) and invalidates the model for the purpose of predicting the cavity radius. Therefore, the transient mass-transfer model is not considered any further. The rapid equalization feature of this model, however, does help motivate the homogeneity of the gas-concentration inside the cavity, which is a central assumption in the convective-diffusion model and the thin-film model.

From the same figure, we also observe that both the convective-diffusion and the thin-film models predict reasonably similar cavity growth rates and internal gas-concentration behavior. This is expected given that these models yield identical results for a specific choice of the cavity length or the diffusion layer thickness. We also observe that the *ad-hoc* modification to the Lamb-Oseen vortex model has a marginal impact on the prediction of the cavity size. Therefore, we can conclude that the choice of the vortex model has limited advantage in the prediction of the cavity growth behavior. This can also be inferred from the standardized Fourier number ($\tilde{F}_m$) comparison in fig. 2.7.c. Overall, it is clear that the relative saturation rate c_∞/c_{sat}, and the diffusion velocity parameters have the largest influence on the growth behavior estimated by the diffusion models of eq. (2.11) and eq. (2.15). This can be inferred from the predicted $\tilde{F}_m$ behavior for the thin-film model at $t_f = 9\mu m$, which corresponds to an equivalent cavity length, $\tilde{l}_c = 0.36m$, for the convective-diffusion model (as indicated in table 2.5). For the subsequent discussion, we make use only of the convective-diffusion and the thin-film diffusion model.

2.4.2 Behavior of the Diffusion Models in Undersaturated Dissolved Gas Conditions

If stable cavity sizes are intended, the relative saturation level must necessarily be lower than 1. In this regard, it is important to understand how long the diffusion process needs to advance for stability to be achieved at a given undersaturated flow-condition. To study this, we conduct simulations with $c_\infty/c_{sat} < 1$ and estimate a new Fourier number, $F'_m = t'D/r_{in}^2$, where t' is the time elapsed following inception when the change in cavity radius is less than 10^{-3} μm.

Figure 2.8, left, provides the behavior of the convective-diffusion model and the thin-film model for a series of undersaturated dissolved gas conditions. The main observation is that stable cavity sizes are possible when $c_\infty/c_{sat} < 1$, however, the final size of the vortex cavity strongly depends on the degree of undersaturation. Furthermore, the estimated F' suggests that the diffusion needs to advance for long diffusion timescales the closer c_∞/c_{sat} is to 1. Note that in this assessment, we ignore the upper bounds to the cavity size which we have observed in our experiments (see figure 2.4).

Both the convective-diffusion model with $l_c = 1.7$ m, and the thin-film model with $t_f = 10$ μm predict the same final cavity size despite having different growth-rates. This suggest that the final stable cavity size is independent of the diffusion model choice. It is possible to estimate the stable cavity radius in undersaturated conditions in the following manner. At equilibrium, c_{in} equals c_∞. Therefore, from Henry's law, the gas pressure inside the cavity is then equal to $c_\infty p_\infty/c_{sat}$. This can be substituted to equation (2.4) which results in the

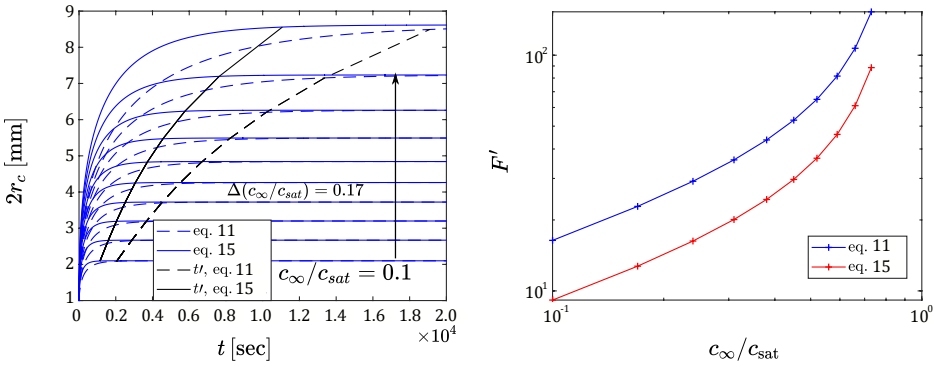

Figure 2.8: Behavior of the diffusion models in undersaturated conditions for parameters of tables 2.3, 2.4 and 2.5. Left: Cavity radius predictions by the diffusion models in undersaturated dissolved gas conditions, where c_∞/c_{sat} is varied from 0.1 onward with a step size of 0.17. The terminal time of the growth, t', is indicated by black lines. Right: Estimation of F' for the simulations conducted in the left figure for both diffusion models. For the analyses, the Lamb-Oseen vortex model is used ($\beta = 1$).

following expression for the cavity interface pressure in stable cavity size conditions:

$$p_c = p_\infty(c_\infty/c_{sat} - 1) + p_{vap} - p_\tau. \tag{2.30}$$

The above expression can be substituted into the pressure equation of a vortex model, such as that in eq. (2.26), and through a least-squares approach, the stable cavity radius required to balance both sides of the expression can be estimated. This demonstrates that an estimate of the stable cavity size is largely defined by the radial pressure profile of the vortex-cavity, which in turn depends on the vortex-model considered. As velocimetry around the vortex-cavity was outside the scope of this work, this analysis has not been considered any further.

2.4.3 Comparison With Experimental Data

In this discussion, we use the thin-film model as the base diffusion model for our analyses and represent the convective-diffusion model by its equivalent length parameter, $\tilde{l}_c$. As noted from our previous discussion in §2.4.1, the vortex model we have chosen for this analysis is the steady Lamb-Oseen vortex model.

Oversaturated Regime

As remarked earlier in §2.3.1, the incipient vortex cavity size in our observations is unknown. This is important to note because the incipient cavity size is an important vortex cavity parameter in our models (see tables 2.3, 2.4 and 2.5). Therefore, we introduced the standardized Fourier number, $\tilde{F_m}$, in §2.3.3, which compares the growth rate within a fixed cavity growth range. Further, the vortex viscous-core size is unknown in the present experiments, therefore, we take a Monte-Carlo simulation approach to estimate the prediction spread for both r_c, as well as, $\tilde{F_m}$. In this procedure, both the vortex cavity parameters, r_c^i and r_v, are varied within a reasonable range. For the viscous-core radius estimate, we refer

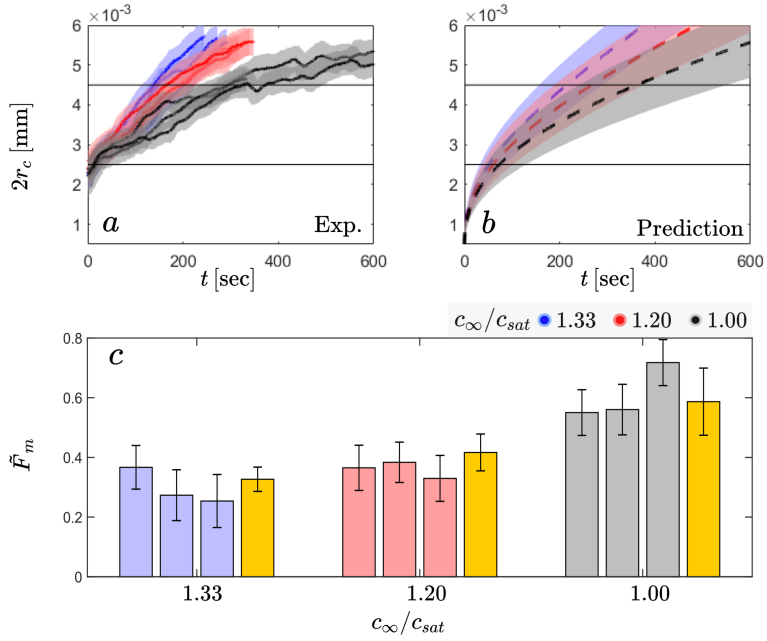

Figure 2.9: Comparison of the experimental observations in the oversaturated regime with the diffusion model predictions for chosen parametric entries (tables 2.3, 2.4 and 2.5). Top: Comparison of the growth of the vortex cavity size, $2r_c$, with the experimental data, procedure B, from table 2.2. The uncertainty envelopes correspond to two standard deviation bounds. Horizontal lines correspond to the size range used to evaluate the standardized Fourier number, $\tilde{F_m}$. Bottom: Bar chart comparing Experimental $\tilde{F_m}$ values obtained from repeated measurements, color coded according to their respective c_∞/c_{sat} values, while yellow bars are their corresponding predictions. The error bars here represent the one standard deviation bound of the output probability distribution of $\tilde{F_m}$.

to the work of [44] where a Winckelman vortex model fit to their experimental data is given by the following expression:

$$r_v = \mathcal{B} \cdot 0.37 \mathcal{C} Re_C^{-0.2} / 10^3, \tag{2.31}$$

where $\mathcal{B}$ varies between 0.3 and 0.5, depending on the distance from the tip. For the incipient cavity radius, we choose a range between 125 μm and 200 μm, which is in range of the typical nuclei radius expected in the tunnel.

Figure 2.9 details the comparison of our experimental data with the diffusion model predictions. In the comparison, the resulting probability distributions of $\tilde{F_m}$ predictions were found to be non-normal, therefore, the predicted $\tilde{F_m}$ is expressed as a mean value and the error bars are defined by one standard deviation of the distribution. From the figure, we find that the diffusion models offer a reasonable prediction of the cavity growth rate for an assumed film-thickness, δ_f, of 5 μm, or, an equivalent cavity length, $\tilde{l_c}$, of 0.18

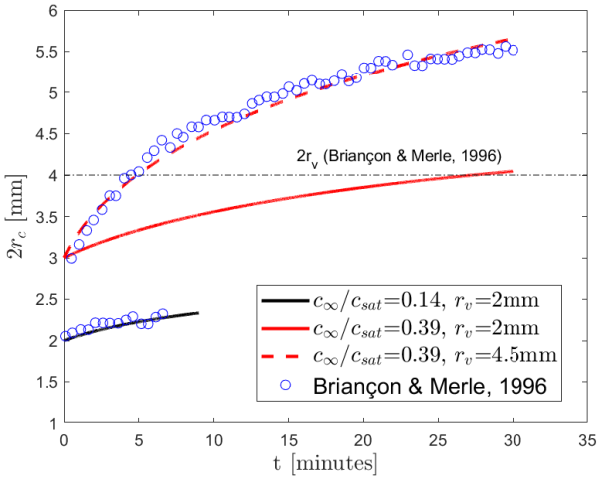

Figure 2.10: Comparison of the experimental observations of [13] in the undersaturated regime with diffusion model predictions for chosen parametric entries (tables 2.3, 2.4 and 2.5).

m. It is concluded that the growth-behavior of a cavitating vortex is largely driven by molecular diffusion in nuclei depleted conditions. However, this comparison does not distinguish between the thin-film model and the convective-diffusion model, leaving the detailed mechanism of vortex-cavitation growth speculative. With the convective-diffusion approach, it is clear that the length of the cavity needed for the comparison is not what is observed in experiments where the cavity length is observably at least as long as the length of the test-section following the hydrofoil tip. For applying this model to experimental data, an estimate of the possible equivalent cavity length remains unknown. What is striking is that, the estimated magnitude of $\tilde{l}_c$, 0.18 m, is quite close to the root-chord length of the wing-tip used. The scope of our analyses presented here do not suffice to explain this occurrence, therefore, this observation remains coincidental. Similarly for the thin-film diffusion model, while a film thickness of 5 μm suffices to explain the observed growth rate, and, even though the criteria that $r_c \gg \delta_f$ is satisfied, the physical mechanisms that eventually lead to the formation of this thin-layer is unknown. Therefore, the choice between these two modeling approaches remains open.

Undersaturated Regime

Comparison against experimental data for the undersaturated regime was made possible from the cavity diameter time-histories reported by [13][3]. The experimental conditions concerned here are the *small-nuclei* cases considered for c_∞/c_{sat}, p_∞, U_∞ and σ found in rows 1 and 2 of table 2.1, whose relevant properties have been summarized in tables 2.3, 2.4 and 2.5. For the model predictions, we have assumed that the cavity size data provided at the first timestep corresponded to inception conditions. The comparison against experimental data is provided in fig. 2.10. For the case where the relative undersaturation is 0.14, a reasonable comparison between both the predicted and observed cavity diameter time-histories was observed. The performance of the diffusion model could not be replicated

[3]These conditions were not possible in the facility used for the present study because the tunnel's ambient pressure could not be increased beyond 1 atm to lower c_∞/c_{sat} below below 1.

for relative undersaturation of 0.39 using the experimental conditions as provided in [13]. In order to match the data, a modification to the viscous core radius to 4.5 *mm* had to be made. As stated previously, the chosen vortex model (here, the static Lamb-Oseen model) also plays a role in the prediction of the time-history, therefore, an exact match of the predictions in the temporal space is difficult.

While a quantitative comparison using the above results is difficult, the predictions qualitatively agree with the experimental data, thus supporting the discussion in §2.4.2. This means that in the undersaturated regime, the size of the stable cavity is proportional to the degree of undersaturation.

2.5 Conclusions

In nuclei depleted conditions, the mechanism of vortex cavity growth following inception can be described as a diffusion dominant phenomenon. Gases dissolved in the liquid enter the vortex cavity through a diffusion layer whose morphology is either hollow-cylinder like (thin-film model), or, developing boundary layer like (convective-diffusion model). From the assumptions common to both the thin-film and the convective-diffusion model, the concentration of air inside the cavity can be thought to be homogeneous. It was found that the convective-diffusion model predicts the growth rate of the cavity reasonably well but requires a cavity length parameter that does not correspond to the physical length of the observed cavitation. In contrast, the thickness of the diffusion layer in the thin film does satisfy the condition $\delta_f \ll r_c$, making it a more appealing description of the diffusion phenomenon. However, physical motivations of the thickness of this diffusion layer remain unknown. Furthermore, in oversaturated conditions we found that the details of the vortex model used in the pressure balance across the interface did not significantly change its growth behavior.

In saturated and oversaturated dissolved gas conditions, $c_\infty/c_{sat} \geq 1$, the diffusion process does not terminate. Consequently, the cavity grows uncontrollably until it becomes unstable, and its size seems to oscillate. The conditions for the upper bounds on the cavity size is not presently known. In undersaturated dissolved gas conditions, $c_\infty/c_{sat} < 1$, the details of the diffusion model were found to not affect the final stable size of the vortex cavity. Rather, we find that the vortex cavity size in undersaturated dissolved gas conditions depends on the pressure profile around the vortex cavity, and the degree of undersaturation. Further understanding of the role of the vortex velocity profile in the rate of growth of vortex cavities is necessary.

The growth behavior of the vortex cavity was found to be fairly repeatable in nuclei depleted conditions, and strongly affected by nuclei in weak-water conditions, although, the influence of the relative saturation of dissolved gases could still be discerned from the non-repeatable measurements. In cavitation tunnels that do not have provisions for water quality control, it is possible to obtain repeat experiments by shutting down the cavitation tunnel and introducing the tunnel to atmospheric pressure between runs. This provides the residence time for the gas bubbles to either separate due to their buoyancy, or reabsorb back into the solution. If stable cavity sizes are intended, the degree of undersaturation must be high so as to reduce the diffusion time-scales ($F' = 1$) required before the cavity size stabilizes.

Bibliography

[1] Amini, A., Reclari, M., Sano, T., Iino, M., Dreyer, M., and Farhat, M. (2019). On the physical mechanism of tip vortex cavitation hysteresis. *Exp. Fluids*, 60(7):118.

[2] Arndt, R., Arakeri, V., and Higuchi, H. (1991). Some observations of tip-vortex cavitation. *J. Fluid Mech.*, 229:269–289.

[3] Arndt, R. and Keller, A. P. (1992). Water quality effects on cavitation inception in a trailing vortex. *J. Fluids Eng.*, 114(3):430–438.

[4] Arndt, R. and Maines, B. (2000). Nucleation and bubble dynamics in vortical flows. *J. Fluids Eng.*, 122(3):488–493.

[5] Arndt, R. E. (2002). Cavitation in vortical flows. *Ann. Rev. Fluid Mech.*, 34(1):143–175.

[6] Atlar, M. (2002). The specialist committee on water quality and cavitation–final report. *Proc. 23rd ITTC*, 2.

[7] Billet, M. and Weir, D. (1975). The effect of gas diffusion on the flow coefficient for a ventilated cavity. *J. Fluids Eng.*, 97(4):501–505.

[8] Bosschers, J. (2018a). An analytical and semi-empirical model for the viscous flow around a vortex cavity. *Intl. J. Multiphase Flow*, 105:122–133.

[9] Bosschers, J. (2018b). *Propeller tip-vortex cavitation and its broadband noise*. PhD thesis, University of Twente.

[10] Bosschers, J., Janssen, A., and Hoeijmakers, H. (2008). Similarity solutions for viscous cavitating vortex cores. *J. Hydrodynamics, Ser. B*, 20(6):679–688.

[11] Brennen, C. (1969). The dynamic balances of dissolved air and heat in natural cavity flows. *J. Fluid Mech.*, 37(1):115–127.

[12] Brennen, C. (2014). *Cavitation and bubble dynamics*. Cambridge University Press, Cambridge, UK.

[13] Briançon-Marjollet, L. and Merle, L. (1996). Inception, development and noise of a tip vortex cavitation. In *21st Symp. on Naval Hydrodynamics, Trondheim, Norway*.

[14] Canny, J. (1986). A computational approach to edge detection. *IEEE Transactions on Pattern Analysis and Machine Intelligence*, (6):679–698.

[15] Chen, L., Zhang, L., Peng, X., and Shao, X. (2019). Influence of water quality on the tip vortex cavitation inception. *Phys. Fluids*, 31(2):023303.

[16] Cheng, H., Long, X., Ji, B., Peng, X., and Farhat, M. (2020). A new euler-lagrangian cavitation model for tip-vortex cavitation with the effect of non-condensable gas. *Intl. J. Multiphase Flow*, 134:103441.

[17] Cheng, H. Y., Ji, B., Long, X. P., Huai, W. X., and Farhat, M. (2021). A review of cavitation in tip-leakage flow and its control. *J. Hydrodynamics*, pages 1–17.

[18] Coleman, H. W. and Steele, W. G. (2018). *Experimentation, validation, and uncertainty analysis for engineers.* John Wiley & Sons.

[19] Crank, J. (1979). *The mathematics of diffusion.* Oxford University Press, Oxford, UK.

[20] Cussler, E. (2009). *Diffusion: Mass Transfer in Fluid Systems.* Cambridge university press, Cambridge, UK.

[21] Dreyer, M., Decaix, J., Münch-Alligné, C., and Farhat, M. (2014). Mind the gap: a new insight into the tip leakage vortex using stereo-piv. *Exp. Fluids*, 55(11):1–13.

[22] Duarte, C., Chapuis, L., Collin, S., Costa, D., Devassy, R., Eguiluz, V., Erbe, C., Gordon, T., Halpern, B., Harding, H., et al. (2021). The soundscape of the anthropocene ocean. *Sci.*, 371(6529).

[23] Duncan, P. and Needham, D. (2004). Test of the epstein- plesset model for gas microparticle dissolution in aqueous media: effect of surface tension and gas undersaturation in solution. *Langmuir*, 20(7):2567–2578.

[24] Eller, A. and Flynn, H. (1965). Rectified diffusion during nonlinear pulsations of cavitation bubbles. *J. Acoust. Soc. Am.*, 37(3):493–503.

[25] Epstein, P. and Plesset, M. (1950). On the stability of gas bubbles in liquid-gas solutions. *J. Chem. Phys.*, 18(11):1505–1509.

[26] Fyrillas, M. and Szeri, A. (1994). Dissolution or growth of soluble spherical oscillating bubbles. *J. Fluid Mech.*, 277:381–407.

[27] Gadd, G. and Grant, S. (1965). Some experiments on cavities behind disks. *J. Fluid Mech.*, 23(4):645–656.

[28] Gerz, T., Holzäpfel, F., Bryant, W., Köpp, F., Frech, M., Tafferner, A., and Winckelmans, G. (2005). Research towards a wake-vortex advisory system for optimal aircraft spacing. *Comptes Rendus Physique*, 6(4-5):501–523.

[29] Groß, T. and Pelz, P. (2017). Diffusion-driven nucleation from surface nuclei in hydrodynamic cavitation. *J. Fluid Mech.*, 830:138–164.

[30] Higuchi, H., Arndt, R., and Rogers, M. (1989). Characteristics of tip vortex cavitation noise. *J. Fluids Eng.*, 111(4):495–501.

[31] Holl, J. (1960). An effect of air content on the occurrence of cavitation. *J. Fluids Eng.*, 82(4):941–945.

[32] Holl, J., Arndt, R., and Billet, M. (1972). Limited cavitation and the related scale effects problem. In *Second Symp. Intl. Jap. Soc. Mech. Eng.*

[33] Holl, J. and Treaster, A. (1966). Cavitation hysteresis. *J. Basic Eng.*, 88(1):199–211.

[34] Jones, N. (2019). Ocean uproar: saving marine life from a barrage of noise. *Nature*, 568:158–161.

[35] Kermeen, R. and McGraw, J. (1952). *Some observations of cavitation on hemispherical head models*. California Institute of Technology, California, USA.

[36] Khoo, M., Venning, J., Pearce, B., and Brandner, P. (2020). Statistical aspects of tip vortex cavitation inception and desinence in a nuclei deplete flow. *Exp. Fluids*, 61:1–13.

[37] Lecoffre, Y., Chantrel, P., and Teiller, J. (1988). Le grand tunnel hydrodynamique (gth). *La Houille Blanche*, (7-8):585–592.

[38] Lee, I., Mäkiharju, S., Ganesh, H., and Ceccio, S. (2016). Scaling of gas diffusion into limited partial cavities. *J. Fluids Eng.*, 138(5).

[39] McCormick Jr, B. (1962). On cavitation produced by a vortex trailing from a lifting surface. *J. Basic Eng.*, 84(3):369–378.

[40] Oweis, G., Van der Hout, I., Iyer, C., Tryggvason, G., and Ceccio, S. (2005). Capture and inception of bubbles near line vortices. *Phys. Fluids*, 17(2):022105.

[41] Parkin, B. and Ravindra, K. (1991). Convective gaseous diffusion in steady axisymetric cavity flows. *J. Fluids Eng.*, 113(2):285–289.

[42] Pennings, P. (2016). *Dynamics of vortex cavitation*. PhD thesis, Delft University of Technology.

[43] Pennings, P., Bosschers, J., and Van Terwisga, T. (2014). Dynamics of isolated tip vortex cavitation. In *APS Meeting Abstracts*.

[44] Pennings, P., Bosschers, J., Westerweel, J., and Van Terwisga, T. (2015). Dynamics of isolated vortex cavitation. *J. Fluid Mech.*, 778:288–313.

[45] Schnerr, G. and Sauer, J. (2001). Physical and numerical modeling of unsteady cavitation dynamics. In *Fourth Intl. Conf. multiphase flow*. ICMF New Orleans.

[46] Soloff, S. M., Adrian, R. J., and Liu, Z.-C. (1997). Distortion compensation for generalized stereoscopic particle image velocimetry. *Meas. Sci. Tech.*, 8(12):1441.

[47] van Wijngaarden, E., Bosschers, J., and Kuiper, G. (2005). Aspects of the cavitating propeller tip vortex as a source of inboard noise and vibration. In *ASME 2005 Fluids Eng. Division Summer Meeting*, pages 539–544. American Society of Mechanical Engineers Digital Collection.

[48] Van Wijngaarden, L. (1967). On the growth of small cavitation bubbles by convective diffusion. *Intl. J. Heat and Mass Transfer*, 10(2):127–134.

[49] Yu, P. and Ceccio, S. (1997). Diffusion induced bubble populations downstream of a partial cavity. *J. Fluids Eng.*, 119(4):782–787.

[50] Zhang, L. X., Chen, L. Y., Peng, X. X., and Shao, X. M. (2017). The effect of water quality on tip vortex cavitation inception. *J. Hydrodynamics, Ser. B*, 29(6):954–961.

3

Simultaneous 3D Measurements of the Kinematics and Dynamics of a Vortex Cavity[1]

Multiphase flows such as the flow around a cavitating wing-tip vortex are notoriously difficult to measure using optical techniques due to imaging and reconstruction difficulties introduced by the opacity of the cavity. The cavity itself is a dynamic, reflective gas-liquid interface that wanders around the measurement domain making velocimetry near the cavity interface difficult for correlation based approaches such as Particle Image Velocimetry. In this work we perform flow measurements around the vortex cavity generated by a NACA 66(2)-415 elliptical hydrofoil at 9 degrees incidence to the flow, at a chord Reynolds number of about 7×10^5*. The measured cavity sizes were in the range of 0.6 to 4.2 mm average cavity diameter and the cavitation numbers were in the range of 1.6 to 1.8 at a distance of 5 chord lengths downstream of the wing tip. Three-dimensional velocimetry measurements around the cavity were performed using an in-house particle tracking approach, where the reconstructions were performed using a focality agnostic particle tracking approach which considers particles image detections as ellipses, and reconstructs particles as ellipsoids in the object space which have a camera cover of three to five views. The tracking of particles across time is enhanced by the detection of the visual hull of the cavity, which is done using a combination of a convolutional neural network and a voxel carving approach. The time averaged velocity fields are compared against the Tomographic PIV approach, showing an improvement in the measurement cover around the cavity. The measurement data is extensively assessed yielding a 1.4% peak displacement error for measured particle displacements in the axial direction, and 7% in the direction transverse to the vortex axis.*

[1]This chapter is being considered for publication as Nanda, S., Muller K., Westerweel, J., van Terwisga, T., & Elsinga, G. (2023). The Kinematics of Developing Wing-Tip Vortex Cavities using Simultaneous 3D Velocimetry and Shape Reconstruction, International Journal of Multiphase Flows.

3.1 Introduction

Optical flow field imaging approaches have been very successful in single-phase flow measurements, however, measuring the velocity field around multiphase flows remains challenging. The flow field generally consists of opaque, reflective, gas-liquid structures which set limitations on the abilities of current optical measurement strategies, particularly those that branch off from PIV/PTV [2]. Therefore, many alternatives to standardized single-phase flow field imaging have been proposed [50], consisting of a wide range of non-intrusive measurements, both optical and non optical. Generally speaking, optical approaches perform imaging within the visible spectrum and the required measurement equipment can be accommodated within that used in single-phase flow field. Non optical approaches utilize the remaining part of the electromagnetic spectrum, sometimes even ultrasonic waves, in order to obtain a measurement. For optical approaches, one could (a) tag one phase with fluorescent tracers [17, 37, 52, 54], or (b) dose one of the phases of a two-phased flow with salts to match their respective refractive indices [11, 61, 63], or (c) try to resolve the visual-hull of the opaque medium using tomography [1], or (d) use other more complicated measurement approaches such as ballistic imaging [38], optical coherence tomography [22], and structured laser illumination planar imaging [6]. Among non-optical approaches, measurement techniques typically use (e) X-ray imaging to characterize the structure of the opaque phase [28, 29, 34], or approaches like (f) magnetic resonance imaging [25, 40], and (g) ultrasound imaging to resolve the velocity of the liquid phase [39, 51]. In contrast to PIV/PTV, non optical approaches are fairly new in multiphase flow imaging and developing them further is highly encouraged.

Choosing between the various measurement approaches highlighted is guided by the intended quantities one is interested in measuring, and each aforementioned technique carries its own inherent limitations [50]. In the field of cavitation research [24], which is the theme of the present work, the interests are wide and include: the velocity field inside the the vapor-liquid structure [40], the shape and motion of the vapor-liquid boundary [9, 47], velocity fields adjacent to, or outside the vapor-liquid boundary [23, 48], and the distribution, or void fraction, of the two-phase flow (including microbubble population density measurements) [36]. Particularly in the case of vortex cavitation, which is considered in this work, we are interested in studying the dynamics of the vapor-liquid boundary due to its relation to farfield noise radiated into the underwater environment. This requires simultaneous measurements of (a) the motion of its vapor-liquid interface, and (b) the velocity field adjacent to, and surrounding the vortex cavity interface (in its reference frame). While this can be easily achieved in a planar setting, as performed by [19], obtaining three dimensional measurements is advantageous from many perspectives, as will be also described in subsequent discussions.

Vortex cavitation occurs due to the inception and development of vapor structures in the low pressure region of vortex cores. Occurring most frequently in marine propellers, they appear as persistent, helecoidal shaped vapor-liquid interfaces. They originate from a low pressure zone in the tip-region of propeller blades [32, 33], and their interface dynamics have been observed to radiate a low-frequency, tonal noise [4, 48] occurring due to characteristic vibration modes on the cavity surface [7]. These vibration modes are not only responsible for increased fatigue loads on the hull structure of a ship [8], the generated noise occupies, alongside many other anthropological sources of noise, a wide

and disruptive bandwidth in the global marine acoustic spectrum [20, 31]. This strongly motivates an increase in vortex cavitation research today.

Tools to assess vortex cavitation noise include analytical dispersion models of the vapor-liquid interface, such as that described in [8], which typically requires an estimate of the axial and azimuthal interface velocity of the cavity, thus warranting velocimetry measurements. The resulting predictions using the dispersion model are compared against observations of cavity dynamics [47] in order to assess its accuracy. This interface velocity is typically provided by vortex-models that have been derived by comparison against experimental data, where one typically observes vortex kinematics and cavity dynamics separately; vortex kinematics is usually studied using velocimetry, either by using LDV [3, 10], or by stereoscopic PIV [45, 49], and the cavity dynamics is typically studied by using single camera shadowgraph imaging [48]. Separating the measurements is preferable from accuracy considerations as each technique can be individually tuned to their best possible extent, however, cavitation phenomenon is generally sensitive to facility dependant effects that alter its appearance [5] and affect the repeatability of the observation. This occurs due to the presence of dissolved gases, gas bubbles and solid particulates, together characterized under the term water quality, affecting both the inception of vortex cavities [3, 32], as well as the rate of its development [10]. Similar to the work by [10], we have also recently shown [44] (see §2) that cavity sizes are strongly affected by dissolved gases present in the liquid, therefore one may introduce water quality dependent bias errors if vortex kinematics and cavity dynamics are studied separately. Furthermore, analysing the measured velocity field is done in the reference frame of the vortex axis, and various conditional averaging approaches have been applied in current literature [19, 26, 48]. These approaches either estimate the centre of the reference axis (the cavity's own axis) as the centreline of its projected edges, or may use the measured velocity fields to estimate a symmetry center. While simple in implementation, the estimation procedures have not been reliably extended to three-dimensional measurements yet. Therefore, there are strong motivations to combine measuring the shape of a vortex cavity as well as flow measurements around it. In the subsequent discussion, we motivate why three-dimensional particle tracking measurements is advantageous over two dimensional flow measurement approaches like PIV for the case of vortex cavitation.

Cavitating vortices in general have a high angular velocity near the interface, and, correlation based techniques using rectilinear interrogation boxes may not capture the particle displacement accurately. This is largely due to a few reasons: (1) The spatial averaging that occurs when a correlation window is used to estimate flow field displacements, (2) the fact that these correlation windows may overlap with the interface of the cavity partially, which biases the measured displacement's true location, and (3), because they approximate the local velocimetry vector as a linear displacement between two timesteps. In PTV, the spatial filtering is then limited by the particle size. In that case, long tracks (here greater than 4 timesteps long) capture the displacement field next to the interface more reliably when using a temporal filter. There are, however, two main drawbacks of the PTV approach when applied to a cavitating vortex. The first is the inherent difficulty of obtaining tracking data close to the interface, due to imaging and illumination difficulties explained below. The second issue is that the statistical noise of displacement measurements using a single particle is generally higher than with correlation based velocimetry, where an ensemble

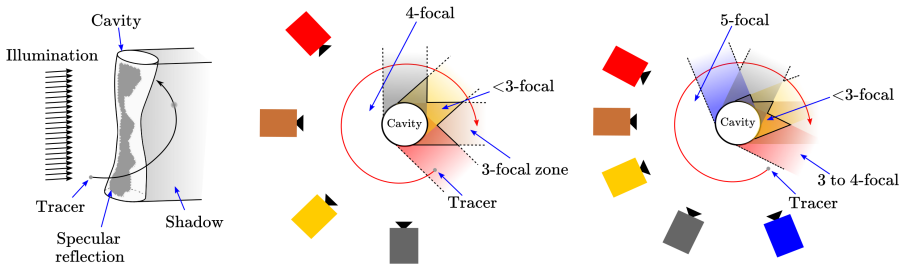

Figure 3.1: Schematic highlighting common issues with illuminating and imaging tracers around a vortex cavity. The left figure highlights the issues encountered in illuminating the volume around a vortex cavity, whereas the remaining figures describe how the focality of multiple-view camera systems breaks down in regions around the cavity.

of particles are considered per displacement measurement. In our work, we accept these drawbacks, and quantify the measurement uncertainties originating from them.

Three-dimensional reconstructions of vortex cavitation flows using conventional measurement techniques have several challenges, some of which are highlighted in figure 3.1. The first issue is that of specular reflections from the vapor-liquid interfaces which both reduce the effective observable volume and overpower the intensity of the light scattered by tracer particles. Secondly, cavities are opaque, and cast shadows in the volumetric illumination where tracers cannot be imaged. Thirdly and most importantly, the cavitation blocks optical access to tracer particles in a multi camera setup, leading to zones of variable camera cover, or *focality*, over a tracer particle. Familiar multiplicative, three dimensional reconstruction techniques such as MART [21] and its variants require full camera cover over a particle in the measurement volume in order for it to be reconstructed, therefore, suffer in performance when generally applied to multiphase flows [1].

In this present work, we have attempted the simultaneous cavity reconstruction and three-dimensional tracking of tracer particles around the cavity interface. The imaging and illumination is a combination of laser illumination and shadowgraphy, where the laser illumination is arranged to minimize imaging artefacts that occur due to specular reflections and shadows cast by the cavity. We segment the shadowgraph using a convolutional neural network and reconstruct the cavity's visual hull as described in §3.4.1. We have also developed a focality agnostic particle tracking approach that considers minimum particle camera cover of 3 and up to 5, described in §3.3.2. Our tracking approach utilizes the properties of the reconstructed cavity's visual hull in order to enable the tracking of particles around the cavity under large inter-frame displacements, of at least twice larger than the inter-particle separation in the image space. In this chapter, we describe our measurement and reconstruction procedure and assess the errors in our reconstructions.

This chapter is divided as follows: §3.2 details our imaging setup and calibration procedure, §3.3 details our reconstruction procedure, a discussion of the results is provided in §3.4, we quantify the errors of our measurements in §3.5, and finally §3.6 concludes this work.

3.2 Experimental Setup

In contrast to the helecoidal vortex cavity we considered for motivating this work (see §4.1), multiple view imaging of a line vortex cavity is simpler because the cavitating vortex neither wraps around in the measurement volume, nor shifts position substantially due to the pitch of the rotating propeller. In the present work, the vortex cavity is generated by a stationary wing-tip of a hydrofoil at incidence to the flow. In this discussion, we first describe our flow conditions in §3.2.1, following which we describe our imaging and illumination configuration in §3.2.2. We end this section by describing our camera calibration procedure in §3.2.3.

3.2.1 Flow conditions

Cases	1	2	3
N_I	9000	9000	9000
N_R/N_I	5.88	5.55	5.55
N_{IN}/N_I	0.36	0.38	0.37
r_{2D} (px)	4.62	4.62	4.62
$\bar{r}_c$ (mm)	0.34	1.94	2.10
U_∞ (m/s)	4.9	5.1	5.1
p_∞ (kPa)	24.5	23.7	23.7
Re_c (10^6)	6.72	7.07	7.07
σ	1.79	1.59	1.59
c_∞/c_{sat}	1.45	1.5	1.5

Table 3.1: Tabulation of the reconstruction test-cases discussed in this work. N_I is the total number of bright particles selected per frame, N_R is the total number of particles reconstructed per frame and N_{IN} are the inlier particles selected from the data. $r_{2D} = 0.5ppp^{-1/2}$ is an estimate of the inter-particle separation in the image using N_I for the ppp-estimation, U_∞ is the inflow axial velocity magnitude, Re_C ($U_\infty C/\nu$) is the chord Reynolds number for a root chord length (C) of 12.56 cm and kinematic viscosity ν, σ is the cavitation number given by $(p_\infty - p_{vap})/(0.5\rho U_\infty^2)$ for p_{vap} being the vapor pressure of water and ρ being its density, c_∞ is the measured dissolved gas saturation at atmospheric pressure and c_{sat} is the saturated dissolved gas concentration at p_∞ using a Henry's constant of 0.223×10^{-6} kg/m^3Pa.

The experimental particulars for the test-cases shown in this work have been described in table 3.1. Measurements were performed for three cavity sizes at similar inflow cavitation numbers, σ of 1.6 to 1.8, and Reynolds numbers, Re of 6.72×10^5 to 7.07×10^5, which were achieved by monitoring the development of the vortex cavity following inception (see §2 for discussion mechanisms of vortex cavity development), and physically initiating measurements at the desired size. For the thinnest cavity diameter, both Re and σ was marginally changed to achieve the cavity size. U_∞ was obtained from the velocimetry data from a measurement region starting 5 chord lengths downstream of the tip, by performing a time average over all reconstructed frames, whereas p_∞ was obtained from an absolute pressure sensor probe attached to the test section wall and located next to the measurement volume. The respective mean cavity sizes of the cavity have been provided as r_c in table 3.1. The dissolved gas content was measured to be 50% oversaturated with air relative to its saturation value at the measured ambient pressure in the tunnel and the temperature of the water (see c_∞/c_{sat} values in table 3.1). In these conditions, an abundance of free-gas nuclei was present in the flow.

3.2.2 Imaging and Illumination Configuration

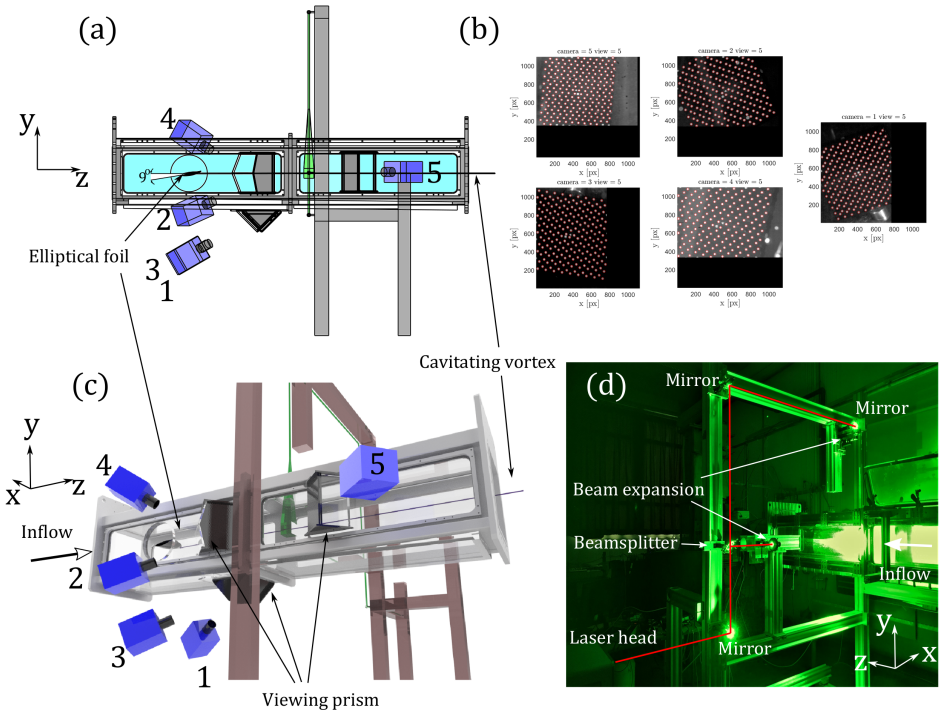

Figure 3.2: Schematic of the measurement setup. (a) and(c) are two views of the camera setup and indicates the position and arrangement of the elliptical foil and the location of the measurement volume downstream, (b) is the calibration images taken by the five views at the mid-plane slice of the measurement volume, with units in pixels, and (d) shows the laser beam illumination arrangement. The coordinate system used in this present work is indicated in the figures.

Figure 3.2 describes the measurement setup considered in this work, highlighting camera positions, illumination, and calibration considerations. The experiments were conducted in the cavitation tunnel of Delft University of Technology (described in [46]) whose test-section dimensions are $0.3\text{m} \times 0.3\text{m} \times 2.13\text{m}$. The test section was fitted on all lateral sides by 4 cm thick acrylic windows, and the foil used for generating the tip-vortex was attached through a port located 60 cm from the inlet. This foil was an elliptical half-wing with NACA 66(2)-415, of 12.56 cm root chord, here C, and a half span of 15 cm. The foil was arranged suction side down and aligned at an angle of 9 degrees to the centreline of the test-section.

The tip-vortex cavity was generated by reducing the ambient pressure in the tunnel using a vacuum pump and subsequently increasing the flow velocity until desired cavitation conditions are attained. The resulting vortex cavity was a line vortex cavity that extended to the full length of the test section. The tunnel was degassed to bring the relative gas concentration down to reasonable levels for the measurements, but, as mentioned in §3.2.1,

the amount of gas content was found to be 50% oversaturated relative to the ambient pressure saturation levels of the testing conditions. The imaged region was located 5 chord lengths downstream from the wing-tip, where the viscous roll up of the wing wake into the vortex has completed [48]. This consideration accommodated the imaging and illumination system and simplified the particle tracking process as the wake of the hydrofoil was completely removed this far downstream from the tip in the viscous roll up region (approximately within the first chord length from the tip). The flow was seeded with tracer particles of size 50 ± 10 μm, chosen to provide sufficient scattered intensity of the laser illumination. The laser illumination configuration considered here was of the double-cavity, ND-YLF, diode-pumped type (LITRON LDY-300) and arranged such that all cameras were in forward scatter with respect to the illumination. A 50/50 non-polarizing, plate-type beam splitter was used to divide the beam into two, which were diverted and expanded to provide volumetric illumination at perpendicular angles, at positive x-direction and negative y direction (see figure 3.2). This illuminated the particles around the cavity because the shadows cast behind the cavity in the direction of one illumination angle was covered by the other. Each of the beams were expanded using a cylindrical lens and a low focal length convex lens. Knife edge filters were used to trim the beam profile to obtain a sharp and uniformly illuminated measurement volume. In order to provide a shadowgraph like back-illumination, two 50 watt DC powered LED lights were arranged directly in view of the camera positions. The cameras were inclined at planar angle of 45 degrees to the windows, and for two stereo-pairs, with an angle close to 35 degrees relative to each other.

The imaging setup consisted of five synchronized high-speed cameras (three Imager Pro HS high-speed cameras and two Phantom 640L high-speed cameras), fitted with 105mm Nikon objectives and scheimpflug adapters. The cameras were arranged in approximately 45 degrees of forward scattering angle to the laser illumination, and aligned at full forward scattering to the LED illumination by the use of an illumination prism. Four of the cameras were arranged as two stereo-pairs, with viewing facilitated by a two planed, water filled, acrylic viewing prism that was prepared in house. The angle between the planes of the viewing prism was such that each camera in the stereo-pair had an angle of 35 degrees in between them. The water introduced into the prism was first boiled and cooled in order to remove excess gases from the water, which prevents the accumulation of microbubbles on optical surface during the course of the measurement campaign. A thin layer of glycerine was introduced between the prism surface and the wall to avoid any internal reflections in the optical path. The camera sensors were cropped to a resolution of about 1100×700 pixels, which provided an imaging frame rate of 5 kHz for single frame particle imaging. The resulting particle image size is approximately 5 pixels. The maximum seeding density estimated was found to be 0.01 particles-per-pixel, or ppp, resulting in a typical inter-particle separation ($r_{2D} = 0.5ppp^{-1/2}$ [2]) of 5.5 pixels. In the experiments conducted in this work, the average inter-frame displacement is found to be 18 pixels, therefore, 3.2 times the inter-particle separation. We addressed this by performing a displacement estimation in the particle tracking step, which we describe later in §3.3.

3.2.3 Camera Calibration

Calibration images for the five cameras were obtained using a multi plane, double sided, dot target pattern (LaVision type 058-5) which was attached to a linear electromechanical

traverse. The target plate was aligned transverse to the flow with its centre located, as best as possible, at the mean centreline position of the cavity. The target plate was traversed parallel to the flow, with 11 calibration images taken at distances of 0.5 cm which is equal to the dot-pitch on the calibration plate, thus providing a $11 \times 11 \times 11$ structured point cloud grid of grid-pitch 0.5 cm. The calibration images recorded in the mid-plane slice of the calibration volume are shown in figure 3.2.

The camera calibration model chosen in the present work was of the pinhole type [64], with a third order polynomial mapping function used as the distortion mapping for the images. Details of the calibration approach are found in [43]. In this approach, the third order polynomial is used to rectify the images such that lines in the measurement volume, here defined as the object space, map as lines in the images, here defined as the image space, which preserves the world to image linearity required for a pinhole forward projection [18]. The images are then dewarped using the distortion mapping and a pinhole model is fitted to the calibration points. The pinhole projective mapping is given in the following manner. If $\tilde{\mathbf{x}} = [x\ y\ 1]$ represents the homogeneous image coordinates in dewarped image space, $\hat{\mathbf{X}} = [X\ Y\ Z\ 1]$ is the three-dimensional homogeneous coordinates in object-space, then the object space to image space projection model is given by:

$$\hat{\mathbf{x}} = P\tilde{\mathbf{X}} = \big[K[R|\mathbf{t}]\big]\tilde{\mathbf{X}}, \tag{3.1}$$

Prop.		Cam 1	Cam 2	Cam 3	Cam 4	Cam 5
$\tilde{J}$	[-]	0.99	0.99	0.99	1.00	0.99
α_x	[px]×10^4	1.55	1.48	1.40	1.72	1.41
α_y	[px]×10^4	1.56	1.44	1.40	1.63	1.41
s	[px]	-551.06	918.27	-31.9	-120.40	322.37
p_x	[px]	1293.20	-6.83	1991.5	1150.0	-84.45
p_y	[px]	520.0	731.27	905.95	1693	612.53
t_x	[mm]	199.56	-400.94	-78.85	-431.73	-439.09
t_y	[mm]	506.16	184.53	425.34	-140.16	34.50
t_z	[mm]	-755.70	-665.23	-667.79	-665.69	805.05
α	[^{o}]	164.51	-114.90	179.03	-78.44	-98.38
β	[^{o}]	54.70	54.84	55.83	58.48	-62.64
γ	[^{o}]	4.77	-86.60	170.55	-92.29	-91.02
f_{eff}	[mm]	143.10	127.24	121.71	149.47	106.76
f_{eff}/f_{lens}	[-]	1.36	1.21	1.15	1.42	1.01
ϵ_{cal}^{avg}	[px]	0.56	0.78	0.72	1.97	0.78

Table 3.2: Camera extrinsic and intrinsic parameters following the calibration. $\tilde{J}$ is the average area expansion ratio of the distortion mapping [43], α_x and α_y are the estimated focal length of the cameras in both directions and in pixel coordinates, s is the skew of the cameras, p_x and p_y are the camera centers in pixel coordinates, t_x, t_y and t_z are the camera translation vectors in object space, α, β and γ are the Euler angles of the camera rotation matrices, f_{eff} is the estimated focal length of the lens in object space following eq. 3.2, f_{lens} here is 105 mm, and finally, ϵ_{cal}^{avg} is the average reprojection error of the camera model to the calibration target.

where K, R and $\mathbf{t}$ are the 3×3 camera intrinsic matrix, 3×3 rotation matrix and translation vector respectively, and P is the 3×4 projection matrix. Table 3.2 shows the camera model parameters, excluding the distortion map coefficients, that are recovered from the calibration procedure. The average area expansion of the distortion map, $\tilde{J}$ [43], is close to 1, meaning that the distortion model does not account for the image magnification occurring at the window. Instead, this is absorbed into the estimated focal length of the lens. Following figure 3.3 and the focal length rationalization performed by [43], the focal

length ($f = \alpha_x/r_x = \alpha_y/r_y$, r_x and r_y are the dimensions of the pixel in units of object space) is rationalized to the true focal length of the lens in the following manner:

$$f_{eff} = \sqrt{\frac{\alpha_x \alpha_y \tilde{J}\tilde{n}^2}{(rsin(\theta))^2}}, \tag{3.2}$$

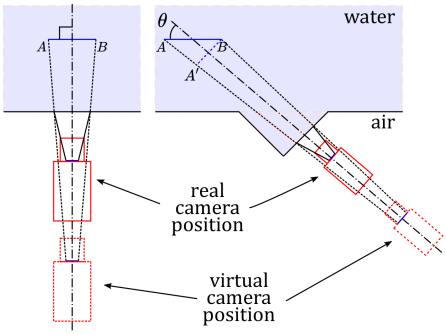

Figure 3.3: A schematic showing the camera and refractive surface configuration for rationalization schemes of the estimated focal length during calibration. Left: Rationalization scheme chosen by [43]. Right: Rationalization scheme chosen in the present work, using a single angle, θ, therefore similar to camera 5 of fig. 3.2.

where θ is the angle made by the estimated principle axis of the camera to the flow centreline [2]. Equation 3.2 tries to model the distortions that occur to the light cones as the light from the measurement volume projects onto the image sensor, through all the optical surfaces, and is a post-calibration check to see if the recovered camera parameters are sensible. Normalization of f_{eff} with 105mm yields values between 1 and 1.5, therefore the camera model is a reasonable approximation to the physical particulars of the imaging system. The normalization is close to 1 for camera 5, whose position and orientation relative to the measurement volume is best approximated by the rationalization scheme shown in fig. 3.3 and eq. 3.2. The average reprojection error, defined as the averaged geometric distance between the projected calibration points and their true locations [64], of all cameras were reasonably below 1 pixel with the exception of camera 4, which has an error close to 2 pixels. As the particle image size is typically of 5 pixels, the error of reprojection is smaller than the typical body length of the particle image, therefore the error is thought to be reasonable for particle image correspondence matching (or 3D-matching) across all views. The average reprojection error is used in the 3D-matching step to threshold the magnitude of the averaged image disparity, elaborated later in §3.3. This misalignment is usually treated by self-calibration techniques [14, 62], however, as each detected particle image correspondence set, defined as the set of particle images from each individual view corresponding to the same particle in real-world space, is triangulated in a least squares sense to obtain the 3D position and shape of the particle, self-calibration at best offers an advantage in performing the 3D matching. We estimate the resulting error later in §3.5.

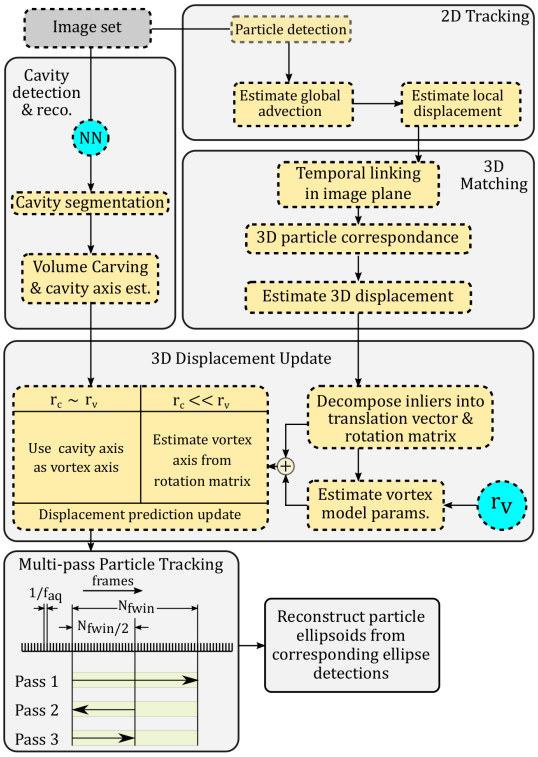

Figure 3.4: Schematic of the reconstruction procedure described in §3.3. Detection of particles and its displacement correction in the image plane are described in the 2D tracking step and elaborated in §3.3.2.1 and §3.3.2.2, respectively. The detection of the edges of the cavity has been described in §3.3.1.1, and the reconstruction of the visual hull has been described in §3.3.1.2. The 3D matching and 3D displacement update steps have been described in §3.3.2.3 and §3.3.2.4, respectively. The particle tracking step has been briefly discussed in §3.3.2.5 and is fully described in [42]. Finally, considerations for track postprocessing have been described in §3.3.2.6.

3.3 Reconstruction Procedure

A schematic of our reconstruction procedure is shown in figure 3.4. In the following, we describe the methods used. We have divided the discussion into two parts: in §3.3.1 we describe the segmentation of the cavity from our images, and the reconstruction of its three dimensional visual hull from multiple views, and in §3.3.2 we discuss the steps taken to perform particle tracking around the cavity.

3.3.1 Cavity Segmentation and Reconstruction

Image segmentation

As the resulting images (see figure 3.5b) are a composite of shadowgraphy and particle imaging, the contrast of the edges of the cavity is susceptible to degradation caused by the random appearance of bubbles, specular reflections on the interface and the scattered illumination from particles. The resulting image processing for cavity extraction is highly heuristic if traditional image processing approaches are utilized. Therefore, the segmentation of cavity from the images was carried out using a convolutional neural network [35]. This approach accounts for image variability by learning the various representations of the

[2] the true angle made is not considered here, instead, we estimate this angle for each view from their estimated rotation matrices.

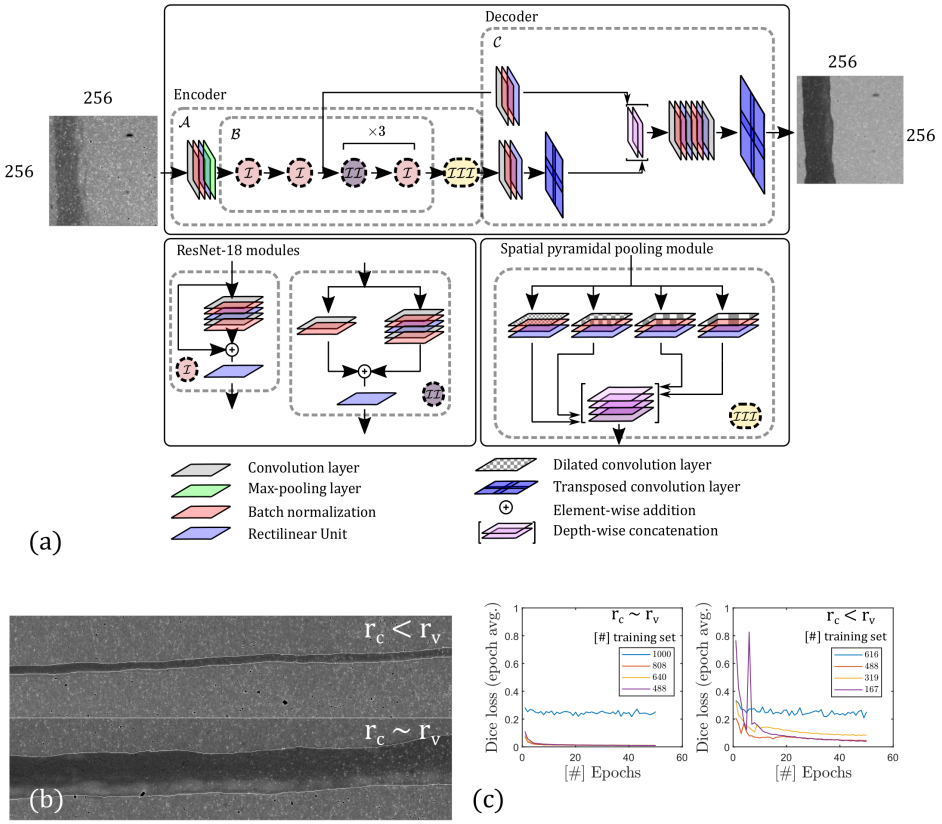

Figure 3.5: Figures highlighting the network model, cavity prediction and training error of the convolutional neural network. (a) Network layer graph of the DeepLabV3+ architecture [12]. Each distinct layer used in this graph has been highlighted below the schematic. Details of the parameters of each convolutional layer is avoided and the focus is instead on the arrangement of the layers. (b) Examples of prediction output of the trained network for two sizes of the vortex cavity, one where the viscous core radius, r_v, is larger than the cavity radius r_c, and the other case corresponds to when they are comparable in size. (c) The epoch averaged training loss for various sample sizes of the training set, and for each case of cavity images. The blue line corresponds to cases where the training set consisted of images not containing the cavity, showing that a better training loss is achieved if both classes are included in the images.

cavity's edges, occurring during the process of training the network with user defined edge data. The network architecture chosen in the present work was the DeepLabV3+ semantic segmentation model [12] which is a flexible encoder-decoder type of convolutional neural network (CNN) architecture, as implemented in MATLAB. In this model, the low level feature extraction of the cavity edges is carried out in the encoder stage, here represented by a ResNet-18 [27] network model which is passed through a set of dilated convolution layers as described in [12]. The decoder consists of a set of transposed convolution layers

that scale up the image representations achieved at the end of the encoder stage to input size, here 256 × 256 pixels. A schematic of the network architecture is provided in figure 3.5a.

For training the neural network, a set of approximately 2000 256 × 256 pixel images are extracted from the raw images and the perceived edges of the cavity are hand drawn. The image intensities are normalized by bringing the image intensity counts to the range [0,1] across the views and samples. The pixels in the training images are then labelled by a binary categorisation between two classes, i.e., the background (0) and the cavity (1). The images are split into a training set consisting of a maximum of 1000 images, and a testing set consisting of 600 images. 400 images were discarded from the dataset to minimize the effect of class imbalance, which biases the performance of the network according to the pixel population of each object class occurring in the training data. Data augmentation to the training set is applied, which applies geometrically transforms to the images in order to increase the training set size and improve the image segmentation performance by minimizing overfitting [41]. The data augmentation consists of a combination of rotation by -45 to 45 degrees, scaling by a factor of 0.7 to 1.3, reflection about both sides of the image, and finally, -10 to 10 degree shear in either dimension of the image. These transformations were easily facilitated within MATLAB's Deep Learning Toolbox. For the present work, a randomly chosen combination of data augmentation was applied in the training stage.

Training was carried out by back-propagation [53] using the stochastic gradient descent approach. The dice loss [57] was used to estimate the training loss between the CNN-segmented image and the hand drawn training image which also helps minimize issues due to class imbalance. Optimizing the training settings was conducted manually, which is not discussed here. The network is trained for a total of 50 epochs using a Nvidia GTX-Titan X GPU (2017). Each training iteration consisted of a batch size of 96 images, the training set was reshuffled following the end of every epoch. The initial learning rate was set to a constant equal to 0.05, which sets the step size in the direction of the gradient of the neural network coefficients. A drop rate schedule was employed to reduce the step size as training progressed. This was a factor of 0.94 reduction in the learning rate, performed every 2 epochs. The resulting training loss as the epochs progress is provided in figure 3.5c. The image inference is performed in blocks of 256 × 256 pixels, without overlap. An example of image segmentation for two different sizes of cavitation are shown in figure 3.5b. We assess the performance of the neural network against ground truth later in §3.5.1.

Visual hull reconstruction

The visual hull reconstruction was carried out using the following approach. A voxel grid encompassing the cavity's location was constructed in the measurement volume. Each voxel was projected onto the binarized image output of the neural network in each view, thus inferring its pixel class as described in the previous discussion. The visual hull was then reconstructed using the following expression:

$$VH = \prod_{v=1}^{5} Class_v([K_v(R_v|\mathbf{t}_v)]\hat{\mathbf{X}}), \tag{3.3}$$

where VH is a three dimensional matrix corresponding to the voxel centers, each containing the voxel's binary classification score in object space. A smooth representation is possible

by assuming the sides of the visual hull as tangent spaces for fitting splines, but this has been avoided in the present work. The reconstruction was performed in two iterations, in the first iteration a coarse voxel-grid was chosen to locate the cavity, which was subsequently refined in the second iteration. For this work, the final voxel grid had an isotropic resolution of 100 μm which is of the order of the azimuthal displacement of the particles between frames. The centreline of the reconstructed visual hull is estimated and the data is stored for use in the tracking step which we describe in §3.3.2.

3.3.2 Particle Detection, Reconstruction and Tracking

Particle detection and characterisation

The particle images were dewarped and preprocessed by background subtraction, min/max filtering and intensity normalization. Particles and bubbles in the image were detected by detecting intensity peaks and fitting ellipses to the particle intensity speckles using the approach described in [42], where each particle ellipse is represented by the generalized quadratic equation of conics in homogeneous coordinates (that of $\hat{\mathbf{x}}$):

$$\hat{\mathbf{x}}^T \mathbf{C} \hat{\mathbf{x}} = 0, \tag{3.4}$$

where $\mathbf{C}$ is a 3×3 symmetric matrix containing the coefficients of the fitted ellipse. The ellipse description of particle images is atypical in particle tracking literature, but is advantageous for the following reasons. Firstly, in diffraction limited imaging conditions, the ellipse can be interpreted as an error ellipse for the location of the centre of the illuminated particle. This allows having a higher camera disparity threshold when performing the correspondence matching. Secondly, the ellipticity accounts for astigmatism and other imaging artefacts not accounted by the camera calibration model, but encountered in the present imaging system. Most importantly, the description of the ellipse as a generalized conic (eq. 3.5) allows using the projective framework for reconstructing the three-dimensional generalized quadric from multiple views using the approach described by [15]. The quadric in this case is an ellipsoidal region that covers the location of the particle, based on its intensity distribution in different views. For Q being the 4×4 symmetric matrix containing the coefficients of the ellipsoid, the generalized expression for a quadric in homogeneous object space coordinate system is given as follows:

$$\hat{\mathbf{X}}^T \mathbf{Q} \hat{\mathbf{X}} = 0. \tag{3.5}$$

The ellipsoidal representation of the particle can be interpreted as a region in object space that contains the true particle centre in diffraction limited imaging. When the object size is larger, the ellipsoid is then an approximation of the visual hull of the object. This can later be exploited to estimate the size and shape of nuclei as they interact with the vortex. In the present work however, we show in §3.5 that the measurement errors in the present imaging setup are too large for studying the shape of nuclei as they interact with the vortex.

Two dimensional displacement estimation

As the typical imaged inter-frame particle displacement of 20 px was larger than the inter-particle separation estimated from the image ppp value, of approximately 5 pixels, the particle tracking is expected to suffer. To reduce this effect, an initial displacement

estimate of each particle in the axial direction was performed. This was carried out by first performing a cross-correlation of the full image with that at the previous and subsequent timestep. Each correlation map consisted of two peaks, each of which signify a global advection and a swirl component. The double peak condition arises from the fact that particles in front of the vortex cavity swirl in a direction opposite to that behind the vortex cavity in the images. The global advection was estimated by taking the midpoint of the line joining the two correlation peaks, and, the displacement is averaged over a sequence of 3 frames centered around the frame of interest. The estimated advection was used to shift the frame subsequent to the frame of interest in the direction of the flow and the remaining swirl component was then estimated by centering each ellipse detection on a 15×15 pixel window and performing local cross-correlation across a two frame sequence of advection corrected images to estimate each particle's displacement at the subsequent frame.

Particle correspondence matching

The next step involves the correspondence matching of particle image detections across multiple views leading to an estimation of the three-dimensional positions of the detected particles/bubbles. The correspondence set of each ellipse in other camera views were found by matching epipolar lines of each detection projected onto the other camera image planes in a manner similar to that done in [62]. The allowable disparity between the epipolar line and particles is taken to be a maximum of 0.5 times the body length of the particle ellipse detection, denoted by a normalized reprojection error shown in eq. 3.6, figure 3.6, and described subsequently in this section. The reprojection error estimated at the end of the camera calibration process was also considered in the matching procedure by adding it to the disparity threshold in the matching procedure. In the present work, particles matched with a minimum camera cover of 3 views to a maximum of 5 views were considered. This variable camera cover introduces several spurious matches, which were filtered out in the track postprocessing step. The average disparity of the triangulated position of the particle is characterized by the following metric. If $\mathbf{C}$ is the the conic vector for a detected ellipse in the dewarped image space, with centre $\hat{\mathbf{x}}_c$, is given by the coefficients $[C_1\ C_2\ C_3\ C_4\ C_5\ C_6]$, and if E is a quadratic expression defined for any point $\hat{\mathbf{x}}$ such that:

$$E(\hat{\mathbf{x}}) = C_1 x^2 + C_2 y^2 + C_3 xy + C_4 x + C_5 y + C_6,$$

then, the averaged normalized reprojection error for the reconstructed particle, here known as the average camera disparity, is then given by:

$$\epsilon^*_{reproj} = \sum_v \sqrt{\left|1 - E(\hat{\mathbf{x}}_p)/E(\hat{\mathbf{x}}_c)\right|} / \sum v, \tag{3.6}$$

where c denotes the centre of the detected conic, p denotes the centre of the projected conic and v denotes the camera views that contain the particle correspondence. As shown in figure 3.6, ϵ^*_{reproj} is equal to 1 if $\hat{\mathbf{x}}_p$ lies on the boundary of the conic, and 0 if it lies on the conic centre. This definition is similar to the Mahalonobis distance if the conic vector is interpreted as the error ellipse, motivating some of the prior discussions on the advantages of a conic-quadric representation of the world-to-image transformations of particle image intensity distributions.

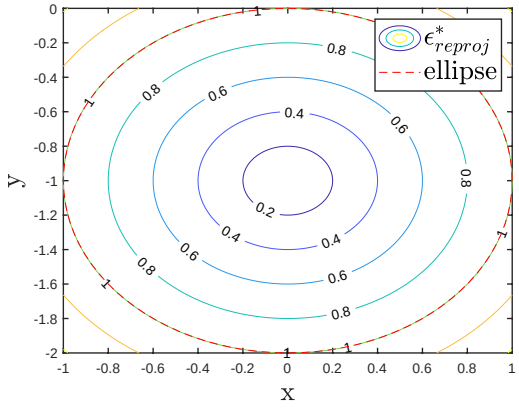

Figure 3.6: Contour-map of the normalized reprojection error (ϵ^*_{reproj}) for one view as given by eq. 3.6, for an example conic.

Three-dimensional displacement prediction

Following the image displacement estimation (§3.3.2.2) and correspondence matching across views (§3.3.2.3), the three-dimensional displacement of each detection was estimated from its displacement in each view as a vector difference between the triangulated three-dimensional position of each particle and the same for its displaced position [42]. Because particles in front of the vortex-cavity displace in the direction opposite to particles behind the vortex-cavity, their contrasting displacement directions make it harder to estimate local displacement of particles. The tracking, then, cannot be carried out purely by an estimate of the local image displacement alone, specifically near the cavity axis, by the cross-correlation technique used in §3.3.2.2. Therefore, this displacement estimate had to be corrected in 3D in a step between the particle correspondence matching and trajectory estimation. Under the condition of low pixel displacement of each particle (less than one body length of the particle image), this step is otherwise not necessary and the three-dimensional displacement estimate calculated using the individual two-dimensional displacements of each view of a particle reasonably locates its position in the next timestep.

Using the detected cavity axis from the visual hull reconstruction, a Lamb-Oseen vortex was fitted to the displacement estimate of particles located 25 mm radially outwards of the cavity axis, assuming a viscous core radius of 10 mm. This was achieved by performing a linear decomposition of the selected displacements into a rotation and a translation, and fitting the vortex model to the angular displacements extracted from the rotational component. To avoid the influence of outliers, the vortex model fitting was performed in a least-squares sense using a RANSAC like approach [13]. The estimated 3D particle displacements from §3.3.2.4 were sampled at random, and a consensus on outliers and inliers in the rest of the sample population was built up using a threshold to the residual of the fit. If outliers were less than inliers, the inliers were pooled and the vortex model was refitted. This process was iterated until the vortex model converges. In this present work, the outlier density was relatively small in regions far away from the vortex-cavity, and only two RANSAC iterations were taken to estimate the circulation strength of the vortex in the Lamb-Oseen vortex model. The three dimensional displacements of each reconstruction was then updated using the vortex model for the angular displacement and the global axial displacement. The particles were displaced in the azimuthal direction using

a rotation matrix and the fitted Lamb-Oseen vortex model. It is possible to avoid this step entirely if there are no tracer particles added to the flow, which would mean that the the flow would be inhabited largely by microbubbles, and the two dimensional estimate alone is sufficient for the tracking. This is a lower number of ambiguities introduced like that in the case of a flow seeded with a relatively larger population of tracer particles, which otherwise corrupts the result of the two-dimensional cross-correlation step (see §3.3.2.2), and subsequently necessitates the steps taken in this discussion.

Particle tracking and reconstruction

The details of the tracking algorithm are discussed in [42]. To briefly summarize here, the tracking algorithm finds the position of each particle in the next timestep by seeding new tracks for each particle in 3D using the estimated 3D displacements of each particle from the previous steps, as well as the extension of track using its position in previous frames. Therefore, two separate estimates of each particle's next position is available, and a selection between them can be made which minimizes the reprojection error of the particle. This approach helps against tracks breaking due to optical obstructions encountered in the flow. For the extension of a track into the subsequent frame, the track was also linearly extended to two subsequent frames using a stencil over 3 previous timesteps, acting as a redundant prediction of the particle's position alongside the displacement estimate discussed in §3.3.2.4. Alternative track extension approaches such as a third order polynomial, or approaches found elsewhere in literature (see [55, 58]) were considered. However, it was found that a linear track extension worked best for the present measurements.

As mentioned previously, the track extension was based on an approach which selects particle positions such that the average reprojection error (described in eq. 3.6) is minimized and the track length is maximized. The tracking was carried out in batches/windows of the time-series data and over multiple passes, both forwards and backwards in time. In the present work, each window had a size of 50 frames, defined here as N_{fwin} in figure 3.4, and a total of 3 passes through a window was performed as described in figure 3.4: one forward pass in time two backward passes through in time. The next window sequence overlapped the prior by 25 frames. A key feature of the tracking approach is that, unlike other approaches (for example in [55, 58]), the particle detections are used more than once to span tracks. This is due to multiple choices that can occur when a track is extended based on particle positions in the previous timesteps, and due to the estimated three-dimensional displacement of each particle between frames, as described in §3.3.2.4. This step was necessary in order to allow the track to resolve matching ambiguities occurring due to the opacity introduced by the cavity, and due to the higher probability of spurious matches when the camera cover over a particle is low. As a result, duplicate tracks for the same particle detection were found in the reconstructions if all constraints imposed by the tracking approach was satisfied (see table 3.1). This was filtered out in the post-processing stage, described subsequently in §3.3.2.6. Following the tracking step, the quadric representation of the particle/bubble was reconstructed using the approach described in [15]. We later discuss in §3.5 that the error of camera calibration and misalignment of cameras during the course of the measurement campaign is absorbed by both the centre of the projected particle reconstruction and its size. This has been utilized to obtain an estimate of the error of the displacement measurement.

Track post processing

As described above, the total number of reconstructed particles is significantly larger than that detected in the images (see table 3.1). As multiple tracks reprojected onto the same particle in the image, the duplicate tracks in the raw track data were removed such that only the longer tracks among the duplicates was registered, yielding one unique track per reprojection onto a particle. Tracks inside the cavity were also removed and other spurious tracks were removed by thresholding the radial and tangential velocity such that large radial velocities of the trajectory ($\geq 1m/s$) and non-zero tangential velocities are avoided. Additionally, tracks lower than five timesteps were also removed. The total filtered particle count was found to be substantially reduced, and well below the total number of particles detected in the images (see table 3.1). A three-dimensional cubic polynomial was used for smoothing the tracks. The radial position of each smoothed particle position relative to the local cavity centre was estimated, and, the tracks were binned accordingly. In this work, 1 mm bin spacing in the instantaneous radial coordinate was chosen. This way, wandering induced smearing to the binned velocities was avoided.

3.4 Results

The particle tracking reconstruction described in §3.3 was performed for a total of 1000 frames per test-case, corresponding to a physical time of 0.2 seconds, whereas for the visual hull reconstruction, a total of 14000 frames were processed, i.e., 2.8 seconds. For each reconstruction, a total of 9000 brightest particles per image (N_I) were considered in the particle detection step (see §3.3.2.2), largely due to memory considerations and the developing nature of the tracking code. This resulted in an inter-particle separation distance of approximately 4.6 pixels. The total reconstructed particles per timestep, N_R, following the tracking step (see §3.3.2.5) was significantly higher than N_I, with N_R/N_I approaching 5.5. Following the track post processing step (see§3.3.2.6), the total number of tracks reduced significantly, yielding an inlier particle per timestep value, N_{IN}, with N_{IN}/N_I approximately at 0.37. While low, this is reasonably below a value of 1, meaning duplicate entries were removed under the simple segmentation criteria described in §3.3.2.6.

The discussions in this section is as follows: In §3.4.1 the shape reconstruction data is described, where its spectral content is analyzed, and in §3.4.2 the particle tracking results are described and the influence of the presence of the cavity to the outcome of the reconstruction approach is highlighted. A comparison against time-resolved Tomographic PIV reconstructions is also made.

3.4.1 Reconstructed Visual Hull

Figure 3.7 consolidates the results of the visual hull reconstruction approach. Following the visual hull reconstruction procedure using eq. 3.3, no other post-processing step was performed to smoothen the visual hull. An instantaneous reconstruction of each test-case can be found in the figure, showing an approximately 6 cm long visual hull. Respectively for the three cases, the reconstruction is 176, 3.1 and 2.85 cavity diameters long. In contrast to measurements by Pennings [47], where more than 4 chord lengths of the cavity was imaged using two-camera shadowgraph imaging, the present imaging setup only covers approximately half a chord length. As the spatial dynamics of a vortex

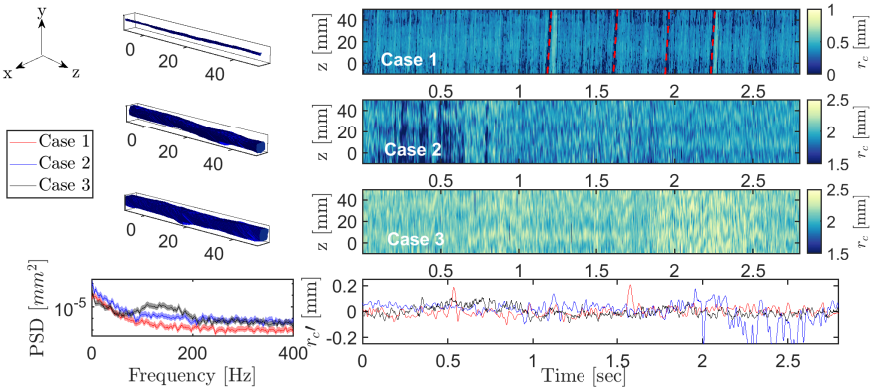

Figure 3.7: Figures showing the outcome of the shape-reconstruction procedure. The reconstructed visual hull of the cavity in object space is shown in the left figures, and, space-time plots of the effective visual hull cross-sectional radius, along its length, are provided in the right figures. For Case 1, reconstruction artefacts such as convective-gaps in the space-time plot, and those introduced by the windowed image-segmentation procedure are indicated. These artefacts are absent in the other cases where the cavity is much thicker in diameter. The bottom figures are respectively the axis averaged cavity radius variations on the right, and a Welch estimate of their respective power spectral density on the left, with 95% confidence bounds.

cavity are largely dominated by waves propagating along its length, the spectral content of the present reconstruction approach is lesser than that offered by synchronized two-camera shadowgraphy. To assess the spatio-temporal spectral content of the present reconstructions, a space-time plot of the diameter of the reconstruction visual hull is provided in figure 3.7. The effective diameter was estimated from the cross-sectional area of the cavity reconstruction along the z-direction.

In terms of quality of the reconstruction, the visual hull data of Case 1 suffers from several artefacts. These cavity reconstructions were heavily influenced by the presence of relatively large bubbles in its vicinity, which are captured as gaps in the space-time diagram of Case 1, highlighted by positively sloped red lines (indicating convection) in the space-time diagram of Case 1, figure 3.7. There are a few reasons why the thin cavity case is challenging: firstly, the mean cavity diameter of Case 1 is of the order of the resolution of the visual hull and the size of the reconstructed particles, and secondly, the neural network model used here was not trained on the cases where larger travelling bubbles block one or more of the camera view, therefore cannot extrapolate to all scenarios encountered in the time series. More importantly, very thin cavities such as in this case are highly intermittent, something not captured presently in the samples used to train the CNN model. In contrast, thicker cavities do not have these issues. The microbubbles in its surrounding are typical an order of magnitude below its mean diameter, therefore did not need to be accounted for in the training set. By definition, they are also much larger in diameter than their voxel resolution.

The reconstruction of the cavity in 3D plays an important role in defining a geometric axis of the surrounding vortex for conditionally averaging the measured velocity fields and subsequently studying the vortex's kinematics. The reconstructions are also useful for

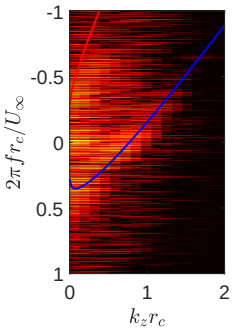

Figure 3.8: Two-dimensional amplitude spectrum of the diameter fluctuations of the cavitating vortex in Case 3. For illustration purposes, the dispersion lines of the breathing mode of a vortex cavity are plotted as derived in equation 4.79 in Chapter 4 of [8]. The corresponding values of the parameters to that equation are: $n = 0$, $\tilde{W}_c = 1$, and $K_\sigma = 0.5$. Both 0^+ and 0^- curves have been plotted in red and blue colors respectively.

the spectral analysis of the cavity dynamics in order to understand the noise radiated by it. In figure 3.7, the power spectral density estimate of the spatially averaged cavity radius is provided, estimated using Welch's spectral density estimation method [59]. We used a window of 2048 timesteps, an overlap of 50% between each window, and each window was preconditioned using the Hamming window function. From the power spectral density estimates for each reconstructed case, as shown in figure 3.7, not all cases contained the expected spectral content discussed in [8]. As shown in figure 3.7, Case 3 has a clear, broadband hump in the frequency range of 100 to 200 Hz that is absent in the other cases. This maybe largely attributed to the cavity size being too small for case 1, and due to the transience of the cavity's dynamics in case 2. As case 3 contains some spectral content, largely owing to its developed size, the spectral content of Case 3 has been analyzed further in both space and time, similar to that found in [8, 46]. For doing so, a two-dimensional Fourier analysis was performed on the space-time diagrams of figure 3.7, with overlap and window preferences similar to that in the 1D spectral analysis discussed previously. The resulting frequency-wavenumber plots are shown in figure 3.8, where the wavenumber space has been normalized using the spatially average cavity radius value of 2.1 mm from table 3.1, and the frequency space has been normalized using $2\pi r_c/U_\infty$ as a reference time scale. Figure 3.8 shows interesting spectral content that bears qualitatively semblance to the zeroth order mode shape signal shown by Bosschers [8]. This mode shape corresponds to a 'breathing' behavior of the vortex cavity, involving oscillations in the diameter of the cavity along its length, and in time, and is thought to be responsible for the tonal noise that the vortex cavity characteristically radiates into its far field [4]. The dispersion line of this modeshape from Bosscher's dispersion model has been plotted for reference in figure 3.8 using parameters that were manually tuned using the reconstructed data as described in the figure. The presence of this signal, despite the low wavenumber resolution, is promising for further use of the present experimental approach to study vortex cavitation induced underwater radiated noise. Further analysis falls outside the scope of this work.

3.4.2 Measured Velocity Fields

In this section, the conditionally averaged velocity vector reconstructions are described. For comparison, the averaged velocity using the reconstruction procedure described in §3.3 is compared against a standard tomographic PIV [21] reconstruction. We first describe

how the conditionally averaged vortex velocity profiles were obtained.

For the particle tracking data, the post-processed particle displacements (following §3.3.2.6) were first shifted in order to have the cavity axis at the origin. For centering the velocity vectors, the centerline of the cavity reconstruction was utilized. In order to avoid transferring the statistical noise of the visual hull reconstruction to the positions of the shifted vectors, the measured visual hull centerline was approximated by a first order fit. The shifted particle displacements were then binned into 2 mm radial bins for each timestep, with a bin overlap of 1 mm, yielding an effective vector spacing of 1 mm in the radial direction. This finally yielded the velocity profiles in the top panels of fig. 3.10.

For the tomographic reconstruction, a standard polynomial calibration function was used over the calibration images described in §3.2.3, which was of third-order in the transverse direction [56], and linear in the axial direction. The coefficients of each camera's polynomial calibration was re-estimated using multiple self-calibration steps [62] in order to bring the reprojection error to below 1 pixel. In contrast to the tracking procedure, where 3D reconstruction of the particle location is based on a correspondence matching step across multiple views (see §3.3.2.4) and least-squares triangulation [64] estimates a best fit to the correspondence set, the tomographic approach does not have a correspondence matching step, and requires a low reprojection error for accurate 3D reconstruction of the particles [21, 62]. Owing to the low all-round camera cover caused by the imaging difficulties highlighted in fig. 3.1, self-calibration was performed using particle image data from the thin-cavity case alone, and the resulting calibration was applied to all cases considered in table 3.1. As all three cases were imaged in succession, calibration drift induced bias errors are minimized. The tomographic reconstructions were carried out in LaVision's DaVis software (version 8.1), using 9 MART iterations and velocimetry was performed on the particle reconstructions using $64 \times 64 \times 64$ voxel rectilinear interrogation boxes with 50% overlap. In order to remove outliers in the cross correlation step, a threshold of 0.3 was applied to the correlation peaks, alongside the universal outlier detector proposed by Westerweel and Scarano [60]. The geometric center of the vortex velocity profiles in each transverse plane was estimated using the centering approach by Graftieaux [26], which was used to center each transverse plane. Because the centering approach is fundamentally integral in nature, contributions by noisy or erroneous vectors are minimized. The resulting center detection is more accurate than gradient based approaches which detect the location of peak axial vorticity. For estimating the center, the average was performed over the 25×25 vectors obtained per plane. Finally the binned vectors were averaged along the axial direction using a transverse vector bin spacing of 1 mm, yielding the velocity vector profiles in the bottom panel of fig. 3.10.

Conditionally Binned Vector Spatial Density

Figure 4.5 shows the vector density that was accumulated in 1000 timesteps for each case and reconstruction approach. Density maps were obtained by binning particle positions for all timesteps over a bin width of 1 mm. For either approach, the density maps clearly show less vectors at the center of the plots, indicating that the centering of the transverse planes were performed successfully. In both reconstruction approaches, the effect of larger cavity radii is apparent, as the region of low vector density (about $\mathcal{O}(10^0) - \mathcal{O}(10^2)$) in each of the plots progressively occupies a larger central region as the cavity size increases. Interestingly, the focality breakdown phenomenon expected in figure 3.1 is also clearly

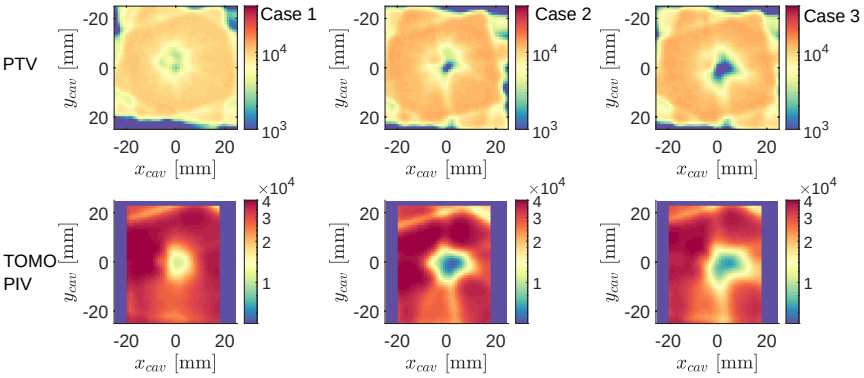

Figure 3.9: Axially accumulated, case-wise velocity vector densities using both the particle tracking approach (top) and Tomographic PIV [21] approach (bottom). The color bars presented show bin counts and therefore are unitless. Both densities were obtained after centering the vector velocity profiles using centering approaches described in §3.4.2.1 such that the position of the cavity is at the origin.

seen in each of the cases, but the vector density difference between 5-focal zones and zones of lower camera cover is observably larger in tomographic PIV reconstructions than in the particle tracking approach. This was the expected benefit of the focality agnostic particle tracking approach. Yet, some low-focal streaks are observed in the density maps of the PTV approach, which should be improved on in subsequent work.

Conditionally Averaged Vortex Velocity Profile

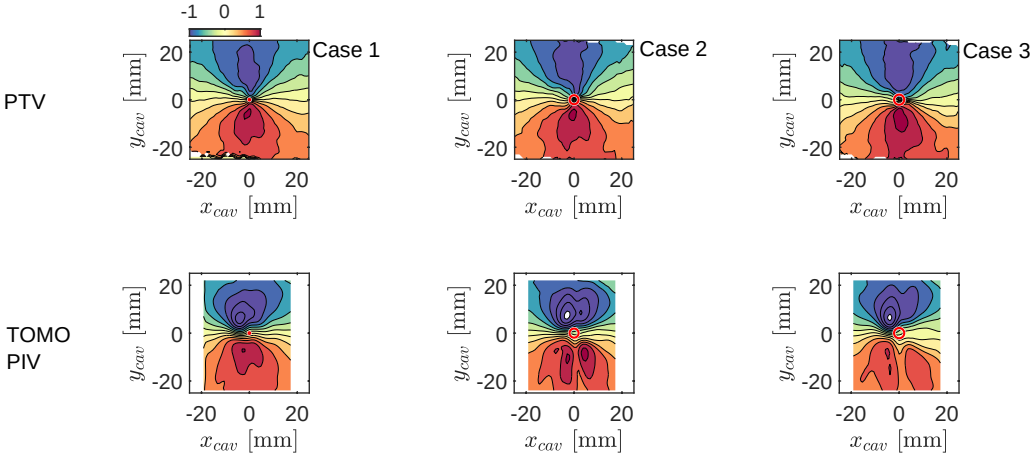

Figure 3.10: Axially averaged transverse velocity profile of the measured vortex velocities, using conditional averaging techniques described in §3.4.2.1. The color bars presented are in the units of $[m/s]$. The position and size of the mean cavity diameter is also shown in the plot.

In contrast to the density maps discussed previously, the conditionally averaged transverse velocity profiles of the vortex convey a different data quality by both reconstruction approaches. Figure 3.10 shows the binned velocity vector maps in the transverse plane using the approaches described in §3.4.2. Despite similar density plot behavior, the vector data of tomographic PIV reconstruction are severely affected by the presence of the opaque vortex cavity for all three cases. For cases 2 and 3, the severity is more pronounced and can be seen in the break-up of the velocity profile in zones where the camera cover is not maximum. These errors arise from spurious correlations that were thought to be mostly filtered out by thresholding the correlation peaks, but evidently have remained in the velocity statistics. Overall, the quality of tomographic PIV data is inadequate in making inferences about the velocity field around the cavity, as was expected previously.

Unlike the artefacts seen in the velocity profiles of the tomographic approach, the particle tracking data has a visibly better quality and the data is promising. The spurious gaps previously discussed were entirely avoided in the PTV data, and due to the focality agnostic approach, the reconstruction volume is larger than the tomographic PIV approach. The velocity data is also more symmetric, with minor asymmetries caused by lower vector density at the top region of the plots, beyond y_{cav} of 20 mm. These results strongly motivate developments in focality agnostic approaches, when applied to flows where the camera cover is severely degraded by opacity. A further assessment of the shape reconstruction and velocity field is provided in the coming section, §3.5. In the following discussion, only the PTV data will be considered.

3.5 Data Quality Assessment

In the present work, data quality assessment was achieved in several ways. Firstly, the quality of the cavity segmentation was assessed against the ground truth data that was set aside as described in §3.3.1. This was done by estimating standard quality metrics used in deep learning based image segmentation, and is discussed in §3.5.1. The assessment was conducted using metrics that compare the overlap between the segmented and ground truth pixel, and the matching of boundaries between the segmented classes against that in the ground truth.

The approaches considered for assessing the particle tracking data are discussed in §3.5.2. Firstly, a velocity divergence map of the mean flow statistics was estimated, which highlights deviations away from mass conservation in the wetted flow of the vortex cavity. Secondly, the performance of the tracking approach was assessed by estimating the relative probability of track extension for the present data, and comparing it to that theoretically derived for multi-frame particle tracking by Adrian & Westerweel [2]. The third approach used was to compare the effective diameter of the reconstructed particles against an expected average size of 50 μm. This is the advantage of the present approach where the particles were reconstructed as ellipsoids from their corresponding ellipse detections in multiple views. Finally, the normalized reprojection error distribution of the particles given by eq. 3.6 was estimated. This normalized reprojection error in the dewarped image plane was also used to estimate the particle displacement error in 3D. Considerations for the size of the particle were also included in the displacement error estimate.

3.5.1 Shape Reconstruction Data

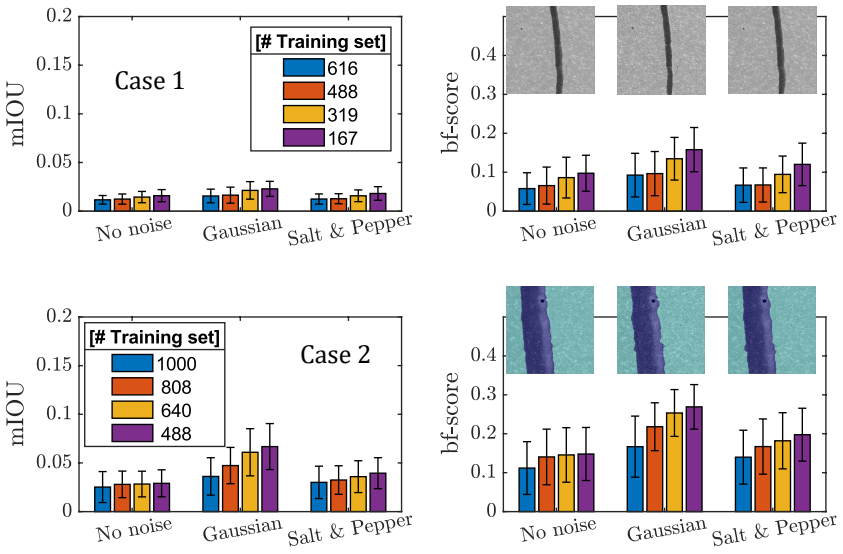

Figure 3.11: Estimation of the similarity scores (eq. 3.7 & eq. 3.8) of the trained neural network model, for cases 1 and 2 (table 3.1), from ground truth data. The averaged similarity scores are plotted as bars, with the 95% confidence bounds of the spread of the estimator given by the error bars. The similarity scores are arranged to highlight the effect of varying the training sample size (given by their color), and, the effect of added image noise (both gaussian and salt & pepper noise) on the cavity segmentation performance.

CNNs are sensitive to the training procedure which contains many heuristic features such as the training set size, the initial learning rate and the rate of reduction to the learning rate as epochs progress, the total number of epochs considered, and among others, the amount of noise present in the images. A sensitivity analysis was conducted by considering two common image segmentation metrics: the inference-over-union loss (also called the Jaccard Index) averaged over the two classes (background and the cavity) which is defined in this work as:

$$\epsilon_{mIOU} = 1 - \sum^{classes} \frac{\text{Prediction} \cap \text{Ground Truth}}{\text{Prediction} \cup \text{Ground Truth}}, \tag{3.7}$$

where mIOU is the *mean inference over union* loss over the two classes. The second metric is the boundary f1 score described in [16] and defined as:

$$\epsilon_{bf-score} = 1 - \frac{2 \cdot \text{precision} \cdot \text{recall}}{\text{precision} + \text{recall}}. \tag{3.8}$$

Here, precision is the total number of points on the boundary of the prediction that are close to that of the ground truth within a tolerance, and, recall is the total number of points on the ground truth that are close to that of the prediction within a tolerance. The tolerance here is set to the standard value of 0.75% of the image diagonal, hence 2.71 pixels.

In the case of the mIOU loss, the loss estimate is biased towards the predicted binarized image, whereas, the bf-score is biased towards the boundaries of classes in the predicted binarized image. Therefore, the latter is a more stringent error measure for the semantic segmentation of the cavity in the images.

In the assessment, ground truth data from cases 1 and 2 were only considered, as cases 2 and 3 are similar in average cavity diameters. Figure 3.11 provides the performance of the trained CNNs against the similarity scores described previously. With regards to the training set size, we find that the size of the training set has a marginal influence on the mIOU score for thinner cavities, which is likely due to the larger ratio between pixels of background class to the cavity class, compared to that in thicker cavities. Even in the case of relatively thicker cavities (case 2), we find that differences in training set size only manifest when the noise added into the images is gaussian. Further, the mIOU error is found to be higher for cavity images from case 2 in comparison to those from case 1. These observations indicate that a large number of background class pixels included in the mIOU metric (eq. 3.7) dilutes the outcome, making it a less reliable measure of segmentation performance compared to the bf-score which will be discussed subsequently. There were no significant differences in the performance of the trained CNNs taking the mIOU metric into account with the exception of the gaussian noise added to case 2 data which shows an increasing averaged mIOU metric over the test set. Even in this case, the 95% confidence intervals of the mIOU metric for both cases largely overlap so that the comparative error in the performance of the CNN with different training set sizes is small.

In contrast to the mIOU metric, the bf-score has a larger average magnitude for all training set sizes and noise levels added. The overall boundary detection accuracy, given by the bf-score, is between 10 and 20%, while the mIOU score is reasonably at or below 5% for all cases without noise. This large difference in magnitude is attributed to the behavior of the bf-score metric, which focuses exclusively on the mismatch in boundaries between the segmented classes. The choice of the dice loss as a training loss [57], which is a differentiable loss function related to the mIOU score, also explains some of the reasons why the mIOU score has a small magnitude while having a relatively large boundary mismatch. In the case of the bf-score, the influence of added noise to the ground truth data is more clearly observed. Overall, the magnitudes of the assessment criteria were considered acceptable for the present work. Several improvements can later be accommodated for both cavity segmentation and microbubble identification with regards to when the cavity is in a state of collapse.

3.5.2 Velocimetry data

We first assess the data quality by evaluating the mass conservation condition on the cavity centered and time averaged velocity field data in 3D, and in the wetted flow region. Mass conservation for the mean wetted flow around the vortex cavity is given in differential form as:

$$\nabla \cdot \mathbf{u} = \frac{\partial \overline{u}}{\partial x} + \frac{\partial \overline{v}}{\partial y} + \frac{\partial \overline{w}}{\partial z} = 0. \tag{3.9}$$

The computed divergence is presented in figure 3.12 as $-(\partial\overline{v}/\partial y + \partial\overline{w}/\partial z)$ in the vertical axis and $\partial\overline{u}/\partial x$ in the horizontal axis, similar to that found in [30]. The spatial gradients

of the mean velocity were estimated using the conditionally averaged velocity profiles of the cavity after the cavity centering was performed. Estimating the same from the instantaneous flow field was avoided due to concerns about the accuracy of the spatial gradient estimation in the absence of velocity vectors in certain locations and timesteps of the data. The results quantify the error in divergence of the flow and suggest that the mean flow satisfactorily follows the zero divergence condition, with marginal spread about the indicated diagonal in the figure.

The performance of the tracking approach is assessed using the expression for the probability of tracking a tracer particle over a sequence of frames given in eq. 7.72 of [2]. For convenience, this expression is reiterated here as follows. The probability of tracking a tracer for N_f frames is given by the estimator:

$$Prob(L \geq N_f) = \epsilon_t^{N_f}(1 - exp^{-N_l}), \tag{3.10}$$

where, ϵ_t is the tracking efficiency, and assumes values between 0 and 1, L is the length of the track, and N_I is the average number of particle reconstructions per frame. ϵ_t accounts for the amount of particles lost due to tracking inefficiencies when a set of detected particle tracks are extended to the next frame. An ϵ_t value of 0.8 means that approximately 80% of the tracks are extended into the subsequent frames. The relative detection probability is estimated from the experimental data by assembling and counting the total tracks corresponding to track lengths from 1 to 25 frames (N_f). This is done for both the raw tracks from the reconstruction procedure, and tracks recovered after the post processing step discussed in §3.3.2.6 where the minimum track length had been set to an N_f of 5. The results are plotted alongside eq. 3.10 for ϵ_t values from 0.5 to 0.9 and shown in panel a of fig. 3.13. The results suggest that the tracking code in general has an efficiency in the range of 70-80%, where the efficiency is higher when the cavity size is smaller. This is expected because the reduced optical blockage by the cavity allows a better matching quality. In the post processed tracking data, all the data sets have a tracking efficiency in the neighborhood of 90% which is highly encouraging. This means that the post processing step prioritized sets of tracks that have a high chance of extension to the next frame.

The shape and size of the reconstructed particle can be recovered from its quadric representation, and comparison with the manufacturer specified size of the particle gives a

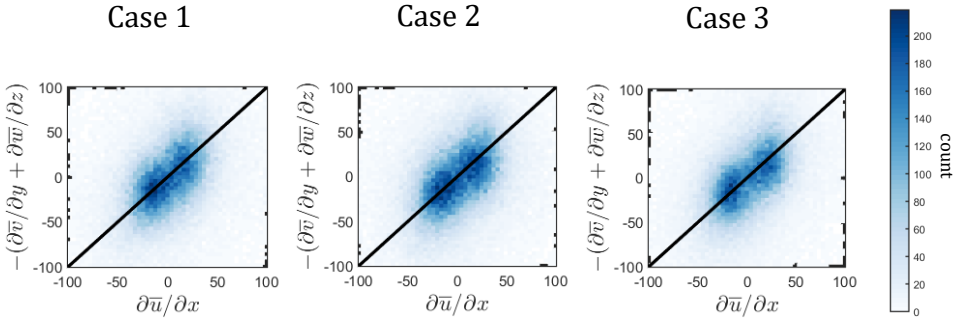

Figure 3.12: Two dimensional histogram of $\partial\overline{u}/\partial x$ and $-(\partial\overline{v}/\partial y + \partial\overline{w}/\partial z)$. Diagonal indicates zero divergence, and densities normally outward of the diagonal are indicative of measurement error.

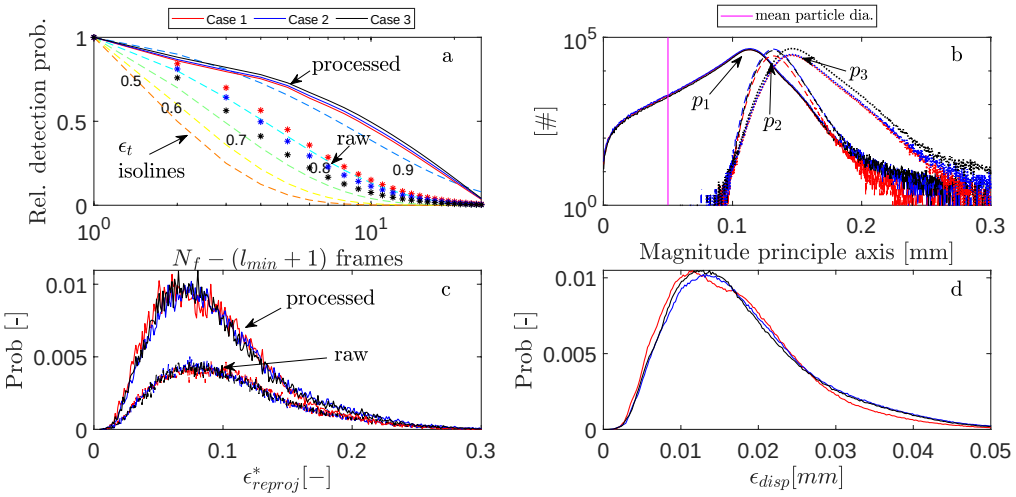

Figure 3.13: Quality of the reconstructed particle tracks. (a) Relative detection probability estimated from the track histogram of the post-processed particle tracks. Dashed lines are isolines of tracking efficiency, ϵ_t (see eq. 3.10). l_{min} represents the minimum track length used for the estimation of the relative detection probability, here 3. (b) Histogram of the magnitude of the principle axes (p1, p2, and p3) of the reconstructed particle quadrics. (c) Probability distribution of the normalized reprojection error (ϵ^*_{reproj}) for both raw and processed particle reconstructions. (d) Probability distribution of the magnitude of the displacement uncertainty of the post-processed particles from eq. 3.11.

good indication of the accuracy of the reconstruction. In the present work the manufacturer data provides a mean particle diameter of $50\mu m$ and standard deviation of $5\mu m$. As the particles are reconstructed as ellipsoids, their size can be characterized by their individual principle axes, $\mathbf{p} = (p_1, p_2, p_3)$. The magnitudes of the principle axes are provided in figure 3.13(b), showing that the reconstructed particle size is much larger than the manufacturer's specifications and that its shape is ellipsoidal. Histograms of the estimated normalized reprojection error, ϵ^*_{reproj} (see eq. 3.6), before and after track post processing are provided in figure 3.13(c). They show that the peak reprojection error densities for the center of the particle ellipsoids fall less than 10% away from the center of the image ellipses. This, together with figure 3.13(b) suggests that the reconstruction error was absorbed largely by the final reconstructed size of the particle, rather than the reprojection error. Therefore, both the normalized reprojection error and the size of the particle play a role in estimating the displacement error, ϵ_{disp}, of the particle tracking measurements. As ϵ^*_{reproj} is defined in the dewarped and normalized image space, it needs to be propagated to object space in order to estimate ϵ_{disp} which is the error in the estimation of the displacement of the particles and is elaborated subsequently in eq. 3.11. As the object to image space transformation is projective, hence linear, this error propagation is also linear and the contribution of the reprojection error to the displacement of the particle is then taken to be the average of the vector given by $\epsilon^*_{reproj}\mathbf{p}$ multiplied by a factor of $\sqrt{2}$. Therefore, the displacement uncertainty is given by:

$$\epsilon_{disp} = \sqrt{2} \cdot mean(\epsilon^*_{reproj}\mathbf{p}). \tag{3.11}$$

The displacement error estimated using the above expression for the present cases are plotted in fig. 3.13(d). For all cases the peak displacement is found to be 10 μm. The relative displacement error is treated as isotropic and therefore the peak displacement error is found to be approximately 1.4% for the axial displacement of the reconstructed particles and approximately 7% for the particle displacements transverse to the axis of the vortex.

3.6 Conclusions

In the present work simultaneous three dimensional particle tracking around a cavitating vortex and the reconstruction of its visual hull was performed. The imaging and reconstruction challenges involved in this task were identified and an imaging system was designed and implemented to provide at least a three camera cover and up to five camera cover on particles around the cavitating vortex. The implemented five camera, two beam illumination setup was calibrated using a pinhole projective mapping to take advantage of the unique properties of projective geometry in the reconstruction of particles, and the resulting calibration was assessed. The subsequent particle matching and reconstruction procedure took into account the reduced camera cover encountered by particles as they are hidden from view behind the opacity of the cavity, and the shape of the illuminated particle which was approximated by an ellipse function. The ellipse like identification of particles allowed for utilizing the ellipse-ellipsoid projective relation in order to assist particle matching. For the reconstruction of the cavity shape, a convolutional neural network was trained to detect the pixels corresponding to the cavity in the images, and the three dimensional visual hull of the cavity was reconstructed using a volume carving procedure. The reconstructed visual hull was then utilized to enhance particle matching in time in order to extend particle tracks onto the next frame. This was done by providing a particle displacement estimate using a Lamb-Oseen vortex model centered around the axis of the reconstruction visual hull of the cavity. The reconstructed particle tracks were post processed in a manner consistent with unique particle identification. Finally a detailed assessment of the measurement quality was made by estimating the quality of cavity detection by the convolutional neural network, the assessment of divergence of the mean velocity field in the wetted flow region around the cavity, the size of the reconstructed particles, the reprojection error of each of the particles and finally the error in measurement of displacement of particles around the cavity.

Overall, the convolutional neural network provided a typical detection error of 5% or less than 5% for the mIOU metric (eq. 3.7) and between of 20% for the bf-score metric (eq. 3.8), both of which were considered acceptable for the present measurement data. The preprocessed and post processed relative detection probability of the tracking algorithm was found to be in the neighborhood of 70% and 90%, respectively. For the velocimetry data, the error distribution was found to peak around 1.4% for the measured axial velocity of around 5 m/sec, and around 7% for a peak transverse velocity of around 1 m/sec.

Bibliography

[1] Adhikari, D. and Longmire, E. K. (2012). Visual hull method for tomographic piv measurement of flow around moving objects. *Exp. Fluids*, 53(4):943–964.

[2] Adrian, R. J. and Westerweel, J. (2011). *Particle image velocimetry*. Cambridge university press, Cambridge, UK.

[3] Amini, A., Reclari, M., Sano, T., Iino, M., Dreyer, M., and Farhat, M. (2019). On the physical mechanism of tip vortex cavitation hysteresis. *Exp. Fluids*, 60(7):118.

[4] Arndt, R., Pennings, P., Bosschers, J., and Van Terwisga, T. (2015). The singing vortex. *Interface focus*, 5(5):20150025.

[5] Atlar, M. (2002). The specialist committee on water quality and cavitation–final report. volume 2, Venice, Italy.

[6] Berrocal, E., Kristensson, E., Richter, M., Linne, M., and Aldén, M. (2008). Application of structured illumination for multiple scattering suppression in planar laser imaging of dense sprays. *Optics Express*, 16(22):17870–17881.

[7] Bosschers, J. (2018a). An analytical and semi-empirical model for the viscous flow around a vortex cavity. *Intl. J. Multiphase Flow*, 105:122–133.

[8] Bosschers, J. (2018b). *Propeller tip-vortex cavitation and its broadband noise*. PhD thesis, University of Twente.

[9] Bremond, N., Arora, M., Dammer, S. M., and Lohse, D. (2006). Interaction of cavitation bubbles on a wall. *Phys. Fluids*, 18(12):121505.

[10] Briançon-Marjollet, L. and Merle, L. (1996). Inception, development and noise of a tip vortex cavitation. In *21st Symp. on Naval Hydrodynamics, Trondheim, Norway*.

[11] Budwig, R. (1994). Refractive index matching methods for liquid flow investigations. *Exp. Fluids*, 17(5):350–355.

[12] Chen, L.-C., Papandreou, G., Kokkinos, I., Murphy, K., and Yuille, A. L. (2017). Deeplab: Semantic image segmentation with deep convolutional nets, atrous convolution, and fully connected crfs. *IEEE transactions on pattern analysis and machine intelligence*, 40(4):834–848.

[13] Cheng, C.-M. and Lai, S.-H. (2009). A consensus sampling technique for fast and robust model fitting. *Pattern Recognition*, 42(7):1318–1329.

[14] Cornic, P., Illoul, C., Cheminet, A., Le Besnerais, G., Champagnat, F., Le Sant, Y., and Leclaire, B. (2016). Another look at volume self-calibration: calibration and self-calibration within a pinhole model of scheimpflug cameras. *Meas. Sci. Tech.*, 27(9):094004.

[15] Cross, G. and Zisserman, A. (1998). Quadric reconstruction from dual-space geometry. In *Sixth Intl. Conf. Computer Vision (IEEE Cat. No. 98CH36271)*, pages 25–31. IEEE.

[16] Csurka, G., Larlus, D., Perronnin, F., and Meylan, F. (2013). What is a good evaluation measure for semantic segmentation?. In *BMVC*, volume 27, pages 10–5244.

[17] Deen, N. G., Westerweel, J., and Delnoij, E. (2002). Two-phase piv in bubbly flows: Status and trends. *Chem. Eng. Tech.*, 25(1):97–101.

[18] Devernay, F. and Faugeras, O. (2001). Straight lines have to be straight. *Mach. Viz. Appl.*, 13(1):14–24.

[19] Dreyer, M., Decaix, J., Münch-Alligné, C., and Farhat, M. (2014). Mind the gap: a new insight into the tip leakage vortex using stereo-piv. *Exp. Fluids*, 55(11):1–13.

[20] Duarte, C., Chapuis, L., Collin, S., Costa, D., Devassy, R., Eguiluz, V., Erbe, C., Gordon, T., Halpern, B., Harding, H., et al. (2021). The soundscape of the anthropocene ocean. *Science*, 371(6529).

[21] Elsinga, G. E., Scarano, F., Wieneke, B., and van Oudheusden, B. W. (2006). Tomographic particle image velocimetry. *Exp. Fluids*, 41(6):933–947.

[22] Fercher, A. F., Drexler, W., Hitzenberger, C. K., and Lasser, T. (2003). Optical coherence tomography-principles and applications. *Rep. Prog. Phys.*, 66(2):239.

[23] Foeth, E.-J., Van Doorne, C., Van Terwisga, T., and Wieneke, B. (2006). Time resolved piv and flow visualization of 3d sheet cavitation. *Exp. Fluids*, 40(4):503–513.

[24] Franc, J., Avellan, F., Belahadji, B., Billard, J., Briançon-Marjollet, L., Fréchou, D., Fruman, D., Karimi, A., Kueny, J., and Michel, J. (1995). *La cavitation: mécanismes physiques et aspects industriels*. Presses universitaires de Grenoble PUG.

[25] Fukushima, E. (1999). Nuclear magnetic resonance as a tool to study flow. *Ann. Rev. Fluid Mech.*, 31(1):95–123.

[26] Graftieaux, L., Michard, M., and Grosjean, N. (2001). Combining piv, pod and vortex identification algorithms for the study of unsteady turbulent swirling flows. *Meas. Sci. Tech.*, 12(9):1422.

[27] He, K., Zhang, X., Ren, S., and Sun, J. (2016). Deep residual learning for image recognition. In *Proc. IEEE Conf. Comp. Vis. Patt. Rec.*, pages 770–778.

[28] Heindel, T. J. (2011). A review of x-ray flow visualization with applications to multiphase flows. *J. Fluids Eng.*, 133(7).

[29] Jahangir, S., Wagner, E. C., Mudde, R. F., and Poelma, C. (2019). Void fraction measurements in partial cavitation regimes by x-ray computed tomography. *Intl. J. Multiphase Flow*, 120:103085.

[30] Jodai, Y. and Elsinga, G. (2016). Experimental observation of hairpin auto-generation events in a turbulent boundary layer. *J. Fluid Mech.*, 795:611–633.

[31] Jones, N. (2019). Ocean uproar: saving marine life from a barrage of noise. *Nature*, 568:158–161.

[32] Khoo, M., Venning, J., Pearce, B., and Brandner, P. (2020). Statistical aspects of tip vortex cavitation inception and desinence in a nuclei deplete flow. *Exp. Fluids*, 61:1–13.

[33] Khoo, M., Venning, J., Pearce, B., and Brandner, P. (2021). Nucleation and cavitation number effects on tip vortex cavitation dynamics and noise. *Exp. Fluids*, 62(10):1–19.

[34] Kim, S. and Lee, S.-J. (2006). Simultaneous measurement of size and velocity of microbubbles inside opaque tube using x-ray ptv technique. *J. Kor. Soc. Viz.*, 4(2):69–75.

[35] Krizhevsky, A., Sutskever, I., and Hinton, G. E. (2012). Imagenet classification with deep convolutional neural networks. *Adv. Neural. Inf. Process. Syst.*, 25:1097–1105.

[36] Lacagnina, G., Grizzi, S., Falchi, M., Di Felice, F., and Romano, G. P. (2011). Simultaneous size and velocity measurements of cavitating microbubbles using interferometric laser imaging. *Exp. Fluids*, 50(4):1153–1167.

[37] Lindken, R. and Merzkirch, W. (2002). A novel piv technique for measurements in multiphase flows and its application to two-phase bubbly flows. *Exp. Fluids*, 33(6):814–825.

[38] Linne, M. A., Paciaroni, M., Berrocal, E., and Sedarsky, D. (2009). Ballistic imaging of liquid breakup processes in dense sprays. *Proc. Combustion Institute*, 32(2):2147–2161.

[39] Lynnworth, L. and Liu, Y. (2006). Ultrasonic flowmeters: Half-century progress report, 1955–2005. *Ultrasonics*, 44:e1371–e1378.

[40] Mastikhin, I. V., Arbabi, A., Newling, B., Hamza, A., and Adair, A. (2012). Magnetic resonance imaging of velocity fields, the void fraction and gas dynamics in a cavitating liquid. *Exp. Fluids*, 52(1):95–104.

[41] Mikołajczyk, A. and Grochowski, M. (2018). Data augmentation for improving deep learning in image classification problem. In *2018 Intl. interdisciplinary PhD workshop (IIPhDW)*, pages 117–122. IEEE.

[42] Muller, K. (2023). *In Preparation.* PhD thesis, Delft University of Technology.

[43] Muller, K., Hemelrijk, C., Westerweel, J., and Tam, D. (2020). Calibration of multiple cameras for large-scale experiments using a freely moving calibration target. *Exp. Fluids*, 61(1):1–12.

[44] Nanda, S., Westerweel, J., van Terwisga, T., and Elsinga, G. (2022). Mechanisms for diffusion-driven growth of cavitating wing-tip vortices. *Intl. J. Multiphase Flow*, 156:104146.

[45] Peng, X., Xu, L., Song, M., and Cao, Y. (2015). Vortex singing in tip vortex cavitation under the effect of water quality. In *J. Phys.: Conference Series*, volume 656, page 012185. IOP Publishing.

[46] Pennings, P. (2016). *Dynamics of vortex cavitation.* PhD thesis, Delft University of Technology.

[47] Pennings, P., Bosschers, J., Westerweel, J., and Van Terwisga, T. (2015a). Dynamics of isolated vortex cavitation. *J. Fluid Mech.*, 778:288–313.

[48] Pennings, P., Westerweel, J., and Van Terwisga, T. (2015b). Flow field measurement around vortex cavitation. *Exp. Fluids*, 56(11):1–13.

[49] Pennings, P., Westerweel, J., and van Terwisga, T. (2016). Cavitation tunnel analysis of radiated sound from the resonance of a propeller tip vortex cavity. *Intl. J. Multiphase Flow*, 83:1–11.

[50] Poelma, C. (2020). Measurement in opaque flows: a review of measurement techniques for dispersed multiphase flows. *Acta Mechanica*, 231:2089–2111.

[51] Poelma, C., Mari, J., Foin, N., Tang, M.-X., Krams, R., Caro, C., Weinberg, P., and Westerweel, J. (2011). 3d flow reconstruction using ultrasound piv. *Exp. Fluids*, 50(4):777–785.

[52] Poelma, C., Westerweel, J., and Ooms, G. (2006). Turbulence statistics from optical whole-field measurements in particle-laden turbulence. *Exp. Fluids*, 40(3):347–363.

[53] Rojas, R. (1996). The backpropagation algorithm. In *Neural networks*, pages 149–182. Springer.

[54] Sahu, S., Manish, M., and Hardalupas, Y. (2018). Two-phase characterization for turbulent dispersion of sprays: a review of optical techniques. *Droplets and Sprays*, pages 247–273.

[55] Schanz, D., Gesemann, S., and Schröder, A. (2016). Shake-the-box: Lagrangian particle tracking at high particle image densities. *Exp. Fluids*, 57(5):1–27.

[56] Soloff, S. M., Adrian, R. J., and Liu, Z.-C. (1997). Distortion compensation for generalized stereoscopic particle image velocimetry. *Meas. Sci. Tech.*, 8(12):1441.

[57] Sudre, C. H., Li, W., Vercauteren, T., Ourselin, S., and Cardoso, M. J. (2017). Generalised dice overlap as a deep learning loss function for highly unbalanced segmentations. In *Deep learning in medical image analysis and multimodal learning for clinical decision support*, pages 240–248. Springer.

[58] Tan, S., Salibindla, A., Masuk, A. U. M., and Ni, R. (2020). Introducing openlpt: new method of removing ghost particles and high-concentration particle shadow tracking. *Exp. Fluids*, 61(2):1–16.

[59] Welch, P. (1967). The use of fast fourier transform for the estimation of power spectra: a method based on time averaging over short, modified periodograms. *IEEE Transactions on Audio and Electroacoustics*, 15(2):70–73.

[60] Westerweel, J. and Scarano, F. (2005). Universal outlier detection for piv data. *Exp. Fluids*, 39(6):1096–1100.

[61] Wiederseiner, S., Andreini, N., Epely-Chauvin, G., and Ancey, C. (2011). Refractive-index and density matching in concentrated particle suspensions: a review. *Exp. Fluids*, 50(5):1183–1206.

[62] Wieneke, B. (2008). Volume self-calibration for 3d particle image velocimetry. *Exp. Fluids*, 45(4):549–556.

[63] Wright, S. F., Zadrazil, I., and Markides, C. N. (2017). A review of solid–fluid selection options for optical-based measurements in single-phase liquid, two-phase liquid–liquid and multiphase solid–liquid flows. *Exp. Fluids*, 58(9):1–39.

[64] Zisserman, A. and Hartley, R. (2001). *Multiple View Geometry in Computer Vision*. Cambridge University Press, Cambridge, UK.

4

Influence of Diffusion Driven Growth on the Kinematics of Wing-Tip Vortex Cavities[1]

Analysing the velocity field around a cavitating vortex experimentally is difficult due to opacity caused by the cavity, and its wandering behavior. In this chapter, the measurement data for mean flow velocities around the vortex cavity obtained from chapter 3 are analysed. The general influence of the opacity towards the binning process is first studied, and subsequently, vortex models are fitted to the measurement data. The fits are compared generally against the measurement data and their specific parameter magnitudes are compared against those found in literature. Four models are compared against experimental data: (1) the vortex model by Proctor [31], (2) both the analytical and the semi-empirical model by Bosschers [9], and finally (3) the vortex model by Choi and Ceccio [13]. It was found that the semi-empirical vortex model describes the behavior of a cavitating vortex remarkably well, with the vortex azimuthal profiles being nearly identical for two different cavity sizes at nearly the same flow conditions. This leads to the hypothesis that the vortex profile does not change significantly during the development of the cavity's size. At the same time, the behavior of the model by Choi & Ceccio showed an acceleration in the azimuthal velocity of the vortex next to the interface, suggesting that the measurement technique could have picked up microbubble velocities close to the interface. Based on these observations, some suggestions to improve experimental practices are given.

[1]This chapter is being considered for publication as Nanda, S., Muller K., Westerweel, J., van Terwisga, T., & Elsinga, G. (2023). The Kinematics of Developing Wing-Tip Vortex Cavities using Simultaneous 3D Velocimetry and Shape Reconstruction, International Journal of Multiphase Flows.

4.1 Introduction

Vortex cavitation occurs in the marine environment when lifting bodies travel beyond a critical velocity, causing the pressure of the fluid in the low-pressure regions of wing-tip vortices to approach vapor pressure, which causes a phase change of the fluid medium. They are found most frequently in marine propeller flows, as helecoidal cavity tubes originating from the blade tip regions of the propeller. Vortex cavitation is thought to be responsible for broadband hull pressure fluctuations [34] which introduce a fatigue load to the ship hull structure, and is also known to be disruptive to the marine habitat [15] through characteristically tonal sound producing mechanisms [5, 18].

The kinematics of cavitating vortices is a topic of current interest and an extensive survey of literature has been produced by various workers (see for example [9]). With respect to cavitation, the study of vortex kinematics is usually done for conditions found at inception [12, 13, 21–24, 26], and fewer studies have considered the conditions of developed cavitation [9, 14, 27]. Developed cavitation is especially important for understanding the vibrations of the cavity surface, which are a component of the underwater radiated noise (URN) from a ship [11], and broadband hull pressure fluctuations (HPF) acting on the hull-structure of the ship [35].

Up until now, it has been shown experimentally [14, 30] that in cavitating conditions, the angular velocity of the wetted flow next to the cavity interface reduces in velocity with increasing cavity size, when compared to fully wetted, or non-cavitating conditions. This is also reflected in the study by Choi & Ceccio [13], who proposed a heuristic vortex model to describe the reducing flow velocity near the cavity interface as it increases in size. A point of contention then occurs when the vortex cavity increases in radius without an increase in either the Reynolds number of the flow, or the angle of attack of the hydrofoil, or the reduction of ambient pressure in the flow facility. This occurs when the vortex cavity naturally develops in size by either ingesting microbubbles in the flow (see works by [12, 26, 33]), or grows in size due to diffusion of dissolved gases present in the flow (see [2, 10], and as discussed extensively in chapter 2 of this thesis), together characterized as water-quality effects. In such conditions, the cavitation is referred to as *gaseous* cavitation, instead of *vaporous* cavitation, where the rarefied medium inside the cavity comprises of a mixture of air and water vapor, and the pressure inside the cavity is higher than vapor pressure. Under these conditions, phenomena such as cavitation hysteresis [19, 20] are observed, where the cavitation survives even after inception conditions are eased in the flow facility. During the period when the cavitation develops in size, it is possible to consider that in order to conserve angular momentum during the development stage, the flow velocity next to the cavity interface may increase, rather than decrease, as the vapor-liquid interface moves radially outwards. At the same time, the contribution to the total angular momentum of the vortex in the regions close to the vortex center is low, therefore the expected change in the vortex velocity profile may not be significant enough to measure using currently available techniques. Experimental data is lacking in clarifying between either of these two scenarios.

The measurement of vortex kinematics next to the cavity interface has inherent difficulties which increase the uncertainty of the flow measurements in that region. Among these measurement challenges is the characteristic wandering behavior of the vortex axis due to the dynamics of the vortex [28], the wandering caused by external turbulence in the incom-

ing flow [30, 36], the periodic shedding of the wake of the wing that generates the vortex [29], and among other reasons, the helecoidal shape of the vortex cavity when generated using a model scale propeller. The main issue with the motion of the vortex-axis and the vibrations of the cavity is that it causes a smearing of the measured velocity profile around a cavity when time-averaged, snapshot based optical imaging techniques are employed, both by single point measurement techniques like Laser Doppler Velocimetry/Anemometry (LDV/LDA) and planar/stereoscopic Particle Image Velocimetry (PIV). Three dimensional measurements are known to be even more notorious for the difficulty in their application to cavitating flows due to the presence of opacities (see [1] for application of tomographic PIV [16] around opaque objects), and to the knowledge of the authors, there exist no known experimental work on three-dimensional velocimetry measurements around a developed vortex cavity, either using Tomographic PIV (TOMO-PIV) [16] or by Particle Tracking Velocimetry [32]. As mentioned previously, these measurement techniques are challenged by optical obstructions caused by the cavity, which introduces effects like specular reflections, reduced camera cover and high vortex angular velocity in regions close to the cavity, all of which were tackled in the measurement and reconstruction approach described in the previous chapter (see chapter 3).

The main aim of this work is to analyse the measurement data obtained in the previous chapter (chapter 3), and compare the measurements against vortex models of a cavitating vortex in order to assess the flow conditions around a developing vortex cavity that develops purely due to water quality effects. To this end, the outline of this chapter is as follows: §4.2 describes the vortex models tested in this work, §4.3 describes the measurement test-cases and the data reduction carried out in this work, §4.4 presents our results and discussions and §4.5 concludes this work.

4.2 Background on Kinematic Models for Cavitating Vortices

4.2.1 The Lamb-Oseen Vortex Model

Vortex models for wing-tip vortices are usually variants of the steady Lamb-Oseen vortex model [25], which describes the tangential velocity, u_θ, as a function of the radial distance, r, from the centre of an infinite line vortex as a solution to the Navier-Stokes equation, and is given as follows:

$$\begin{aligned} u_\theta &= \frac{\Gamma_\infty}{2\pi r}\left[1 - exp\left(\alpha\frac{r^2}{r_v^2}\right)\right], \\ \frac{u_\theta^2}{r} &= \frac{1}{\rho_l}\frac{\partial p}{\partial r}, \end{aligned} \tag{4.1}$$

where Γ_∞ is the ambient circulation strength of the vortex, α is a constant equal to 1.2526[2], r_v is the radius of the viscous core of the vortex, ρ_l is the density of the liquid phase, and p is the pressure field around the vortex. The Lamb-Oseen expression represents an

[2]The constant is needed to ensure that the maximum tangential velocity is at the viscous core boundary

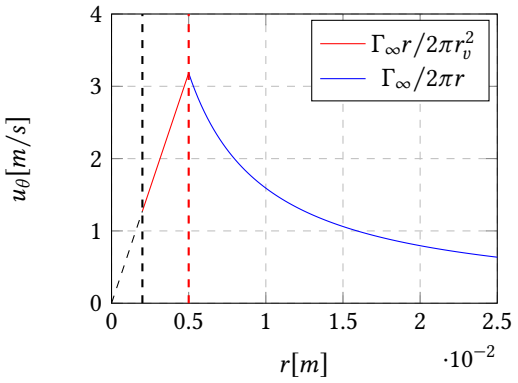

Figure 4.1: Example profile for the Arndt and Keller model, with Γ_∞ at 0.1 m/s^2, r_v of 5 mm shown by the red vertical line, and r_c of 2 mm as shown by the black vertical line. u_θ is presented in m/s and r is presented in m.

isolated ideal vortex, and is not generally applicable to wing-tip vortices, specially near the tip-region of the flow, where secondary flows originating from the wake of the wing are dominant. In these regions, semi-empirical variants such as the Proctor vortex model [31] and the Winckelman's vortex model [17] were developed to account for the presence of the wake of the wing, typically needing extra fitting parameters to tune the vortex model to the flow. While these modifications are successful in wetted, or non-cavitating flows, they are very limited in describing the flow-field around a cavitating vortex [29], particularly in the region inside its viscous core. For cavitating vortices, very few vortex models have been proposed [3, 7, 13], and experimental data is generally lacking due to the difficulty in measuring the flow-field near the vapor-liquid interface. Some of these models will be elaborated in the coming discussions.

4.2.2 Vortex Model By Arndt and Keller

For modelling cavitating vortices at inception conditions, Keller and Arndt [4] proposed a simple but instructive vortex model based on the Rankine vortex, which models the tangential velocity around a cavitating vortex as the following piecewise function:

$$u_\theta = \begin{cases} \frac{\Gamma_\infty r}{2\pi r_v^2} & r_c \leq r \leq r_v; \\ \frac{\Gamma_\infty}{2\pi r} & r > r_v, \end{cases}$$

where r_c is the cavity radius. They argue that, as the vaporous core of the cavity has a much smaller total angular momentum in comparison to that in the wetted flow, the total angular momentum of the wetted flow in cavitating conditions is approximately equal to that in non-cavitating conditions. This requires the viscous core radius to increase as the radius of the cavity increases, but not proportionally as implied by Bosschers [7]. This is instead given by the following relationship:

$$\left(\frac{r_v^{nc}}{r_v}\right)^2 = 1 + \left(\frac{r_c}{r_v}\right)^4, \tag{4.2}$$

where r_v^{nc} is the viscous core radius of the vortex in non-cavitating conditions.

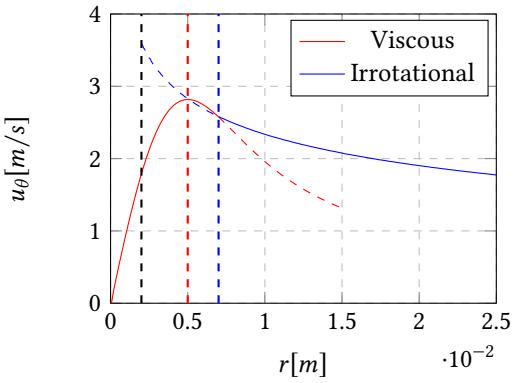

Figure 4.2: Example profile for Proctor's vortex model (eq. 4.3 and eq. 4.4), with Γ_∞ at 0.2 m/s^2 on the viscous core formulation, r_v of 5 mm shown by the red vertical line, and r_c of 2 mm as shown by the black vertical line. The blue dashed line corresponds to the location $r = 1.4r_v$ (dashed blue vertical line) where both the irrotational and the viscous formulations need to be matched. u_θ is presented in m/s and r is presented in m.

4.2.3 Proctor's Vortex Model

Although the Proctor Vortex model [31] was developed for non-cavitating wing-tip vortices, it has also been applied to cavitating vortices by Pennings et al. [27]. The vortex model was developed to with additional parameters relative to the Lamb-Oseen formulation in order to account for the wake of the wing. The model is a discontinuous formulation consisting of a purely irrotational part and a part containing the viscous core radius. The irrotational part is given as:

$$u_\theta = \frac{\Gamma_\infty}{2\pi r}(1 - exp(-\beta(r/B)^{0.75})), \tag{4.3}$$

where B and β are constants. The viscous core region is modelled as:

$$\begin{aligned} u_\theta = 1.0939\frac{\Gamma_\infty}{2\pi r}\left\{1 - exp\left(-\beta\left(1.4\frac{r_v}{B}\right)^{0.75}\right)\right\}... \\ ...\left\{1 - exp\left(-\alpha\left(\frac{x}{r_v}\right)^2\right)\right\}. \end{aligned} \tag{4.4}$$

The above formulations have been tested in the work of Pennings et al. and it was found that only the irrotational component was able to represent cavitating vortices. While this is a drawback, the extra parameters may be applicable for modelling the viscous core of the vortex in the far wake region of the vortex, where the wake effects of the foil are typically not observed.

4.2.4 Bosschers Analytical Model For Infinite Cavitating Vortices

While it is generally agreed that the flow outside the viscous core is essentially similar to a non-cavitating vortex [9], therefore irrotational, the kind of boundary condition assumed at the vapor-liquid interface is what distinguishes one vortex model from the other. In the analytical vortex-model of Bosschers [7], the shear stress at the interface of the cavity is considered to be zero. The vortex model is then given by the following expression:

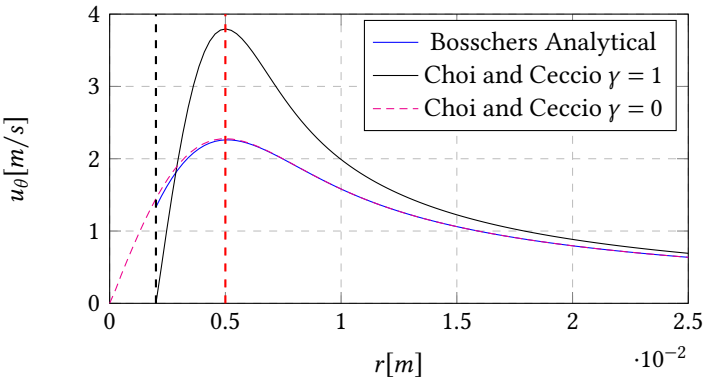

Figure 4.3: Example profile for the analytical vortex model by Bosschers (4.5), with Γ_∞ at 0.1 m/s^2 on the viscous core formulation, r_v of 5 mm shown by the red vertical line, and r_c of 2 mm as shown by the black vertical line. This gives a corresponding β value of 1.0179. Also included with similar parameters is the vortex model of Choi and Ceccio (eq. 4.10) with the γ parameter set to 0 (Lamb-Oseen formulation) and 1. u_θ is presented in m/s and r is presented in m.

$$u_\theta = \frac{\Gamma_\infty}{2\pi r}\left\{1-\beta exp\left(-\alpha\frac{r^2}{r_v^2}\right)\right\}, \tag{4.5}$$

$$\beta = \frac{r_v^2}{r_v^2+\alpha r_c^2} exp(\alpha r_c^2/r_v^2), \tag{4.6}$$

where r_c is the radius of the cavity, and β is derived from the assumption of no shear stresses at the cavity interface. If β is time-invariant, then it follows that r_c is proportional to r_v in time.

4.2.5 Bosschers Semi-Empirical Model for Cavitating Vortices

Similar to the way the Proctor vortex and the Winckelman's vortex account for wake effects of the wing, semi-empirical models for the cavitating vortex have also been proposed. Bosschers [9] proposed a semi-empirical model for the tangential velocity of a cavitating vortex, which is given by the following expression:

$$\begin{aligned} u_\theta = \frac{\Gamma_\infty}{2\pi r}&\left\{1-\overline{\alpha} exp\left[-\zeta_1\left(\frac{r}{B}\right)^p\right]\right\}... \\ &...\left\{1-\beta exp\left[-\zeta_2\frac{r^q-r_c^q}{r_v^q}\right]\right\}, \end{aligned} \tag{4.7}$$

where B, ζ_1, ζ_2, p and q are free-parameters of the vortex model. β is derived from the assumption of zero shear-stresses at the cavity interface, and given by the following expression:

$$\beta = \frac{2(1-\hat{\alpha})B^p r_v^q - \hat{\alpha}\zeta_1 p r_c^p r_v^q}{2(1-\hat{\alpha})B^p r_v^q - \hat{\alpha}\zeta_1 p r_c^p r_v^q + (1-\hat{\alpha})B^p q\zeta_2 r_c^q}, \tag{4.8}$$

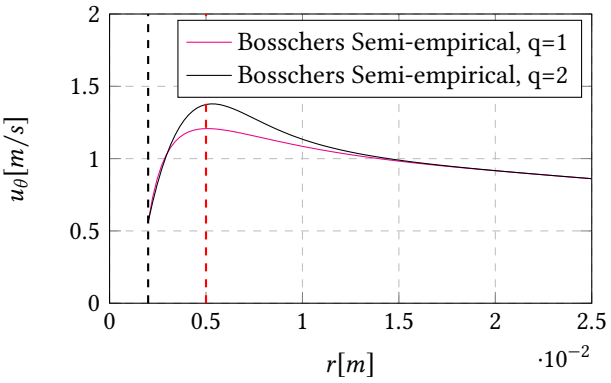

Figure 4.4: Example profile for the semi-empirical vortex model by Bosschers (4.5), with Γ_∞ at 0.2 m/s^2 on the viscous core formulation, r_v of 5 mm shown by the red vertical line, and r_c of 2 mm as shown by the black vertical line. Further parameters include $p = 1.6197$, $\overline{\alpha} = 0.7870$, $\beta = 0.8429$, $\zeta_1 = 49.75$, and $\zeta_2 = 1.8475$. u_θ is presented in m/s and r is presented in m.

where, $\overline{\alpha}$ is estimated from a free-parameter $\hat{\alpha}$ as follows:

$$\overline{\alpha} = \hat{\alpha} exp\Big[-\zeta_1\Big(\frac{r_c}{B}\Big)^p\Big]. \tag{4.9}$$

This semi-empirical model has been fitted [8] to stereoscopic PIV data found in [29], and will be used for comparison with the measurements of this work.

4.2.6 Vortex Model of Choi and Ceccio

In contrast to the ideas of Bosschers, the heuristically derived vortex model of Choi and Ceccio [13] keeps the shear-stress boundary condition on the cavity interface flexible by the use of a free parameter, γ. This vortex model is given by the following expression:

$$u_\theta = \frac{\Gamma_\infty}{2\pi(r-\gamma r_c)}\Big\{1-exp\Big(-\alpha\Big[\frac{r-\gamma r_c}{r_v-\gamma r_c}\Big]^2\Big)\Big\}. \tag{4.10}$$

The term γ allows modifying the velocity of the flow at the interface, with a value of 0 describing a steady Lamb-Oseen vortex, and a value of 1 giving zero tangential velocity at the interface. Choi and Ceccio have found that for cavitating vortices at inception conditions, the γ parameter is approximately between 0 and 0.6, meaning that the tangential velocity of the interface reduces as one increases its size.

4.3 Test Cases and Data Reduction

As described in the previous chapter (see chapter 3), three dimensional, time resolved velocimetry data was obtained using Particle Tracking Velocimetry (PTV) for a cavitating vortex generated by a stationary NACA 66_2-415 elliptical half-wing at 9 degrees incidence to the flow, with a half span of 15 cm and a root chord, C_0, of 12.56 cm. The measurements were performed in a region five chord lengths downstream from the tip, and a total axial distance of 3 cm around the center of the measurement volume was processed for producing the mean velocity profiles discussed in the subsequent section 4.4. As motivated in the earlier chapter, the measurement region was chosen for two main purposes: 1) to accommodate the optical measurement equipment, and 2) that the viscous roll up of the wake of the hydrofoil can be assumed to be completed this far downstream of the tip. Furthermore, the

Properties	Units	Case 1	Case 2	Bosschers 1 [9]	Bosschers 2 [9]	Pennings 1 [27]	Pennings 2 [27]
C_L	[-]	0.66	0.66	0.58	0.58	0.66	0.66
N_{IN}^{avg}	[-]	3240	3330	-	-	-	-
$\bar{r}_c$	[mm]	0.34	2.10	0.56	1.22	2.6	2.4
$100\bar{r}_c/C_0$	[-]	0.27	1.67	0.52	1.22	2.07	1.91
U_∞	[m/s]	4.9	5.1	6.8	6.8	6.8	6.8
p_∞	[kPa]	24.5	23.7	55.1	31.1		
Re_{C_0}	[$\times 10^5$]	6.72	9.4	9.3	9.2	9.2	
σ	[-]	1.79	1.59	2.3	1.26	1.79	1.59
c_∞/c_{sat}	[-]	1.45	1.5				
z/C_0	[-]	5-5.24	5-5.24	1.14	1.14	1.14	1.14
Γ_∞	[m^2/s]	0.18	0.2	0.19	0.19	0.16	0.17
$\bar{r}_v$	[mm]	6.5	6.9	1.3	2.5	1	1

Table 4.1: Tabulation of the test-cases used in this work. N_{IN}^{avg} is the average inlier particles of the tracking data per timestep. U_∞ is the magnitude of the freestream velocity, $Re_{C_0} = U_\infty C_0/\nu$ is the chord Reynolds number for a root chord length (C_0) of 12.56 cm and kinematic viscosity ν, σ is the cavitation number given by $(p_\infty - p_{vap})/(0.5\rho U_\infty^2)$ for p_{vap} being the vapor pressure of water and ρ being the water density, c_∞ is the measured dissolved gas saturation at atmospheric pressure and c_{sat} is the saturated dissolved gas concentration at p_∞ using a Henry's constant of 0.223×10^{-6} kg/m^3Pa. Γ_∞ is the ambient circulation strength, and $\bar{r}_v$ is the average viscous core radius of the vortex, both measured at the downstream location z/C_0 from the tip, where the root chord length has been used to normalize the distance from the wing-tip in tunnel reference frame. These were inferred from model fits as described later in §4.4. Data from both works by Pennings [27] and Bosschers [9] are shown. While the data Bosschers is not directly considered, as it concerns only the region near the tip, the fit coefficients estimated from this work are compared against that from our data in §4.4.3. The data by Pennings is shown, and considered for comparison due to the presence of data at our measurement location downstream of the tip. The viscous core radius shown in this table from this dataset corresponds to the region near the tip, at z/C_0 of 1.14.

growth of the the viscous core of the vortex reduces downstream from the tip as observed in the work of [27]. This means that the viscous core does not vary much within the measurement volume considered in this work.

In order to understand the influence of the size of the cavity on the vortex azimuthal velocity profile, two cavity sizes were chosen, one where the cavity radius was small compared to its viscous core size ($r_c/r_v \approx \mathcal{O}(10^{-1})$)) and one where the viscous core size is comparable compared to the developed size of the cavity, i.e., $r_c/r_v \approx \mathcal{O}(10^0)$. Details of the test cases considered in this work are described in table 4.1 and labeled as case 1 and case 2. A total of 1000 timesteps were reconstructed for both test cases, with Δt being 2×10^{-4} seconds, corresponding to an acquisition frame rate of 5000 Hz. The quality of the velocimetry was previously estimated, and the uncertainty in the measured velocity signal was 1.4% in the direction of the vortex axis and 7% in the component tangential to the vortex axis. Some particulars of the cavitating vortex could not be measured, such as the cavitation number at inception and the ambient circulation strength. Empirical work found in literature and described subsequently was used to fill the missing information. To this end, an expression for the ambient circulation strength of the vortex was be taken from literature [6]:

$$\Gamma_\infty = \frac{\pi}{8} C_0 C_L U_\infty. \tag{4.11}$$

In the analysis of the vortex models, the viscous core radius has been kept as a free-parameter because estimating the viscous core radius from measurement data would

lead to biases due to a limited vector resolution, and that the measurements also contain experimental uncertainty described in the previous chapter (chapter 3). In order to compare the estimated viscous core radius with that of prior data for the location 5.5 chord lengths downstream from the tip, estimates were considered from the experimental data fit of Pennings [29] which is given as follows:

$$r_v \approx B0.37CRe_C^{-0.2}, \tag{4.12}$$

where B depends on the distance downstream from the tip and varies between 0.3 and 0.5. In the current work, this is equal to 0.5 for the data presented in this work.

Also provided in table 4.1 are data from prior work for comparison, using the same elliptical hydrofoil and in the same cavitation tunnel, however, with differing experimental particulars. These cases are based around the measurement data by Pennings et al. [27]. The data reported by Pennings et al. [27], named Pennings 1 and Pennings 2, contains information at the same angle of attack and cavitation numbers as in case 1 and case 2 of the current work respectively, but has a very similar cavity radius. This comes from the fact that in the measurements of Pennings, a buffer time is provided during the measurement campaign, where the cavity grows to a predefined size starting from inception and prior to recording measurements. Secondly, in the table, the viscous core radius is provided at a value of 1.14 chord lengths downstream of the tip, where a lot of the vortex model fitting was performed. This is different from our experiments because the cavity radii are not the same between cases 1 and 2 from the present measurements, and that the experimental data is taken from a region more than 5 chord lengths downstream from the tip. The study from Bosschers [9] is also shown, which considers a different, shallower angle of attack (at 5 degrees incidence to the flow), where most of the vortex model fitting was performed.

Because of the differences in the experimental particulars, it is not possible to compare measured vortex model profiles between the present work and those in table 4.1. Therefore, a comparison is made between the fitted vortex model parameters. This is later performed in §4.4.3.

4.4 Results and Discussions

The details of the measurement approach and data reduction were previously discussed extensively in chapter 3. For convenience, some relevant details regarding the data processing are repeated first. The velocimetry data was obtained from a volumetric region covering 6 centimeters beginning from 5 chord lengths downstream of the tip of the hydrofoil. The centerline of the reconstructed visual hull of the vortex cavity was extracted and a linear fit was applied to estimate the axis of the vortex for each timestep. This was then used to center the measured particle displacements to the vortex axis. The flow velocities from the centered particle tracks were binned radially with a vector spacing of 0.5 mm, and an averaged flow field was estimated after accumulating the centered displacement measurements over a time period of 1000 timesteps, totalling 0.2 seconds of physical time. The measured particle displacements cover a region all around the cavity, however, the regions of low camera cover are typically regions where particle matching was found to be reduced in density. The causes of this is attributed to issues with particle matching near the cavity interface due to the existence of less than 3 focal zones around the cavity (see

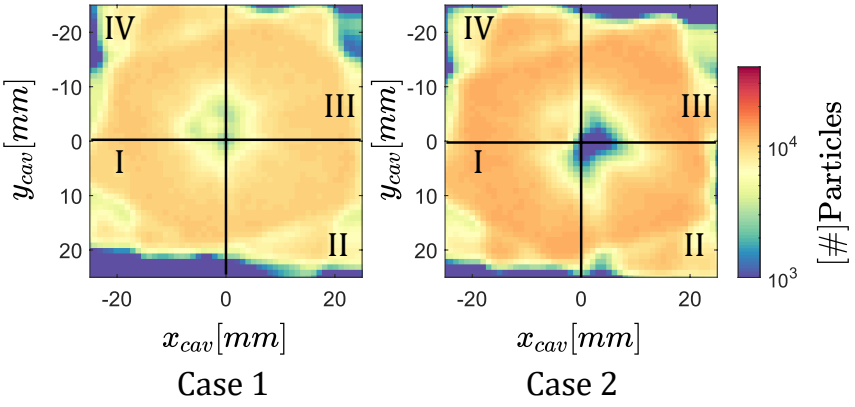

Figure 4.5: Axially accumulated, case-wise particle displacement bin counts over 1000 timesteps using 0.5 mm bin width in both dimensions. Both densities were obtained after centering the vector velocity profiles using centering approaches described in §4.4 such that the position of the cavity is at the origin.

figure 3.1 and the accompanying discussion). This is reflected in the particle density plots of figures 4.6 and 4.7 which are discussed below. The measured particle density plots are better seen in figure 4.5 where the particle densities have been summed over in the axial direction.

The discussion of results is done in the following manner. Firstly, the sensitivity of the azimuthal component towards the binning process is studied. This is done by conditionally binning the centered particle displacements, first by binning the particle displacements based on their focality (§4.4.1), and second by binning them based on their location in the imaging volume, in quadrants (§4.4.2). Both binning procedures essentially highlight sensitivities induced by the varying camera cover of the particles caused by the opacity of the cavity, and guide the selection of regions for comparing the azimuthal component of the velocity to the vortex models. Finally a comparison of parameters of the vortex models fitted to the averaged azimuthal velocity profile is done in §4.4.3.

The vortex models discussed in §4.2 are assessed by parameter fitting to the averaged azimuthal velocity profiles of the measured cavitating vortices. As the binning was performed in a cavity centered coordinate system, it can be fairly assumed that the influence of vortex wandering was essentially eliminated. Not all the models discussed in §4.2 were studied. The Proctor vortex model in equations 4.3 and 4.4 is compared against the experimental data to check if the irrotational formulation indeed applies as was observed by Pennings [27] and if the rotational formulation is applicable to the viscous region of the vortex. For the latter comparison, it is expected that the model would be applicable due to extra parameters present in the model. It is useful to note that this model is being applied outside its applicable range, therefore the comparison can lead to similar observations as previously reported by Pennings. Both models introduced by Bosschers, i.e., the analytical model (eq. 4.5) and the semi-empirical formulation (eq. 4.7) are fitted to the experimental data. In this case, the fitted parameters are qualitatively compared against that estimated by Bosschers [9] based on data by Pennings [27]. The vortex model of Choi and Ceccio (eq. 4.10) was also fitted to the averaged azimuthal velocity of the vortices.

In the vortex model comparisons presented subsequently in §4.4.3, the vortex models considered above are not directly fitted to the entire measured radial region. Considerations were made towards the range where each vortex model would be best applicable. These considerations are elaborated in the discussions in §4.4.3. In the following discussions, the sensitivity of the vortex velocity profiles to conditional binning based on camera-cover and quadrant around the vortex-axis are elaborated.

4.4.1 Sensitivity of Vortex Profile to Particle Camera Cover

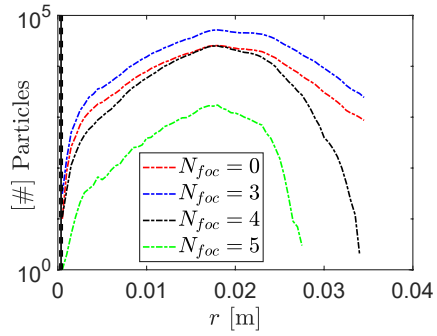

(a) Case 1

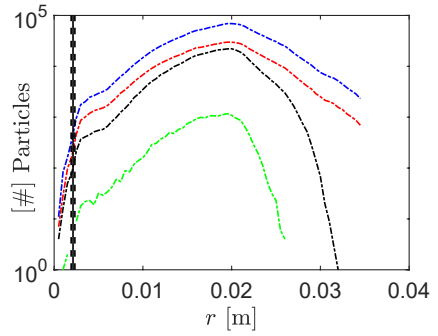

(b) Case 2

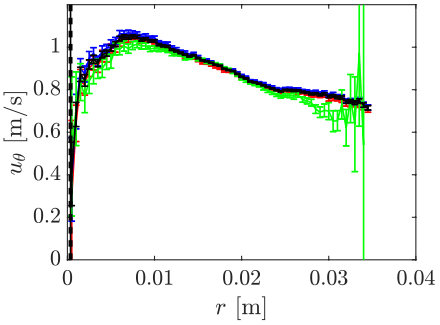

(c) Case 1

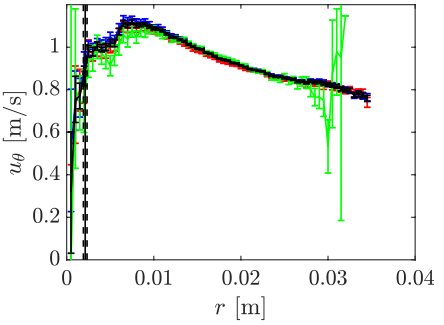

(d) Case 2

Figure 4.6: Plots showing the sensitivity of the averaged azimuthal velocity when considering a specific camera cover value, N_{foc}. In these plots, data from all four quadrants are considered. Figures a and b show the distribution of particle counts considered for each velocity profile shown in figures c and d. Also included is data from reconstructions considering zero-focal particles, i.e., particles that are used to stitch two tracks together while performing the track reconstruction. The error bars in figures c and d are the statistical uncertainty based on a 95% confidence bound of the velocity magnitude.

The camera cover over a particle is the total number of individual particle images from correspondence set across multiple views that were used to triangulate the position of the particle in 3D in a least-squares sense. With an increase in camera cover, the uncertainty over a particle's position reduces, but as has been discussed previously in §3, the opacity

caused by the vapor-liquid boundary of the cavity means a particle cannot be tracked by all cameras as it moves around the cavity (see figure 3.1). This is why a variable particle camera cover approach was developed to measure particle displacements around the cavity. Figure 4.6 shows profiles of the azimuthal component of the vortex when binned based on camera cover. Therefore, the variation includes the effect induced by opacity of the cavity, which makes tracking difficult for 5-focal reconstructions. In the binning process, all quadrants are considered, therefore the results indicate how good one could estimate the azimuthal component if the data would be found in only a few quadrants, which is the case for 5-focal reconstructions particularly.

The particle density plots in the top figures of figure 4.6 show that the densities are strongly dependant on camera cover, however, when their conditionally binned velocity profiles are considered (bottom figures of fig. 4.6), the velocity profiles are found to be invariant of the camera cover.

4.4.2 Sensitivity of Vortex Profile to Data Quadrant

The camera cover over a particle is also dependent on the angular position of the particle around the cavity. This is due to the combination shadows cast by the light that travels in the direction of the principle axis of the cameras, as seen in figure 3.1. To study the effect of these zones of varying camera cover, the binning has been done based on quadrants around the cavity, disregarding the number of cameras used to reconstruct the position of each particle in that quadrant. The conditional binning in this case is done to highlight velocity profile differences from quadrant to quadrant. With this in mind, it is useful to note that in the case of the fully developed cavity (case 2 of table 4.1), the presence of zones of variable camera cover are well attributed to the inability to join particle tracks as particle disappear behind the cavity and enter a zone of low camera cover. However, for case 1, the size of the cavity is negligible compared to the viscous core radius, and yet one observes zones of reduced reconstructed particle density in regions corresponding to quadrants I and IV of figure 4.5. The causes of this is unclear, although, one could attribute it to the track post-processing step (see §3.3.2.6) where duplicate particle tracks are removed if more than one particle reconstructed in 3D reprojects onto a particle in the image, with the track eliminated being the shorter track.

The binned displacement densities shown in the top figures of figure 4.7 show that the particle densities are mostly identical in the region away from the viscous core, i.e., in the irrotational region of the vortex. Most differences arise in the region closer to the interface, and are most pronounced in the well developed cavity case, where one can clearly see the influence of reducing camera cover. In contrast to the velocity profile conditioned based on focality, there are differences introduced when the binning is performed quadrant wise. Initially, the differences were expected to be more pronounced for case 2, where the cavity radius is larger, and a clear dark zone is visible. Surprisingly however, the velocity profiles are found to be relatively similar for cases 1 and 2. Differences due to quadrant wise conditioning largely arise in the profiles of case 1, specifically in quadrant IV, where a zone of low binned particle displacement density is observed in figure 4.7. These differences may be attributed to a particular N_{foc} value being larger in a certain quadrant or sub regions of a quadrant.

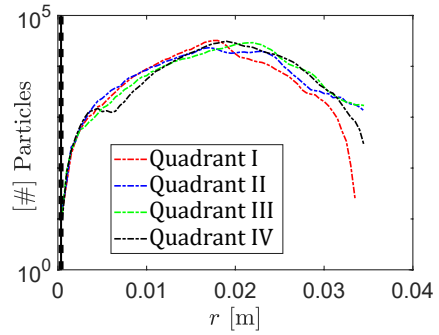

(a) Case 1

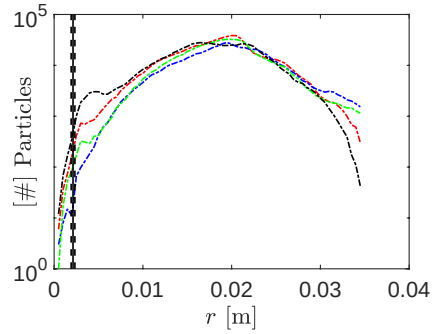

(b) Case 2

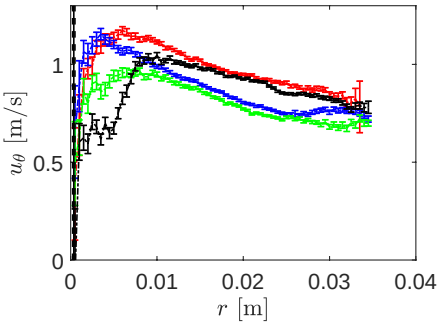

(c) Case 1

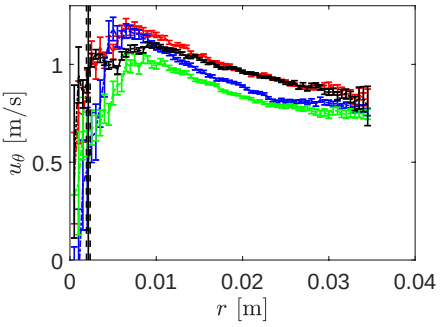

(d) Case 2

Figure 4.7: Plots showing the sensitivity of the averaged azimuthal velocity component of the vortex cavity conditioned on a specific quadrant. In these plots, data from all focalities are considered. The quadrant is decided in an anticlockwise manner, with the positive x-axis of figure 4.5 taken to be zero degrees. Figures a and b show the distribution of particle counts considered for each velocity profile shown in figures c and d. The error bars in figures c and d are the statistical uncertainty specified as a 95% confidence bound of the velocity magnitude.

4.4.3 Comparison of Azimuthal Velocity Profile with Vortex Models

As discussed in the preceding section, the vector velocity components are averaged considering data from all focalities and quadrants. The parameter fitting of the vortex models to the measurement data was done in a manner that preserves the principle predictive feature of the model. For the Proctors vortex model in equations 4.3 and 4.4, the parameters were tuned so that the irrotational model represented the irrotational region well, in line with the observations of Pennings et al. [27], while the viscous core model was tuned to roughly give the same observed viscous core radius as the data. The fitting was performed simultaneously and parameters that were shared between both formulations were kept constant between the models once a magnitude had been estimated. The analytical cavitating vortex model of Bosschers (eq. 4.5) was fitted to only the far reaches of the data, i.e., $r/r_v \geq 2$ because it was unable to account for the viscous core profile. Therefore only the ambient

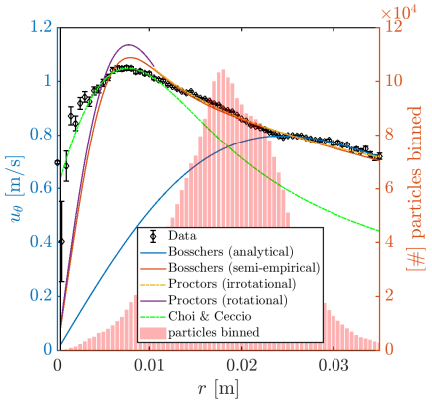

(a) Case 1, conditionally averaged azimuthal velocity.

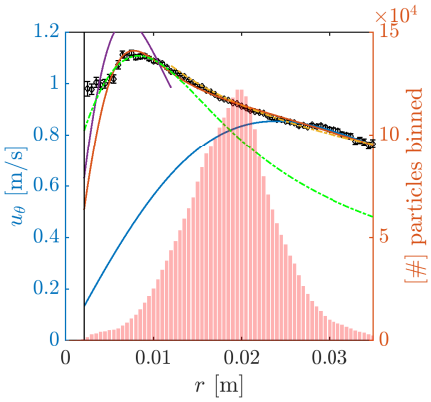

(b) Case 2, conditionally averaged azimuthal velocity.

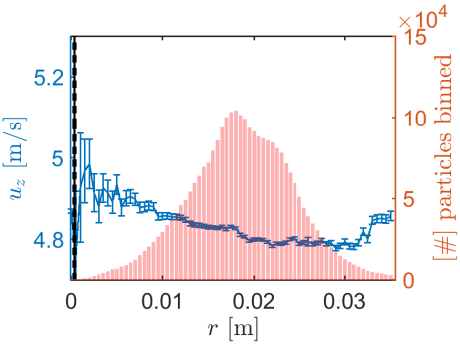

(c) Case 1, conditionally averaged axial velocity.

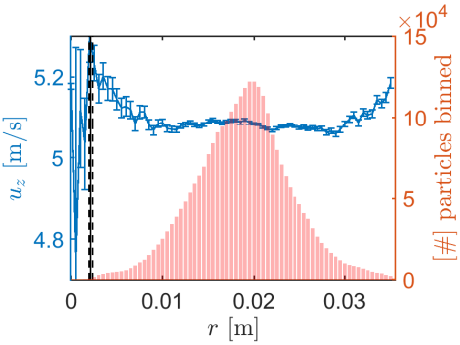

(d) Case 2, conditionally averaged axial velocity.

Figure 4.8: Profiles of the vortex velocity components of cases 1 and 2 described in table 4.1, conditionally averaged so that the centre of the reconstructed cavity is at $r = 0$, and over all four quadrants as described in figure 4.7. The vertical line indicates the cavity radius estimated from the reconstruction. The plots on the left (both top and bottom) are for case 1, while the ones on the right are for case 2. The resulting number of particle displacements averaged is shown in the red histogram data for each plot. The top figures correspond to the azimuthal component of the vortex onto which the various vortex models described in §4.2 have been fitted. The axial velocity components are shown in the plots below.

Model Parameters	Case 1	Case 2	Literature
Proctor Model			
Γ_∞	0.85	0.74	0.22^* (eq. 4.3)
r_v	6.5	6.9	9.4[27]
B	16.24	8.25	0.3^*[27]
β	20.58	15.41	14.5 [27]
Bosschers Analytical Model			
Γ_∞	0.18	0.18	-
r_v	24.21	23.4	-
Bosschers Semi-Empirical Model			
Γ_∞	0.18	0.2	-
r_v	6.5	6.9	-
ζ_1	59.06	49.75	57.5[9]
ζ_2	1.86	1.84	1.81 [9]
p	1.63	1.61	1.13 [9]
B	0.3^*	0.3^*	0.3^*[9]
q	2^*	2^*	2^*[9]
$\hat{\alpha}$	0.8^*	0.8^*	0.8^*[9]
Choi and Ceccio Model			
Γ_∞	0.11	0.117	-
r_v	7.6	8.3	-
γ	-11.7	-1.74	ranging between 0 and 1 [13]

Table 4.2: Summary of fitted model parameters to the azimuthal velocity data described in §4.4 and corresponding to the discussion in §4.4.3. A separate column with parametric entries from literature is also provided, predominantly from the work of Pennings et al. [27] and Bosschers [9]. If the parameter is not optimized and assumed constant, it is marked by a $*$. Γ_∞ has units of m^2/s, B has units of m whereas r_v has units of mm.

circulation strength can be extracted from the fit. For the model by Choi and Ceccio in eq. 4.10, the model was fitted to the viscous core region alone as it was unable to be fitted to both the irrotational and the viscous core region simultaneously. This is not an issue, as the model is specialized to vary it's behavior in the viscous core region alone, therefore, the retrieved value of γ parameter is instructive. The semi-empirical model of Bosschers in eq. 4.7 has a wide range of applicability, and it was tuned to fit most of the data range available.

The vortex models were fitted to measurement data using a non-linear least squares solver in MATLAB. The recovered magnitudes of the fitted parameters are tabulated in table 4.2 and the fits themselves have been plotted altogether in the figure 4.8. We first comment on the general behavior of the fit, following which comments on the parameter magnitudes are provided. This latter discussion is facilitated by the availability of fitting data in the works of Pennings [27] and Bosschers [9], specifically for our measurement cases of the NACA 66_2-415 elliptical foil. However, it needs to be mentioned that only the data of Pennings considers a measurement location at least 5 chord lengths downstream of the tip of the hydrofoil. Nevertheless, comparison with the fitting performed by Bosschers at $z/C_0 = 1.14$ is instructive.

From figure 4.8, it is clear that the viscous core formulation of the Proctor vortex model is unable to describe the behavior of the azimuthal component in the viscous core region. In contrast, the irrotational model can very adequately describe the region outside the viscous core, in line with prior observations by Pennings [27]. Secondly, the analytical vortex model of Bosschers [9] fails to describe the behavior of the vortex velocity profile, except for the outer regions of the flow. Therefore the model at best acts as an estimate of the circulation strength of the vortex only.

The behavior of the vortex model by Choi and Ceccio [13] is interesting as it is the only vortex model that is able to be fitted to the flow vectors inside the viscous core boundary and closer to the interface. However, the vortex model is unable to be adequately fitted to the irrotational region simultaneously. Exploring a blend between this model's formulation and the analytical model of Bosschers [9] could be interesting, but is outside the scope of the present work. Of all the vortex models tested, the semi-empirical vortex model of Bosschers (see §4.2.5) fits the best with the measurement data, although it does not follow the measured velocity very close to the interface. Considering that this model is well suited to cavitating vortices [9], a close examination of the magnitude of the fitted parameters is needed.

The fitted parameters and their values previously reported in literature are shown in table 4.2. The proctor vortex model's β parameter is close to that reported by Pennings et al. [27] which is important to note because this, alongside the B parameter, makes up most of the dimensionless parameters of the irrotational Proctor vortex model in eq. 4.3. At the same time, the magnitude of the B parameter is off the value reported in the literature. A minute comparison of the magnitudes of the parameter fit is not excessive, specifically because the semi-empirical model of Bosschers (§4.2.5) yields fit parameters with the present measurement data that are very similar to the ones reported by Bosschers [9]. As these parameters have no more than 15% deviation to the lift coefficient in the work by Bosschers, the semi-empirical model of Bosschers [9] is a remarkably well performing model that adequately describes cavitating vortices. Therefore, the viscous core radius and the circulation strength in the model are a good representation of the physical parameters of the vortex. This becomes more apparent when one compares the recovered circulation strength from the analytical vortex model of Bosschers (see §4.2.4) with that of the semi-empirical model, which are very similar. The semi-empirical model is also able to capture a marginal rise in the viscous core radius with a marginal increase in the flow Reynolds number, therefore capturing minute differences in the physical quantities of the cavitating vortex.

Perhaps surprising is the recovered fit parameter γ belonging to the vortex model of Choi and Ceccio (see §4.2.6). Even though the model adequately fits to the measured velocity vectors in the viscous core region of the cavitating vortex, the obtained value of γ is very much out of the expected range between 0 and 1. Noting that a γ of 0 is similar to a Lamb-Oseen vortex while a value of 1 is similar to the assumption of zero velocity at the interface, the negative magnitude of the γ parameter indicates that the azimuthal velocity of the measured vortex is higher relative to non-cavitating conditions. At the same time, as the γ magnitude is lower for the smaller cavitating vortex (Case 1) than for the fully developed case (Case 2), the degree of velocity increase is higher in Case 1 relative to Case 2. This observation, in combination with the fact that the semi-empirical model of Bosschers could not describe the observed measurement data near the interface, and accounting for the fact that measurement data itself deviates from a solid-body rotation profile in the core, suggests that the velocity vectors in the region of the cavity interface could have been corrupted by high-velocity particles, which may actually have been microbubbles. Considering the fact that microbubbles were not treated in the same manner as done in §2 (see 2.3.3), and that the dissolved gas content is well above oversaturation at c_∞/c_{sat} of approximately 1.5, it is expected that the flow itself contains a large amount of microbubbles

that are not distinguished from particles in the reconstruction technique developed in §3. This is motivated in the subsequent discussion.

Motivations for microbubble induced error in measurements

The motion of microbubbles around the vortex is modeled using a simple one-way coupled bubble trajectory model used in, for example, the work of Oweis et al. [26]. As the region of consideration is 5 chord lengths downstream of the tip, inception conditions are not important, and therefore the influence of bubble dynamics modeled by the Rayleigh-Plesset equations to the bubble trajectories is ignored. For the background flow, the Lamb-Oseen vortex is chosen with a circulation strength of 0.2 m^2/s, and r_v of 6.5 mm, therefore cavitation is ignored. The force balance on the bubble is given by the following equation:

$$\rho_b V_b \frac{d\mathbf{u}_b}{dt} = -V_b \nabla p + \frac{1}{2}\rho_L V_b \left(\frac{d\mathbf{u}}{dt} - \frac{d\mathbf{u}_b}{dt} \right) + \mathbf{F}_D + \mathbf{F}_L, \tag{4.13}$$

where $\mathbf{u}_b$ the velocity vector of the spherical bubble, which has a radius r_b, volume V_b, and density ρ_b. The right hand side of eq. 4.13 contains the force due to pressure gradient of the vortex, the added mass of the bubble, the drag, and lift forces. The Basset force and buoyancy force acting on the bubble is neglected here based on arguments found in [26], as is any spin on the bubble interface, which eliminates Magnus forces. The drag and lift forces acting on the bubble are dependant on the relative motion between the microbubble and the surrounding flow, which is characterized by a bubble Reynolds number, $Re_b = 2\rho_l r_b |\mathbf{u} - \mathbf{u}_b|/\mu$, where μ is the dynamic viscosity of the liquid, i.e., water. These forces are given by:

$$\mathbf{F}_{D,L} = C_{D,L} \frac{1}{2} \rho_L A_b (\mathbf{u} - \mathbf{u}_b) |\mathbf{u} - \mathbf{u}_b|, \tag{4.14}$$

where $C_{D,L}$ is the drag/lift coefficient of the microbubble, and A_b is the cross-sectional area of the bubble. The drag acting on the bubble can be reasonably modeled using the Schiller-Naumann drag model, whereas the lift coefficient is used from the estimates of Sridhar and Katz [33]. These are given as:

$$\begin{aligned} C_D &= \frac{24}{Re_b}(1 + 0.197 Re_b^{0.63} + 2.6 \cdot 10^{-4} Re_b^{1.38}), \\ C_L &= 0.59 \tilde{\alpha}^{0.25}, \end{aligned} \tag{4.15}$$

where $\tilde{\alpha}$ is the dimensionless shear-rate ($\alpha = \omega r_b / |\mathbf{u} - \mathbf{u}_b|$) for ω being the axial vorticity of the undisturbed flow at the bubble location.

The bubble trajectory model is solved using the 4th order Runge-Kutta solver. The bubble radius is varied from 100 μm to 250 μm in a steps of 50 μm. The bubble is released from a position $2.3 r_v$ from the vortex center and with an stationary initial velocity. The results of the calculated bubble trajectories are shown in figure 4.9. Included in the plots is the difference between the tangential velocity of the bubble and that of the background flow. The results indicate that at a bubble radius of 250 μm, the tangential velocity difference approaches a magnitude larger than 0.3 m/s, with gradually reducing difference as the bubble radius reduces. This result reaffirms the assumption that, when performing particle tracking

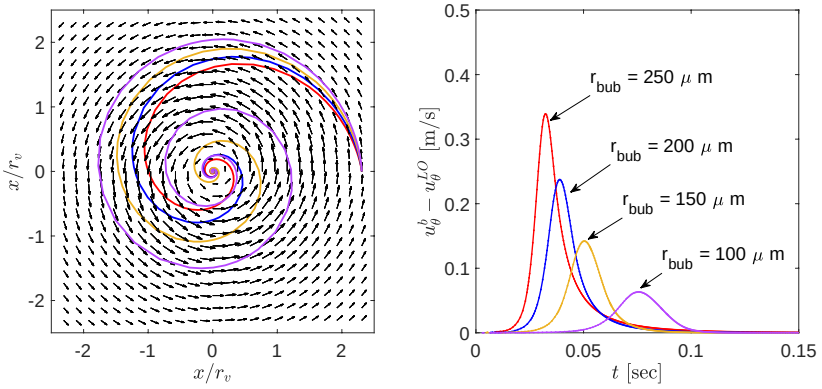

Figure 4.9: Left: Computed bubble trajectories released at $r = 2.3r_v$ of various diameters. The background Lamb-Oseen vortex is described by the quiver plot. Right: Difference between the tangential velocity of the bubble and the background flow in the bubble positions over time, and for various bubble radii. Colors in the left and the right plots correspond to the same bubble radius.

around a cavitating vortex, measurement errors can be encountered if one measures microbubbles in lieu of the tracer particles seeded into the flow. Therefore, maintaining a very low nuclei concentration in the flow is of immense importance when performing velocimetry around a cavitating vortex.

4.5 Conclusions

The measured velocity fields for a cavitating tip-vortex generated by a NACA $66_2 - 415$ hydrofoil were analysed by conditionally averaging the velocity vectors based on focality and quadrant-wise location. Following this, a set of vortex models were tested against the measurement data. In the comparison with the measurement data it was found that the Proctor's vortex model was adequate in describing the irrotational region of the cavitating vortex, however, it did not yield a satisfactory fit to the ambient circulation strength of the vortex, and therefore is not a good model to be used to describe a cavitating vortex. In contrast,the analytical model by Bosschers yielded a very good fit to the observed circulation strength of the cavity and the semi-empirical vortex model of Bosschers fitted quite well to the measurement data, with the fitted parameters closely matching the reported values in literature.

At the same time, the semi-empirical vortex model was unable to describe the flow vectors near the interface, which were well described by the vortex model by Choi and Ceccio with the caveat that the fitted γ parameter was well out of the reported range by Choi and Ceccio. This suggested that the flow had accelerated close to the interface relative to the flow velocity in non-cavitating conditions. It was hypothesized that the velocity vectors have been contaminated by microbubble trajectories instead of the tracers embedded in the flow. These remarks were further motivated by computing idealized bubble trajectories around a Lamb-Oseen vortex using a one-way coupled model, showing an increase in the

tangential velocity of the bubble as it is ingested by the vortex. It was then remarked from this that measurements of the near interface velocity of a cavitating vortex should be very carefully performed, ideally without any microbubbles in the flow. Therefore, measurement practices should allow for removing microbubbles from the flow, either by using cavitation tunnels with provisions for them or by shutting down the measurement facility prior to taking data and removing underpressure conditions to it so that the microbubbles that were generated in the flow from the previous experiment can dissolve back into the flow.

Although the present study does not contain extensive repeat measurements of the vortex profile at similar flow conditions, the similarity between the measured velocity profiles and the semi-empirical model of Bosschers at different r_c points towards a hypothesis on the influence of the developing cavity size on the vortex velocity profile: the velocity profile around a wing-tip vortex cavity that is developing in size, either due to ingestion of microbubbles or due to diffusion of dissolved gases into the cavity, and not due to variations in flow parameters like the cavitation number, Reynolds number or the lift coefficient of the foil generating the vortex cavity, does not change during the course of development of the cavity.

The results and the accompanying hypothesis also support the assumption of the same done in chapter 2 of this work, where a stationary Lamb-Oseen profile was used to represent the kinematics of the vortex during its growth.

Bibliography

[1] Adhikari, D. and Longmire, E. K. (2012). Visual hull method for tomographic piv measurement of flow around moving objects. *Exp. Fluids*, 53(4):943–964.

[2] Amini, A., Reclari, M., Sano, T., Iino, M., Dreyer, M., and Farhat, M. (2019). On the physical mechanism of tip vortex cavitation hysteresis. *Exp. Fluids*, 60(7):118.

[3] Arakeri, V., Higuchi, H., and Arndt, R. (1988). A model for predicting tip vortex cavitation characteristics. *J. Fluids Eng.*, 120(6):190–193.

[4] Arndt, R. and Keller, A. P. (1992). Water quality effects on cavitation inception in a trailing vortex. *J. Fluids Eng.*, 114(3):430–438.

[5] Arndt, R., Pennings, P., Bosschers, J., and Van Terwisga, T. (2015). The singing vortex. *Interface focus*, 5(5):20150025.

[6] Arndt, R. E. (2002). Cavitation in vortical flows. *Ann. Rev. Fluid Mech.*, 34(1):143–175.

[7] Bosschers, J. (2009). Investigation of hull pressure fluctuations generated by cavitating vortices. In *Proc. First Symp. Marine Propulsors*.

[8] Bosschers, J. (2018a). An analytical and semi-empirical model for the viscous flow around a vortex cavity. *Intl. J. Multiphase Flow*, 105:122–133.

[9] Bosschers, J. (2018b). *Propeller tip-vortex cavitation and its broadband noise*. PhD thesis, University of Twente.

[10] Brennen, C. (1969). The dynamic balances of dissolved air and heat in natural cavity flows. *J. Fluid Mech.*, 37(1):115–127.

[11] Bretschneider, H., Bosschers, J., Choi, G., Ciappi, E., Farabee, T., Kawakita, C., and Tang, D. (2014). Specialist committee on hydrodynamic noise, final report and recommendations to the 27th ittc. *Copenhagen, Sweden*.

[12] Chen, L., Zhang, L., Peng, X., and Shao, X. (2019). Influence of water quality on the tip vortex cavitation inception. *Phys. Fluids*, 31(2):023303.

[13] Choi, J. and Ceccio, S. (2007). Dynamics and noise emission of vortex cavitation bubbles. *J. Fluid Mech.*, 575:1–26.

[14] Dreyer, M., Decaix, J., Münch-Alligné, C., and Farhat, M. (2014). Mind the gap: a new insight into the tip leakage vortex using stereo-piv. *Exp. Fluids*, 55(11):1–13.

[15] Duarte, C., Chapuis, L., Collin, S., Costa, D., Devassy, R., Eguiluz, V., Erbe, C., Gordon, T., Halpern, B., Harding, H., et al. (2021). The soundscape of the anthropocene ocean. *Science*, 371(6529).

[16] Elsinga, G. E., Scarano, F., Wieneke, B., and van Oudheusden, B. W. (2006). Tomographic particle image velocimetry. *Exp. Fluids*, 41(6):933–947.

[17] Gerz, T., Holzäpfel, F., Bryant, W., Köpp, F., Frech, M., Tafferner, A., and Winckelmans, G. (2005). Research towards a wake-vortex advisory system for optimal aircraft spacing. *Comptes Rendus Physique*, 6(4-5):501–523.

[18] Higuchi, H., Arndt, R., and Rogers, M. (1989). Characteristics of tip vortex cavitation noise. *J. Fluids Eng.*, 111(4):495–501.

[19] Holl, J. (1960). An effect of air content on the occurrence of cavitation. *J. Fluids Eng.*, 82(4):941–945.

[20] Holl, J. and Treaster, A. (1966). Cavitation hysteresis. *J. Basic Eng.*, 88(1):199–211.

[21] Hsiao, C. and Chahine, G. (2002). Prediction of vortex cavitation inception using coupled spherical and non-spherical models and unrans computations. In *Proc. 24th Symp. Naval Hydrodynamics, Fukuoka, Japan*.

[22] Hsiao, C.-T. and Chahine, G. L. (2005). Scaling of tip vortex cavitation inception noise with a bubble dynamics model accounting for nuclei size distribution. *J. Fluids Eng.*, 127(1):55–65.

[23] Hsiao, C.-T., Chahine, G. L., and Liu, H.-L. (2003). Scaling effect on prediction of cavitation inception in a line vortex flow. *J. Fluids Eng.*, 125(1):53–60.

[24] Khoo, M., Venning, J., Pearce, B., and Brandner, P. (2020). Statistical aspects of tip vortex cavitation inception and desinence in a nuclei deplete flow. *Exp. Fluids*, 61:1–13.

[25] Lamb, H. (1934). *Hydrodynamics*. Cambridge University Press, Cambridge, UK.

[26] Oweis, G., Van der Hout, I., Iyer, C., Tryggvason, G., and Ceccio, S. (2005). Capture and inception of bubbles near line vortices. *Phys. Fluids*, 17(2):022105.

[27] Pennings, P. (2016). *Dynamics of vortex cavitation*. PhD thesis, Delft University of Technology.

[28] Pennings, P., Bosschers, J., Westerweel, J., and Van Terwisga, T. (2015a). Dynamics of isolated vortex cavitation. *J. Fluid Mech.*, 778:288–313.

[29] Pennings, P., Westerweel, J., and Van Terwisga, T. (2015b). Flow field measurement around vortex cavitation. *Exp. Fluids*, 56(11):1–13.

[30] Pennings, P., Westerweel, J., and van Terwisga, T. (2016). Cavitation tunnel analysis of radiated sound from the resonance of a propeller tip vortex cavity. *Intl. J. Multiphase Flow*, 83:1–11.

[31] Proctor, F. (1998). The nasa-langley wake vortex modelling effort in support of an operational aircraft spacing system. In *36th AIAA Aerospace Sciences Meeting and Exhibit*, page 589.

[32] Schanz, D., Schröder, A., Gesemann, S., Michaelis, D., and Wieneke, B. (2013). Shake the box: a highly efficient and accurate tomographic particle tracking velocimetry (tomo-ptv) method using prediction of particle positions. In *10TH Intl. Symp. Particle Image Velocimetry*.

[33] Sridhar, G. and Katz, J. (1995). Drag and lift forces on microscopic bubbles entrained by a vortex. *Phys. Fluids*, 7(2):389–399.

[34] van Wijngaarden, E., Bosschers, J., and Kuiper, G. (2005). Aspects of the cavitating propeller tip vortex as a source of inboard noise and vibration. In *ASME 2005 Fluids Engineering Division Summer Meeting*, pages 539–544. Am. Soc. Mech. Eng. Digital Collection.

[35] Van Wijngaarden, H. C. J. (2011). *Prediction of propeller-induced hull-pressure fluctuations*. PhD thesis, Delft University of Technology.

[36] Varadharajan, P. K. (2019). The effect of upstream turbulence on a tip-vortex. *MSc Thesis, Delft University of Technology*.

5

Conclusions and Outlook

This thesis is an experimental work that aims to elaborate the transport of dissolved gases into a vortex cavity in order to better understand mechanisms behind cavitation hysteresis. This chapter begins with a brief summary of the main hypotheses and findings this thesis in (§5.1). Finally some recommendations for further work are given in §5.2.

5.1 Conclusions

5.1.1 Diffusion Driven Growth of Cavitating Wing-Tip Vortices

The first study in this work aims at understanding the phenomenology of cavitating vortex growth when exposed to dissolved gases in the flow. This study was carried out by performing experimental studies on the development of a vortex cavity generated by a NACA $66_2-(415)$ elliptical foil, which were compared against a theoretical model developed in this work. The conclusions found from these are enumerated as follows:

1. **Hypothesis 1:** *There exists a thin diffusion layer of the shape of a hollow cylinder immediately outside the interface of a vortex cavity. The thickness of this layer is much smaller than the size of the vortex cavity.*

   Following inception, and in conditions where the population of microbubbles in the flow has no influence on the cavity growth, the mechanism of vortex cavity growth can be described as a diffusion dominant phenomenon where gases dissolved in the liquid enter the vortex cavity through a diffusion layer located outside the interface. If the modeled shape of the diffusion layer is either hollow-cylinder like (thin-film model, §2.2.2.2), or a developing boundary layer like (convective-diffusion model, §2.2.2.1), a good match to the experimentally observed growth rate of a wing-tip vortex cavity was found (§2.4.3). A qualitative agreement to data found in literature was also made using the diffusion models (see figure 2.10 and the accompanying discussion).

2. Both models discussed above predict the same result because their predicted growth rates can be tuned based on their individual diffusion velocity parameters. For the

convective-diffusion model, this parameter was based on the length of the vortex-cavity (l_c in eq. 2.11). For the thin-film diffusion model, this parameter was the thickness of the diffusion layer (t_f in eq. 2.15). The tuned value of l_c did not match the observed length of the cavity, whereas a similar physical interpretation for t_f is not available.

3. **Hypothesis 2:** *The concentration of air inside the vortex cavity is homogeneous.*

   As the diffusion coefficient for air in water vapor is much higher than that in liquid, it is reasonable to expect homogeneity of air inside the cavity by virtue of the diffusion model based on the heat conduction analogy (see §2.2.2.3).

4. **Hypothesis 3:** *The azimuthal vortex profile remains constant during the course of development of the vortex cavity. Under the assumption of zero shear stress on the interface of the cavity, this suggests that the vortex cavity interface spins faster on diffusion driven growth.*

   This was later investigated and confirmed in chapter 4 using measurements of the velocity profile around a vortex cavity at different stages of growth, using measurement techniques developed in chapter 3. This will be discussed in subsequent sections.

5. **Hypothesis 4:** *The size of a vortex cavity is unstable in oversaturated dissolved gas conditions ($c_\infty/c_{sat} \geq 1$), while stable sizes are possible only in undersaturated dissolved gas conditions ($c_\infty/c_{sat} < 1$).*

   Motivations for unstable vortex cavity size are based on experimental observations in the present work, while motivations for a stable vortex cavity size in undersaturated dissolved gas conditions can be found in the discussions in §2.4.2.

5.1.2 Three Dimensional Multiphase Flow Characterisation for Cavitating Vortices

A key assumption in modelling the diffusion driven growth of cavitating vortices was that the flow field remains unchanged during the course of the vortex cavity development, deeming it necessary to support the hypothesis with experimental data. In order to measure the average velocity profile around a vortex cavity using a particle tracking approach where data is gathered using a multi-camera setup, it was necessary to account for imaging challenges due to the opacity of the cavity when performing the measurements (see figure 3.1). Another challenge is posed by the wandering of the vortex, requiring conditional averaging of the measured velocities. In this work, it was decided to combine shadowgraph imaging alongside particle tracking measurements. With this in mind, the conclusions from this work are enumerated as follows:

1. Two main requirements associated with the three-dimensional measurement of the velocity around a vortex cavity are recognised:

   (a) **Imaging system**

      i. **Requirement 1:** *Minimizing zones where the camera cover over a particle is less than three.*

This was achieved in the present work by careful choices in the buildup of the multi-camera setup, and achieving all round illumination of particles around the cavity using two perpendicularly combined laser illumination sources split from one using a beam splitter;

ii. **Requirement 2:** *Eliminating specular reflection of the scattered light at the vapor-liquid interface of the cavity.*
This was achieved in this work by arranging the cameras in forward scattering mode with respect to the illumination;

iii. **Requirement 3:** *Maximizing the length of the illuminated volume along the axis of the vortex to image relatively long particle tracks.*
This was achieved in the present work as a by-product of choosing the forward scattering arrangement.

iv. **Requirement 4:** *Providing a silhouette of the vortex cavity in the image.*
This was achieved in the present work using non-flickering LED backlight illumination placed directly opposite to the camera view.

v. **Requirement 5:** *Clearly distinguishing between particles and bubbles in the images.*
This requirement could not be achieved in the present measurements, and caused a large bias error in the velocity measured near the vortex cavity.

(b) **Reconstruction procedure**

i. **Requirement 6:** *Separating the shadowgraph signal from the light scattered by the particles.*
This was achieved using a deep learning model that separates signals of different semantic meaning in the image (background versus cavity), through the DeepLabV3+ convolutional neural network model (see figure 3.5). The segmented cavities from the images were then used to reconstruct the visual hull of the vortex cavity in three dimensions using a volume carving approach (see eq. 3.3 and figure 3.7).

ii. **Requirement 7:** *Focality agnostic particle tracking approach.*
This was achieved in the present work within the projective geometry framework after the image distortion was removed (see figure 3.4). Particles were detected in the images as ellipses, matched across image sets in the multi-view setup and reconstructed as ellipsoids using the projective relationship between ellipses and ellipsoids. A key benefit of the ellipse-like interpretation of a particle image was that it models distortions to the particle image naturally, and can be interpreted as an error ellipse for the true location of the centroid of the particle. The particle tracking approach performed the particle matching taking into account the size of the particle image, the image disparity and the position of each reconstructed particle relative to the axis of the reconstructed vortex cavity. Particle tracks were built by spanning multiple particle track options per particle using a combination of a vortex model and a polynomial fit to the track data. Finally tracks were selected by minimizing the averaged reprojection error

of each option. A post-processing operation was implemented to ensure that particle tracks were unique to each particle considered in the images.

2. The reconstructed flow field and vortex cavity data was assessed using a series of metrics:

   (a) Vortex cavity shape (see figure 3.11): The convolutional neural network provided a typical detection error of 5% or less than 5% for the mIOU metric (eq. 3.7) and between of 20% for the bf-score metric (eq. 3.8), both of which were considered acceptable for the present purpose.

   (b) Flow field (see figure 3.13): The time averaged flow field was shown to follow the divergence free condition (see fig. 3.12). The preprocessed and post processed relative detection probability of the tracking algorithm (see eq. 3.10) was found to be in the neighborhood of 70% and 90%, respectively. For the velocimetry data, the distribution of the displacement error (see eq. 3.11) was found to peak around 1.4% of the inter-frame particle displacement for the measured axial velocity of around 5 m/s, and around 7% of the inter-frame particle displacement for a peak transverse velocity of around 1 m/s.

5.1.3 The Kinematics of Developing Gaseous Vortex Cavities

Following the reconstruction of the velocity field around the vortex cavity, the next steps were to perform a conditional averaging of the measured particle displacements and compare vortex models against the velocimetry data in order to infer the behavior of the kinematics of the vortex cavity during the course of its development in size. With this in mind, the conclusions presented in this work are enumerated as follows:

1. The measured velocity fields were first analysed by conditionally averaging the velocity vectors based on camera cover over the particles (see figure 4.6) and based on the quadrant-wise location of the particles binned (see figure 4.7). Sensitivity of the conditionally averaged velocity profile to the location of the particle around the vortex cavity was larger than that due to camera cover. These sensitivities were higher in regions inside the viscous core. Camera cover sensitivities were negligible.

2. In the comparison of the measured velocity profiles to the vortex models found in literature (see figure 4.8), it was found that the Proctor's vortex model (see eq. 4.3) was adequate in describing the irrotational region of the cavitating vortex, similar to conclusions previously found in literature. However, it did not yield a satisfactory fit to the ambient circulation strength of the vortex, and therefore was not a suitable model for describing a cavitating vortex. In contrast, the analytical model by Bosschers (see eq. 4.5) yielded a very good fit to the observed circulation strength of the cavity and the semi-empirical vortex model of Bosschers (see eq. 4.7) fitted quite well to the measurement data, with the fitted parameters closely matching the reported values in literature.

3. **Consequence of not satisfying requirement 5:** Despite the success of the semi-empirical vortex model, there was significant scatter in the measurement data for the flow velocities inside the viscous core of the vortex. The velocities in this region were

well described by the vortex model by Choi and Ceccio (see eq. 4.10), but required the assumption that the flow accelerates during the growth process from the profile found in a non cavitating vortex. This led to the hypothesis that the flow velocities near the interface of the cavity were corrupted by the brighter microbubbles in that region. This hypothesis was supported by performing one-way coupled trajectory calculations of microbubbles embedded in a Lamb-Oseen background flow when released from a stationary state. This analysis confirmed that a false registration of microbubbles as particles causes an increase in the measured tangential velocity relative to the background flow.

4. **Motivations for hypothesis 3:** Because the flow parameters of the measured datasets, which contained two different sizes of the vortex cavity, were similar in nature, it was possible to comment on the behavior of the vortex velocity profile's behavior during the development of the vortex cavity. The relatively similar average velocity profiles and fit coefficients to the velocity profiles using the semi-empirical model of Bosschers verified the hypothesis considered in chapter 2 on the influence of the developing cavity size on the vortex velocity profile. Therefore, it can be said that the velocity profile around a wing-tip vortex cavity that is developing in size, either due to ingestion of microbubbles or due to diffusion of dissolved gases into the cavity, and not due to variations in flow parameters like the cavitation number, Reynolds number or the lift coefficient of the foil generating the vortex cavity, does not change during the course of development of the cavity.

5.1.4 Experimental Practices for Cavitation Observations

From both of the measurement campaigns conducted in this work, one on the shadowgraph survey of the development of the vortex cavity (chapter 2), and the other on the three-dimensional particle tracking survey of a segment of the vortex cavity (chapter 3), some measurement practices and concerns were identified. These are enumerated in the following discussion:

1. **Experiences from the shadowgraph survey:**

   The growth behavior of the vortex cavity was found to be fairly repeatable in nuclei depleted conditions, and strongly affected by nuclei in weak-water conditions, although, the influence of the relative saturation of dissolved gases could still be discerned from the non-repeatable measurements. In cavitation tunnels that do not have provisions for water quality control, it is possible to obtain repeat experiments by shutting down the cavitation tunnel and introducing the tunnel to atmospheric pressure between runs. This provides the residence time for the gas bubbles to either separate due to their buoyancy, or reabsorb back into the solution. If stable cavity sizes are intended, the degree of undersaturation must be high (see hypothesis 4) so as to reduce the diffusion time-scales required before the cavity size stabilizes.

2. **Experiences from the particle tracking survey:**

   Measurements of the flow field around a vortex cavity are sensitive to microbubbles in the region near the vortex cavity. If the tracer particles seeded into the flow cannot be discerned from microbubbles, it is possible to register the scattered intensity

of microbubbles instead of tracer particles. Therefore, the measurement practices highlighted in the previous discussion should be followed, where the tunnel ambient pressure is equalised with the outside atmosphere between runs to dissolve the microbubbles, and care must be taken to minimize the size and population of microbubbles in the flow by choosing a suitable experimental facility. In the present work, due to the chronology of conducting these two measurement campaigns, it was not possible to use the insights gained from the shadowgraph survey towards the particle tracking survey. Furthermore, dedicated mechanisms to control the size and population of microbubbles were not present in the flow facility.

5.2 Outlook

The conclusions and hypotheses presented in this work have attempted to expand our understanding of the effect of water quality on a vortex cavity at model scale sizes. In the next steps following this work, there are several areas where improvements can be made to the insights from the present work, as well as the methods and materials considered in the present work. These are enumerated categorically as follows:

1. **Diffusion Driven Growth of Vortex Cavities:** The next steps towards diffusion modeling should be to test the diffusion model across different measurement facilities, and implement the diffusion model in multiphase CFD solvers. This can be used in the initialization stage where the cavity is grown using the diffusion model. Furthermore, experimental studies linking the diffusion driven growth to cavitation desinence, therefore cavitation hysteresis, should be carried out. Further studies must also be conducted on elaborating the sensitivities of the diffusion velocity parameters which controls the diffusion rate of the dissolved gases.

2. **Advancements in Measurement and Reconstruction Methods for Cavitation Studies:** Advanced measurement techniques such as that used in the present work have so far had very limited applicability in cavitation measurements. Undoubtedly this is due to the immense difficulty with measuring displacements using vision based systems, however, as has been shown in this work, machine learning approaches augment traditional three-dimensional measurement techniques quite well. Efficiencies in reconstructing flow fields by incorporating faster particle tracking algorithms must be explored. Separating the measurement signal from microbubbles and particles, done for example by the use of fluorescent tracer particles, should also be considered. Mechanical design of these vision systems should be given serious attention to in order to reduce the time to insight for cavitation measurements. Ultimately, when sufficient maturity has been achieved with the mechanical and algorithmic design of these techniques, pressure reconstruction of the flow around cavitating vortices should be carried out. This will ultimately connect the velocimetry measurements to noise radiated in the underwater environment.

3. **Measurement and Modeling of Vortex Cavity Inception:** The present particle tracking code can be used to measure strain in spherical bubbles as they approach inception sites while providing tracking information. The technique is suited towards inception studies because the stretching of a microbubble can be captured by the

ellipsoid like reconstruction of its shape, which has a projective relationship to ellipses detected in images of microbubbles that approach inception sites.

4. **Vortex Cavitation Research and Measurement Practices:** Vortex cavitation research, specifically towards the understanding of cavitation noise, should explore hydrofoil geometries beyond the NACA $66_2 - (415)$ hydrofoil. This allows a fair assessment of phenomenology by repeating it across hydrofoil geometries. Furthermore, initiatives to standardize measurement practices to minimize the influence of dissolved gases should be pursued. This will improve repeatability across facilities. Furthermore, reconstruction of the flow field around helecoidal vortex cavities should also be attempted considering the measurement and reconstruction techniques used in this work. In order to do so, it is wise to begin with a low number of propeller blades to minimize reconstruction challenges.

5. **Modernization, Innovation and Standardization of Cavitation Research Facilities:** Owing to the sensitivity of vortex cavitation to water quality effects, it must be recognized that cavitation research facilities have different design requirements to water tunnels. The conventional cavitation tunnel, such as that used in the present work, distinguishes itself from water tunnels only through the control of the ambient pressure in the tunnel. Considering the growing number of newly built state-of-the-art facilities that are designed based on water quality requirements, it is clear that a cavitation facility is fundamentally differently designed today. At the same time, designs are not standardized, and remain expensive to construct. Innovations are needed to reduce difficulties in the construction of these facilities. The core requirements of a cavitation tunnel facility with water-quality considerations must be codified and disseminated in the cavitation research community.

Curriculum Vitæ

Swaraj Nanda

16-03-1992 Born in Doranda, Ranchi, India.

Education

2014 B.S Marine Engineering
Tolani Maritime Institute (affl. BITS, Pilani),
Talegaon, Maharashtra, India

2016 M.Sc. Ship Hydromechanics
3mE, Delft University of Technology,
Delft, The Netherlands

2021 PhD. Vortex Cavitation
3mE, Delft University of Technology,
Delft, The Netherlands

Thesis: Gas Transport Into Vortex Cavities

Promotor: Prof. dr. T. J. C. van Terwisga
Prof. Jerry Westerweel

List of Publications

1. **Nanda S.**, Westerweel J., van Terwisga T., Elsinga G. E.: *Shape Reconstruction of an Unsteady Wing-Tip Vortex Cavity*, 10th International Conference for Multiphase Flows, 23rd May (2019), Rio de Janeiro, Brazil.

2. **Nanda S.**, Westerweel J., van Terwisga T., Elsinga G. E.: *Mechanisms of Diffusion Driven Growth of Vortex Cavities*, 11th International Symposium on Cavitation, 11th May (2021), South Korea (Virtual).

3. **Nanda S.**, Westerweel, J., van Terwisga, T., & Elsinga, G. (2022). *Mechanisms for diffusion-driven growth of cavitating wing-tip vortices.* International Journal of Multiphase Flow, 156, 104146.

4. (*In Preparation*) **Nanda S.**, Muller K., Westerweel, J., van Terwisga, T., & Elsinga, G. (2023). *The Kinematics of Developing Wing-Tip Vortex Cavities using Simultaneous 3D Velocimetry and Shape Reconstruction.* International Journal of Multiphase Flows.

5. (*In Preparation*) Fiscaletti D., Thill C., **Nanda S.**, Nikolaidou L., Stigter R., Delfos R., Schreier S., Poelma C., Westerweel J., van Terwisga T.. (2023). *Design and flow characterization of the Multi-Phase Flow Tunnel (MPFT) of Delft University of Technology*, Experiments in Fluids

Acknowledgements

This dissertation work was the most difficult intellectual undertaking I have considered in my life thus far. When I started this task, I had recently completed my conceptual design work on the next generation cavitation tunnel (now called the Multiphase Flow Tunnel) for the university. It became very clear to me that I would be replacing the very facility I needed to complete my investigations, or as Rene Delfos said to me once, shooting my own foot. It turned out that I would have only two years to develop my experimental work and gather precious data, and I would have two years to scan the data for insights. At the same time, I wanted to accomplish a considerable amount of research for my field. I decided to study diffusion of dissolved gas into a vortex, and find a way to reconstruct the three dimensional flow field around it, neither of which had been done previously in literature, and pursued my experimental work on these two topics with full steam. At the end of the first two years, when the facility I used was dismantled, I had a fistful of raw experimental data, and no means to know if my measurements would yield any insight on the gas diffusion phenomenon. I also did not know if the multi-camera data I had would even yield a three-dimensional reconstruction. This all had to be accomplished in the remaining two years, with no hope of looking back had I done something wrong in my measurements. This was the biggest risk I had ever taken, and it was a decision that kept me on my toes for the rest of my PhD period.

Naturally, with such ambitious plans and with a timeline akin to threading a needle with my eyes closed, I did not achieve any of it by myself. I want to acknowledge the people who helped me find my answers; I am here today only because I could stand on the shoulders of those giants. To begin, my thesis co-promotor Gerrit Elsinga was easily the best supervisor I had ever come across. He was very open minded, full of wisdom, and understanding of my ambitions. I happily acknowledge here that I would not have managed these tasks without his guidance. In his absences, I had the privilege to be guided by Jerry Westerweel, who has enormous insight on fluid flow phenomenon, has a stellar recognition in the field of fluid flow, and knows exactly how an open problem can be tackled. I say this because he guided me on how to discover my diffusion model, by instructing me to start with a simple model, and add to it to build a predictive ability in that model. I must also mention here the guidance I have received from Tom van Terwisga. An incredibly kind being, he has always been a father figure in my research journey, right from the very beginning when I approached him for a role at MARIN during my masters in 2015. He occupies a special place in my heart, and has instilled in me my research attitude. He is an exceptional supervisor, and due to my exposure to him over the years, I understand why he where he is. Together, we tackled several challenges in cavitation research, and I will forever be in debt to him for those wonderful years.

A second round of acknowledgement goes to people who have equal contribution to seeing my work to fruition. Firstly, without my collaboration with Koen Muller in the use of his fish tracking algorithm, there would have been no way to process the multi-camera

data that I had gathered with immense difficulty. In order to gather that data, an enormous experimental setup had to be designed and set up. I failed the measurements two times in the first two years before I got it right, and I could only get it right due to the involvement of expertise from Peter Poot, the facility manager at my laboratory who helped design my prisms and troubleshoot breakdowns in the facility, Edwin Overmars, the PIV expert who guided me with his wisdom on how to perform a PIV, and how to set up the laser illumination and cameras, Fritz Sterk, the electrical technician who constructed the LED pulsor circuit for me, and troubleshooted the drive system of the facility, Pascal Chabot, who assisted me with setting up my experiments on the last campaign, troubleshooted leaks together with me, stayed with me during the last campaign because I had an accident in the previous one, and kept my spirits high, and finally, Sebastien Schreier, who engaged with me intellectually and showed me a neat trick on how one could calibrate an absolute pressure sensor to measure vacuum pressures.

Then come the various people who made life beautiful in Delft. I would like to acknowledge Ankur Kislaya, who was my favorite banter partner during my time in Delft, Wick Hillege, who had been my loud and awesome room mate at the laboratory, Gunnar Jacobi who shared with me his enthusiasm for multi camera PIV and difficult experimental setups, Jennifer Monteiro for keeping the laughs going and for bringing her pet to the lab to keep us all in good mental health, and many many more people that I know I will miss out as this goes on. It is remarkable to know how many good people one comes across during their time in the laboratory.

Lastly, I want to thank my family, my parents for believing in me and my strengths and for giving me a chance to come to the Netherlands and get the education I wanted, my twin brother Swadhin Nanda for being a source of inspiration, my kindest sister Puja Nanda who has brought color to my life right from my birth, and her husband Jereon Latour, who is perhaps reading this and wondering what joke he could concoct out of this mist of acknowledgements. I have been truly lucky in life.

2023

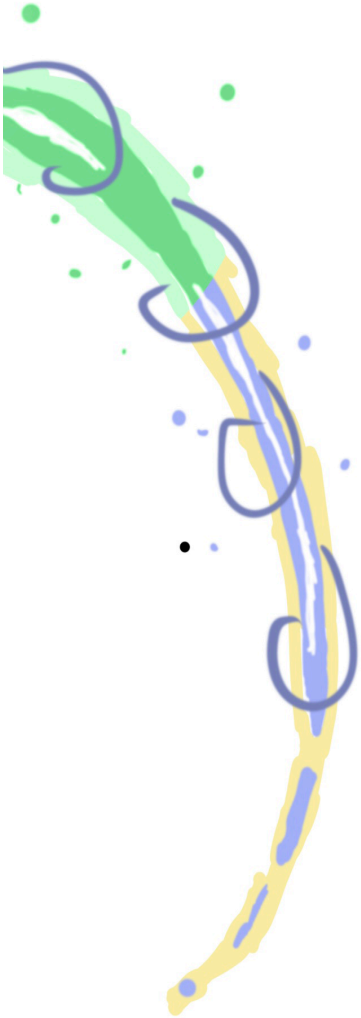

TU Delft

As the pressure inside the core of a vortex present in a liquid dips below the vapor pressure of the liquid, it ruptures, giving rise to vortex cavitation. This kind of cavitation is prevalent in marine propellers and is known to cause structural vibrations on a ship's hull and damage to a ship's propeller. It is also gaining attention for the noise it radiates into the underwater environment, which results in disruption to marine habitats. Studying vortex cavitation presents challenges, such as a lack of understanding of the influence of water quality on lab-generated vortex cavities, and the difficulty of applying 3D imaging and velocimetry techniques as investigative tools. In this experimental work, we address these challenges.